UNIVERSITY OF OKLAHOMA

GRADUATE COLLEGE

AN INTEGRATED SEDIMENTOLOGICAL AND GEOCHEMICAL STUDY TO TEST THE POSSIBLE LINKS BETWEEN LATE PALEOZOIC CLIMATE CHANGE, ATMOSPHERIC DUST INFLUX AND PRIMARY PRODUCTIVITY IN THE HORSESHOE ATOLL, WEST TEXAS

A DISSERTATION

SUBMITTED TO THE GRADUATE FACULTY

in partial fulfillment of the requirements for the

Degree of

DOCTOR OF PHILOSOPHY

By

SOHINI SUR
Norman, Oklahoma
2009

AN INTEGRATED SEDIMENTOLOGICAL AND GEOCHEMICAL STUDY TO TEST THE POSSIBLE LINKS BETWEEN LATE PALEOZOIC CLIMATE CHANGE, ATMOSPHERIC DUST INFLUX AND PRIMARY PRODUCTIVITY IN THE HORSESHOE ATOLL, WEST TEXAS

A DISSERTATION APPROVED FOR THE
CONOCOPHILLIPS SCHOOL OF GEOLOGY AND GEOPHYSICS

BY

Dr. Gerilyn S. Soreghan, Chair

Dr. Michael J. Soreghan

Dr. Richard D. Elmore

Dr. Susan E. Postawko

Dr. Arthur H. Saller

Dr. Timothy W. Lyons

Dedication

This dissertation is dedicated to my lovely parents and to my dear husband

Acknowledgements

I am extremely thankful to my advisor Lynn Soreghan for her advice, guidance, endless support and encouragements throughout this process. I am equally grateful to Mike Soreghan for his time and valuable guidance in every aspect of my work. My heartiest thank to both Lynn Soreghan and Mike Soreghan to grow my interest in this subject matter. I also like to thank my committee members Richard D. Elmore, Art H. Saller, Timothy W. Lyons and Susan E. Postawko for their help, suggestions and review of my dissertation. My sincere thank to Art H. Saller, G. Hinterlong, A. Auffant, S. Randall for help in core access and sampling. A special thank to Timothy Lyons for allowing me to use their laboratory facility and stay with his lovely family during my visit in University of California, Riverside.

I am grateful to Wan Yang for his time, valuable discussions, guidance and review of spectral analyses. Many thank to Brooks B. Ellwood for allowing me to use his laboratory facility (for magnetic susceptibility measurement) in Louisiana State University, Baton Rouge. I also like to sincerely thank Paul Philp, Juergen Schieber, Paul Wright, Paul Knauth, Troy Rasbury, Vladimir Davydov and Andy Madden for their help and valuable discussions. I really appreciate analytical help by George Morgan, Preston Larson, Ron Conlon, Clint Scott, Steve Bates, Robert Turner and Rick Maynard. I also like to thank my laboratory mates Sabata Pereira, Kristen Marra, Dustin Sweet, Alice Stagner, Vanessa Harvey and Alisan Templet for their analytical help and keeping a nice friendly environment in the laboratory. Special thank to Alice Stagner for her contribution in chapter 1 about Arrow Canyon.

I am indebted to the ConocoPhillips School of Geology and Geophysics, University of Oklahoma, Norman for financial support and providing me the opportunity to travel to professional meetings. I like to show my sincere gratitude to Shell Oil Company for a fellowship during my study and to American Association of Petroleum Geologists, the Geological Society of America and the Society for Sedimentary Geology (SEPM) Rocky Mountain Section (Donald L. Smith grant) for student research grant. Other financial assistance was provided by Chevron (USA) and grants from the American Chemical Society of Petroleum Fund and the National Science Foundation to Dr. Lynn Soreghan.

On a personal note, a special thank to my undergraduate advisor Santanu Banerjee and my senior Supriyo Mitra to encourage me for higher studies. I would like to thank my family and many friends (Tanima, Kausik, Subho, Kajari, Rumela, Shamik, Nabanita, Suprotik, Debu, Vishakha, Rahul and Andrea) for their support throughout this journey. My heartiest thank to my mom, dad and my sister who has supported in all the endeavors of my life. Special thank to my little nephew Ruhin who brought tremendous joy to my life. Last but not the least a very special thanks to Prasenjit, my husband and best friend, for his love, support and endless patience to this long journey of learning. Without him this would not have been possible.

Table of Contents

List of Tables

List of Figures

Abstract

Atmospheric dust is an important climatic agent as well as a valuable climatic archive. Recent studies have hypothesized ample dust deposits (loess) from late Paleozoic western equatorial Pangaea. However their relation with late Paleozoic climate change is understudied. In this study, I developed a methodology for sequential extraction of the silicate mineral fraction (SMF, a proxy for dust influx) from lithified carbonates and have applied this method to paleoclimatic interpretation of an upper Pennsylvanian glacio-eustatic sequence of Horseshoe Atoll, an isolated carbonate buildup of the Midland basin (west Texas).

The studied cycle (~ 30 m thick) consists almost entirely of carbonate with a thin interval of dark, pyritic mudrock at the sequence boundary. The SMF contains both detrital and authigenic silica and, using paleogeography, stratigraphy and petrographic constrains, both components are inferred to be of eolian origin. Accordingly, the SMF can be used as a proxy for atmospheric dust and attendant aridity. Dust varies over 2 orders of magnitude within the carbonate succession and is over 3 orders of magnitude higher in the mudrock. The mudrock is interpreted as a loess deposit that was pedogenically modified and subsequently transgressed. The stratigraphic position of the the mudrock, juxtaposed between the sequence boundary and early transgressive carbonate facies, suggests maximum aridity during lowstand to early transgression (glacial to incipient interglacial). Spectral analyses of the dust fraction within the carbonate reveals Milankovitch scale ($< 10^5$ yr) variations in atmospheric conditions through a single glacial cycle. Remarkably high abundance of highly reactive iron within

the mudrock together with recent recognition of high atmospheric dust load during the late Paleozoic suggest high reactive iron input to the late Paleozoic ocean and attendant marine primary productivity.

Chapter 1

Extraction methodology for the silicate mineral fraction from ancient carbonate: assessing the geologic record of dust

Abstract

The climatic influence of eolian dust (silt and finer sizes) is well recognized in the Cenozoic earth system, but less so for the pre- Cenozoic. In ancient carbonate rocks that formed isolated from fluvio- deltaic influx, the silicate mineral fraction can, in some cases, be shown to represent atmospheric dust. Here we present a methodology for sequential extraction of carbonate, organic matter, pyrite and iron- oxide from pre-Cenozoic carbonate strata to isolate the dust fraction, and illustrate the application to stratigraphic sequences in a late Paleozoic carbonate buildup and ramp setting.

Introduction

The geologic record of dust is of growing interest owing to its importance in the climate system (e.g. Rea 1994; Duce 1995; Mahowald et al. 1999; Kohfeld and Harrison 2001; Muhs and Bettis 2003; Anderson et al. 2006). Climate controls dust production, transportation and deposition. Thus dust deposits hold the potential to record high-resolution climate change through time. Additionally, atmospheric dust impacts the climate system by a) its direct and indirect effects on radiative forcing, which controls surface and atmospheric temperature and stability (e.g. Tegen et al. 1996; Yoshioka et al. 2005; Mahowald et al. 2006), and b) nutrient delivery to the land and ocean, which

influences the biosphere and thus affects the carbon cycle (e.g. Jickells et al. 2005 and references therein). To date, most studies of atmospheric dust have focused on the Cenozoic deep- sea record owing to the advantages imparted by 1) geographic isolation to eliminate the possibility of fluvio-deltaic contamination, and 2) a lack of diagenetic overprinting. Hence, non-authigenic mineral components isolated from deep- sea sediments have long been used as a proxy for atmospheric dust flux applied to paleoclimatic studies (e.g. Rea & Janecek 1981; Rea 1994; Hovan 1995; Lyle and Lyle 2002; Hyeong et al. 2006; Ziegler et al. 2007). In these studies the mineral components are extracted through a series of chemical procedures which involve removal of carbonate with acetic acid, removal of opal by sodium hydroxide or sodium carbonate and removal of Fe and Mn oxides and hydroxides by sodium dithionite-sodium citrate solution buffered with sodium bicarbonate (Rea and Janecek 1981). Clemens and Prell (1990) modified the procedures slightly by using: a) weaker buffered acetic acid to dissolve the biogenic carbonate, b) sodium hypochlorite treatment to remove organic material, and c) a stronger opal leach for complete dissolution of radiolaria and diatoms. Later Hovan (1995) modified the process for sediments with high concentrations of diatoms by using 1.5-N sodium hydroxide solution at 85°C for 2 hour to remove all biogenic silica. Recently, Lyle and Lyle (2002) recommended the use of 2M potassium hydroxide at 80 °C for 8 hours to remove opal from the sediments.

In contrast to the large body of work on atmospheric dust in oceanic sediments of the latest Mesozoic to Cenozoic, studies on pre- Cretaceous strata are rare (Soreghan et al. 2008 and references therein), in part owing to the absence of truly oceanic sediments for the older record, but also owing to the, until recently, poor recognition of the

contribution of dust to sedimentary systems. However, (paleo) geographic isolation can also be achieved in deeper- time continental epeiric regions by targeting systems that developed far from fluvio-deltaic sources, most notably, carbonate systems. Nevertheless, older strata also bear the complication of increasingly severe diagenesis. For example, ancient rocks commonly contain diagenetic pyrite, and recrystallization of opaline silica to authigenic quartz precludes separation of the authigenic from the detrital quartz (dust) in the extracted residue. However, the authigenic component can, in many cases, be considered to reflect an ultimate detrital origin (e.g. Cecil 2004; explained further later). Moreover, an advantage of the pre- Mesozoic is that many fine- grained siliceous biota (e.g. diatoms) had not yet evolved and thus do not pose a source of non- detrital silica.

In this paper we outline our approach for extraction of what we infer to be the atmospheric "dust" component from Pennsylvanian stratigraphic sequences of an isolated carbonate buildup of the "Horseshoe Atoll", Midland basin, west Texas (Fig. 1.1A) and from ramp carbonates of the Bird Spring Formation, Arrow Canyon, Nevada (Fig. 1.1B). We have modified the extraction methodology of Rea and Janecek (1981), Clemens and Prell (1990) and Hovan (1995) to address some of the problems unique to lithified strata; hence our approach should be generally applicable to many pre- Cenozoic systems.

Methodology

Samples of the Midland basin study site (Fig. 1.1A) are from an air-drilled core, covering a complete glacioeustatic sequence of ~ 30 m thickness, from which we sampled at 10 cm intervals. Samples of the Bird Spring ramp (Fig. 1.1B) are from outcrop exposed in Arrow Canyon, and constitute part of a glacioeustatic sequence of ~

24 m thickness which we sampled at 20 cm intervals. We collected at least 50 gm from each sample horizon and avoided sampling across stylolites.

A tile snipper or pestle was used to fragment the sample, which was then washed with distilled water, dried and gently crushed to approximately pea size using a mortar and pestle. The crushed rock sample was then transferred to a clean beaker and the sample weight recorded to the fourth decimal place. For Horseshoe Atoll samples, the starting amount of 50 gm ultimately yielded a residue of .0047 to 3.3444 gm (.0093 to 6.6885 wt %), which was sufficient for subsequent grain-size analysis. However, samples from the Bird Spring Formation were more siliciclastic rich, necessitating a sample mass of ~30 gm for this study. Accordingly, when applying this approach to samples with very different background levels of residue, either larger or smaller starting amounts might be more appropriate.

The initial step is removal of carbonate (calcite and dolomite). For this, approximately 300 ml of 2N hydrochloric acid (HCl) is added to the sample in the beaker on a hot plate set at 50°C. The sample is periodically stirred gently with a glass rod for an hour and then left covered with a watch glass to avoid evaporation and contamination. The pH of the acid is checked after 24 hours; if the pH approaches neutral the supernatant is then carefully decanted and fresh acid (~ 300 ml) added. This process is repeated until carbonate dissolution is complete, as indicated by no change in pH. We preferred 2N HCl for this step in order to speed the dissolution process considering our large starting amount (50 gm) and number of samples. The strength of the acid did not negatively affect subsequent petrographic analyses, nor measurements of the residue amount and grain size. Analyses of chemistry and clay mineralogy of the residue, however, should be done

on pristine sample splits using much weaker acid (e.g. acetic acid) for digestion in order to avoid chemical changes induced by acidification.

Once dissolution is complete the residue is gently rinsed with distilled water into a cleaned 50 ml polypropylene centrifuge tube, centrifuged for 10 minutes and the supernatant decanted. This process is repeated (up to 3-4 times) until no acid remains in the residue to form any salt.

The residue is then washed, using a minimal amount of distilled water, into a pre-weighed flask and freeze-dried for 24 hours. The dried sample plus flask is then weighed (3 times) and the weight recorded to the fourth decimal place to obtain the weight percent of residue. This residue is referred to as the “acid insoluble residue” which is devoid of carbonate (limestone and dolomite) (Fig. 1.2A).

Owing to the geologic age and setting of the samples, the presence of dead oil (bitumen) and kerogen proved problematic. Treatment with hydrogen peroxide is ineffective for this organic matter and, if not removed, the insoluble residue can become entrapped in the oil. We approached this by placing the freeze-dried insoluble residue into a pre-weighed crucible and combusting the sample at 500 °C for ~15 hours. The burned sample plus crucible was then weighed (3 times) and recorded to the fourth decimal place. This process worked well for our carbonate samples for two reasons: a) the rock contains very little total organic carbon (average TOC = 0.25 %), thus combustion at 500 °C removed most of the organics, and b) this process also oxidized most of the disseminated diagenetic pyrite to iron oxide (Fig. 1.2B, D), which enabled their subsequent dissolution using the citrate-bicarbonate-dithionite (CBD) method, originally described by Mehra and Jackson (1960) and later modified by Rea and Janecek

(1981). Alternatively, the combustion process could be completed before the acidification stage where entrapment of insoluble residue in the oil can be a problem during decantation in the acidification stage.

Following combustion, many of our insoluble, inorganic residues appeared red owing to the oxidation of pyrite (Fig. 1.2B, D). Removal of these amorphous coatings and crystals of free iron oxides and hydroxides is then possible using the citrate-bicarbonate-dithionite (CBD) method. We follow the procedure described by Rea and Janecek (1981) but slightly modified because of the small insoluble, inorganic residue size and consequent use of small (50 ml) centrifuge tubes. We halved the amount of sodium citrate and sodium bicarbonate recommended while keeping the concentrations unchanged. Residue is first placed in the 50 ml centrifuge tube and 20 ml of 0.3 M sodium citrate and 2.5 ml of 1 M sodium bicarbonate added. The centrifuge tube is then placed in a water bath set at 80°C. Once the temperature equilibrates, 0.5 gm of sodium dithionite powder is added and the solution is stirred for 1 minute. The solution is kept at 80 °C for 10- 15 minutes and then another 0.5 gm of sodium dithionite powder is added and the solution stirred intermittently for another 10 minutes. The sample is then centrifuged for 10 minutes and the clear supernatant decanted. Finally, 20 ml of 0.3 M sodium citrate is added and the sample stirred and centrifuged for 10 minutes and supernatant decanted. The residue is then rinsed with distilled water. The entire process is repeated as needed to ensure removal of all iron oxides, as determined by visual inspection. This process effectively removes amorphous iron oxide and hydroxides, and thus the oxidized pyrite. However it also removes any detrital hematite present in the insoluble, inorganic residue, which adds a minor error component in determination of the

detrital contribution. The contribution of detrital hematite relative to other, silicate mineral components, in the detrital load, however, is sufficiently minimal to justify this error. Furthermore, because this process is applied to all samples equally, removal of any detrital hematite should not significantly alter *relative* trends in residue amount through the study section. At this stage, the sample is free of carbonate, organic matter, pyrite and iron oxides. However, varying amounts of authigenic silica (e.g. silicified bioclasts, authigenic quartz) could be present in the residue, hence we term the remaining residue the "silicate mineral fraction" (SMF; Fig. 1.2C, E).

The SMF is gently washed through a 63 μm sieve to filter any sand- sized authigenic siliceous phases, such as sponge spicules or chertified fragments and the sieved fraction transferred to a beaker. The > 63 μm fraction ("sand- sized SMF") is transferred into a pre-weighed petri dish (Fig. 1.2F). The sample plus the petri dish is then weighed (3 times) to four decimal places. This coarser fraction is then visually examined by stereo microscope to identify any detrital components and these are then transferred into the < 63 μm fraction. Once picking is complete the remaining coarser fraction plus the petri dish is weighed again (3 times).

The < 63 μm fraction is then transferred in a pre-weighed flask and freeze-dried for 24 hours. The dried residue plus flask is weighed (3 times) and recorded to the fourth decimal place. Finally the residue (< 63 μm) is visually examined to identify, remove and weigh any obvious non- detrital component and the weight recorded again to determine the final weight percent of the residue. The residue is then ready for any petrographic (e.g. SEM, microprobe) and grain size analyses. At this stage, we term the remaining residue the "silt- sized SMF" (Fig. 1.2G), which is devoid of carbonate, organic matter,

amorphous Fe and Mn oxides and hydroxides, disseminated pyrite and biogenic siliceous phases of > 63 μm size. We cannot apply the term “detrital” residue owing to the presence of silt- sized authigenic silica, as discussed below.

Replicate analyses were done to check the reproducibility of the methodology and are typically within 0.1 to 2 %. A flowchart of the steps involved in this methodology of silicate mineral extraction is presented in figure 1.3.

Application

In a carbonate environment isolated from fluvio- deltaic systems, any detrital material (SMF) should reflect eolian input. Hence analysis of the detrital residue holds the potential to provide information on various aspects of paleoclimate, including variations in atmospheric dust loads (by studying weight percent through a section), wind strength (via grain size), and wind direction (using provenance of the detrital fraction). Below, we illustrate the application of this method to two different study areas.

Example 1: Application to an isolated carbonate buildup

Figure 1.4A shows results of our extraction processes applied to a single upper Pennsylvanian (Virgilian) glacioeustatic sequence of approximately 30 m from “Horseshoe Atoll,” a series of isolated carbonate buildups located in the interior Midland basin, west Texas (Fig. 1.1A). Our results show that SMF varies in a nonrandom pattern, in the sense that it increases significantly close to the sequence boundary and decreases away from it and exhibits nonrandom variations throughout the carbonate succession. The SMF in the carbonate is dominated by authigenic quartz (fine- grained doubly

terminated prisms; Fig. 1.2E, F, G) and we address origin of this component in a later section.

Example 2: Application to a pericratonic, mid- ramp setting (Stagner 2008)

The mid-Pennsylvanian Bird Spring Formation of Arrow Canyon, Nevada contains multiple discrete silty intervals in an otherwise carbonate cyclic succession. Paleogeographic constraints by Blakey and Knepp (1989) and others (e.g., Stevens and Stone 2007) indicate the Bird Spring Formation developed on a distally-steepened carbonate ramp in low-latitude Pangaea, isolated from fluvio- deltaic feeders (Fig. 1.1B). We sampled a mid- Desmoinesian section of the Bird Spring Formation that includes two silt- rich units.

Following the SMF extraction protocol outlined above, we analyzed ~ 8 m of this section for detrital siliciclastic influx. The results of SMF extraction indicate that weight percent of the SMF varies over two orders of magnitude through the analyzed section, from 0.32% to 53.3% for the total SMF. Placed within a sequence stratigraphic framework, the Bird Spring Formation exhibits major influxes of silt and very fine sand-sized detritus proximal to sequence boundaries (Fig. 1.4B).

The combination of physical and chemical extraction processes outlined here allow for extraction of the SMF from the Bird Spring Formation such that grain microtextures are preserved, and compositional and quantitative grain size analysis can be performed on the SMF residues. Petrographic analysis indicates that the grain-forming constituents of the SMF include quartz, potassium feldspar, muscovite and biotite, in order of decreasing mineral abundance. Heavy-mineral components including zircon, rutile, and tourmaline were observed in trace amounts during electron microprobe

analyses of the SMF. Qualitative visual and SEM analyses of residues indicate that quartz is the dominant mineral in SMF extracted from the Bird Spring Formation, and occurs as angular to sub-rounded silt-sized grains that are inferred to be detrital (Fig 5A, B), and as doubly terminated prisms inferred to be authigenic (Fig 5C, D) analogous to the Midland basin example.

The SMF of the Bird Spring Formation is coarser and more abundant compared to the SMF of the Horseshoe Atoll carbonates. These differences in amount and grain size reflect their different paleogeographic settings. The Bird Spring Formation developed on land- attached ramp wherein siliciclastic grains could have arrived via either saltation or suspension transport whereas Horseshoe Atoll was isolated within the interior Midland basin, and could have received siliciclastic material only via suspension mode, from relatively distal source areas. Hence, depending on paleogeographic settings, larger or smaller starting amounts may be more appropriate for processing.

Discussion

Sur et al (in review) noted that possible sources for silica in these systems comprise: a) fluvio-deltaic plumes; b) submarine volcanism; c) dissolution-reprecipitation of biogenic silica (sponge spicules, radiolaria, diatoms, dinoflagellates); d) diagenesis of clay; e) marine upwelling; or f) dissolution-reprecipitation of aeolian dust (continental and/or volcanic ash). However, we infer a detrital eolian origin for the authigenic quartz in both study areas on the basis of the following observations and reasoning:

As noted, both sections formed isolated from sources of fluvio- deltaic input, hence eliminating fluvio- deltaic plumes as a possible silica source. Late Paleozoic

submarine volcanism did not occur in either region, and neither section contains sufficient clay to call upon large- scale clay diagenesis as a reasonable source. Furthermore, biogenic silica components (e.g. sponge spicules, radiolaria) are extremely rare in both sections, and the few grains of biogenic silica recovered are pristine. Paleogeographic considerations (analogy with midcontinent sea; Algeo and Heckel 2008) suggest that upwelling was probably not important in the Midland basin. These considerations, together with the presence of (1) well- rounded to subangular, pitted and fractured (fine) sand- sized grains of detrital origin, and (2) common observation of fine to medium sand- sized detrital (quartz) cores within authigenic quartz lead us to infer that the major silica source for the authigenic silica was ultra fine-grained dust (continental and/or volcanic) that entered the system in association with the demonstrably detrital, coarser fraction (see also Sur et al. in review).

Furthermore, there is growing recognition of abundant loessite deposits in western equatorial Pangaea during the late Paleozoic, which suggests that this time period was characterized by abundant dust in the atmosphere (Soreghan et al. 2008). If this reasoning is valid then variations in the SMF reflect variations in the dust influx in the studied sections. Higher dust influx close to sequence boundaries is interpreted to reflect increased aridity and dust availability during glacial to incipient interglacial phases (Stagner 2008; Sur et al. in review).

Notably, Cecil (2004) argued that the majority of the Paleozoic bedded chert deposits of North America are associated with warm- arid climate regimes which produce ample amounts of highly reactive ultra- fine- grained dust. He therefore inferred aeolian

dust as the major source of silica for these bedded cherts which were otherwise thought to derive from biogenic silica.

These studies converge to suggest that dust in the pre- Cenozoic record is more important than generally realized. Although it is important to thoroughly assess the origin of any authigenic silica component, our method of extraction of SMF as a proxy for atmospheric dust has significant potential for application to the pre- Cenozoic record for paleoclimatic studies, especially given the climatic importance of aerosols.

Conclusions

1. The method described in this paper works well for the extraction of the silicate mineral fraction from Paleozoic carbonates and should be applicable to lithified carbonates throughout the geologic record. However, doubly terminated prisms of authigenic quartz can form a significant component of the extracted SMF, and its origin must be thoroughly evaluated.

2. The resultant SMF can be used as a proxy for dust and aridity for systems that formed isolated from fluvio- deltaic input and for cases wherein other, non- atmospheric sources of silica can be confidently eliminated.

3. Authigenic quartz dominates the SMF and is a common phenomenon in many ancient rocks where they are associated with arid climates and are likely sourced from atmospheric dust. This suggests a greater importance of atmospheric dust in pre-Cenozoic time than is generally realized.

Acknowledgements

The work presented here forms part of S. Sur's PhD dissertation under the supervision of G.S. Soreghan, M.J. Soreghan, R.D. Elmore, S.E. Postawko, A. Saller and T. Lyons and funded in part by grants from the American Chemical Society of the Petroleum Research Fund (PRF # 39198- AC8), the National Science Foundation (EAR-0746042), the American Association of Petroleum Geologists, the Geological Society of America, the Society for Sedimentary Geology (SEPM) Rocky Mountain Section (Donald L. Smith grant), Chevron (USA) and University of Oklahoma, Norman. Sincere thanks to A. Saller, G. Hinterlong, A. Auffant, S. Randall for help in core access and sampling. We thank T. Lyons and P. Philp for valuable discussions on geochemistry. We also thank S. Pereira, K. Marra, D. Sweet, G. Morgan, P. Larson, R. Turner and R. Maynard for analytical help. Special thank to D. Sweet for his generous help during fieldwork in Arrow Canyon.

Figure Captions

Fig. 1.1.— A) Location map of the study area (Reinecke Field) in "Horseshoe Atoll" of the Midland basin (modified after Saller et al. 1999). B) Sketch of Late Paleozoic paleogeographic elements of southwestern North America (modified after Rich, 1977, and Stevens and Stone, 2007) indicating constraints on fluvio-deltaic input to the Bird Spring shelf (Stagner 2008).

Fig. 1.2.— Photographs of different stages of residues from the Horseshoe Atoll carbonate. A) "Acid insoluble residue"; the dark color is due to presence of organic matter. B) Residue after combustion at 500 °C; note slight reddish color due to oxidation

of pyrite. C) SMF after CBD. All of the petri dishes in A), B) and C) have diameter of 5 cm. D), E), F) and G) show photographs of residue under the reflected light microscope. D) Residue after combustion at 500 °C; arrow indicates oxidized pyrite grain; horizontal field of view for photograph is ~ 5 mm. E) SMF after CBD; note absence of oxidized pyrite grains and dominance of doubly terminated quartz; horizontal field of view for photograph is ~ 2.5 mm. F) “Sand- sized SMF” after sieving (> 63 μm fraction); horizontal field of view for photograph is ~ 2.5 mm. G) “Silt- sized SMF” after sieving (<63 μm fraction); horizontal field of view for photograph is ~ 2.5 mm.

Fig. 1.3.— Flowchart for methodology to extract silicate mineral fraction from carbonate.

Fig. 1.4.— A) The stratigraphic distribution of total SMF across a sequence boundary in the Horseshoe Atoll. B) The stratigraphic distribution of SMF in the Bird Spring Formation across a mid-Desmoinesian sequence boundary and a high- frequency cycle (HFC boundary) indicates that inferred dust influx increases approximately two orders of magnitude proximal to inferred lowstand- to early transgressive intervals (Stagner 2008).

Fig. 1.5.— Reflected light and scanning electron photomicrographs of components identified in the silicate mineral fraction from the Bird Spring Shelf, showing a (A) detrital silt end-member composed primarily of (B) quartz and feldspar, and (C) an authigenic silt end-member comprised of (D) doubly terminated quartz of variable size (Stagner 2008).

References

ALGEO, T.J., AND HECKEL, P.H., 2008, The Late Pennsylvanian Midcontinent Sea of North America: A review: Palaeogeography Palaeoclimatology Palaeoecology, v. 268, p. 205-221.

ANDERSON, R.F., FLEISHER, M.Q., AND LAO, Y., 2006, Glacial-interglacial variability in the delivery of dust to the central equatorial Pacific Ocean: Earth and Planetary Science Letters, v. 242, p. 406-414.

BLAKEY, R.C., AND KNEPP, R.A.,1989, Pennsylvanian and Permian geology of Arizona, *in* Jenney, J.P., and Reynolds, S.J., eds., Geologic evolution of Arizona: Arizona Geological Society Digest, v. 17, p. 313-347.

CECIL, C.B., 2004, Eolian dust and the origin of sedimentary chert: U.S. Geological Survey Open-File Report 2004-1098, 15 p.

CLEMENS, S.C., AND PRELL, W.L., 1990, Late Pleistocene variability of Arabian Sea summer monsoon winds and continental aridity; eolian records from the lithogenic component of deep-sea sediments: Paleoceanography, v. 5, p. 109-145.

DUCE, R.A., 1995, Sources, distributions and fluxes of mineral aerosols and their relationship to climate, *in* Charlson, R.J., and Heintzenberg, J., eds., Aerosol Forcing of Climate, John Wiley, New York, p. 43-72.

HOVAN, S.A., 1995, Late Cenozoic atmospheric circulation intensity and climatic history recorded by eolian deposition in the eastern Equatorial Pacific Ocean, Leg 138, in Stewart, S.K., ed., Proceedings of the Ocean Drilling Program, Scientific Results, v.138, p. 615-625.

HYEONG, K., YOO, C.M., KIM, J., CHI, S.B., AND KIM, K.H., 2006, Flux and grain size variation of eolian dust as a proxy tool for the paleo-position of the Intertropical Convergence Zone in the northeast Pacific: Palaeogeography, Palaeoclimatology, Palaeoecology, v. 241, p. 214-223.

JICKELLS, T.D., AN, Z.S., ANDERSEN, K.K., BAKER, A.R., BERGAMETTI, G., BROOKS, N., CAO, J.J., BOYD, P.W., DUCE, R.A., HUNTER, K.A., KAWAHATA, H., KUBILAY, N., LAROCHE, J., LISS, P.S., MAHOWALD, N., PROSPERO, J.M., RIDGWELL, A.J., TEGEN, I., AND TORRES, R., 2005, Global iron connections between desert dust, ocean biogeochemistry, and climate: Science, v. 308, p. 67-71.

KOHFELD, K.E., AND HARRISON, SP., 2001, DIRTMAP: the geological record of dust: Earth Science Reviews, v. 54, p. 81-114.

LYLE, A.O., AND LYLE, M.W., 2002, Determination of biogenic opal in pelagic marine sediments; a simple method revisited, in Chapman, M., ed., Proceedings of the Ocean Drilling Program, Part A: Initial Reports, v.199, 21 p.

MAHOWALD, N., KOHFELD, K., HANSSON, M., BALKANSKI, Y., HARRISON, S.P., PRENTICE, I. C., SCHULZ, M., AND RODHE, H., 1999, Dust sources and deposition during the last glacial maximum and current climate: A comparison of model results with paleodata from ice cores and marine sediments: Journal of Geophysical Research, v. 104(D13), p. 15.895-15.916.

MAHOWALD, N.M., MUHS, D., LEVIS, S., RASCH, P., YOSHIOKA, M., AND ZENDER, C., 2006, Change in atmospheric mineral aerosols in response to climate: late glacial period, pre- industrial, modern and doubled-carbon dioxide climates: Journal of Geophysical Research, v. 111, D10202.

MEHRA, O.P., AND JACKSON, M.L., 1960, Iron oxide removal from soils and clays by a dithionite citrate system buffered with sodium bicarbonate: Clays Clay Miner, v. 7, p. 313–317.

MUHS, D.R., AND BETTIS, E.A., III, 2003, Quaternary loess-paleosol sequences as an example of climate extremes: Geological Society of America Special Publication, v. 370, p. 53-74.

REA, D.K., 1994, The paleoclimatic record provided by eolian deposition in the deep sea: the geologic history of wind: Reviews of Geophysics, v. 32, p. 159-195.

REA, D.K., AND JANECEK, T.R., 1981, Late Cretaceous history of eolian deposition in the mid-Pacific mountains, central North Pacific Ocean: Palaeogeography, Palaeoclimatology, Palaeoecology, v. 36, p. 55-67.

RICH, M., 1977, Pennsylvanian paleogeographic patterns in the western United States, *in* Stewart, J.H., Stevens, C.H., and Fritsche, A.E., eds., Paleozoic Paleogeography of the western United States, Pacific Section, SEPM, Pacific Coast Paleogeography Symposium, p. 87-111.

SALLER, A.H., WALDEN, S., ROBERTSON, S., STECKEL, M., SCHWAB, J., HAGIWARA, H., AND MIZOHATA, S., 1999, Reservoir characterization of a reefal carbonate for crestal CO2 flood, Reinecke Field, west Texas, in Hentz, T.F., ed, Advanced Reservoir Characterization for the 21st Century: Gulf Coast Section SEPM Foundation 19th Annual Research Conference, p. 259-268.

SOREGHAN, G.S., SOREGHAN, M.J., AND HAMILTON, M.A., 2008, Origin and significance of loess in late Paleozoic western Pangaea: A record of tropical cold?: Palaeogeography, Palaeoclimatology, Palaeoecology, v. 268, p. 234-259.

STAGNER, A.F., 2008, Eolian silt in upper Paleozoic carbonates of the Bird Spring Formation (Arrow Canyon, Nevada): Implications for climate controlled sedimentation, Masters Thesis, University of Oklahoma, 115 p.

STEVENS, C.H., AND STONE, P., 2007, The Pennsylvanian-Early Permian Bird Spring carbonate shelf, southeastern California; fusulinid biostratigraphy, paleogeographic evolution, and tectonic implications: Geological Society of America, Special Paper, v. 429, 82 p.

SUR, S., SOREGHAN, G.S., SOREGHAN, M.J., AND YANG, W., in review, A high-resolution record of atmospheric dust from the Pennsylvanian tropics: submitted in Journal of Sedimentary Research.

TEGEN, I., LACIS, A.A., AND FUNG, I., 1996, The influence on climate forcing of mineral aerosols from disturbed soils: Nature, v. 380, p. 419-422.

YOSHIOKA, M., MAHOWALD, N., CONLEY, A., FILLMORE, D., COLLINS, W., AND ZENDER, C., 2005, Impact of desert dust radiative forcing on Sahel precipitation (abstract): Eos, Transactions, American Geophysical Union, vol. 86, no. 52, Abstract P13B-0157.

ZIEGLER, C.L., MURRAY, R.W., HOVAN, S.A., AND REA, D.K., 2007, Resolving eolian, volcanogenic, and authigenic components in pelagic sediment from the Pacific Ocean: Earth and Planetary Science Letters, v. 254, p. 416-432.

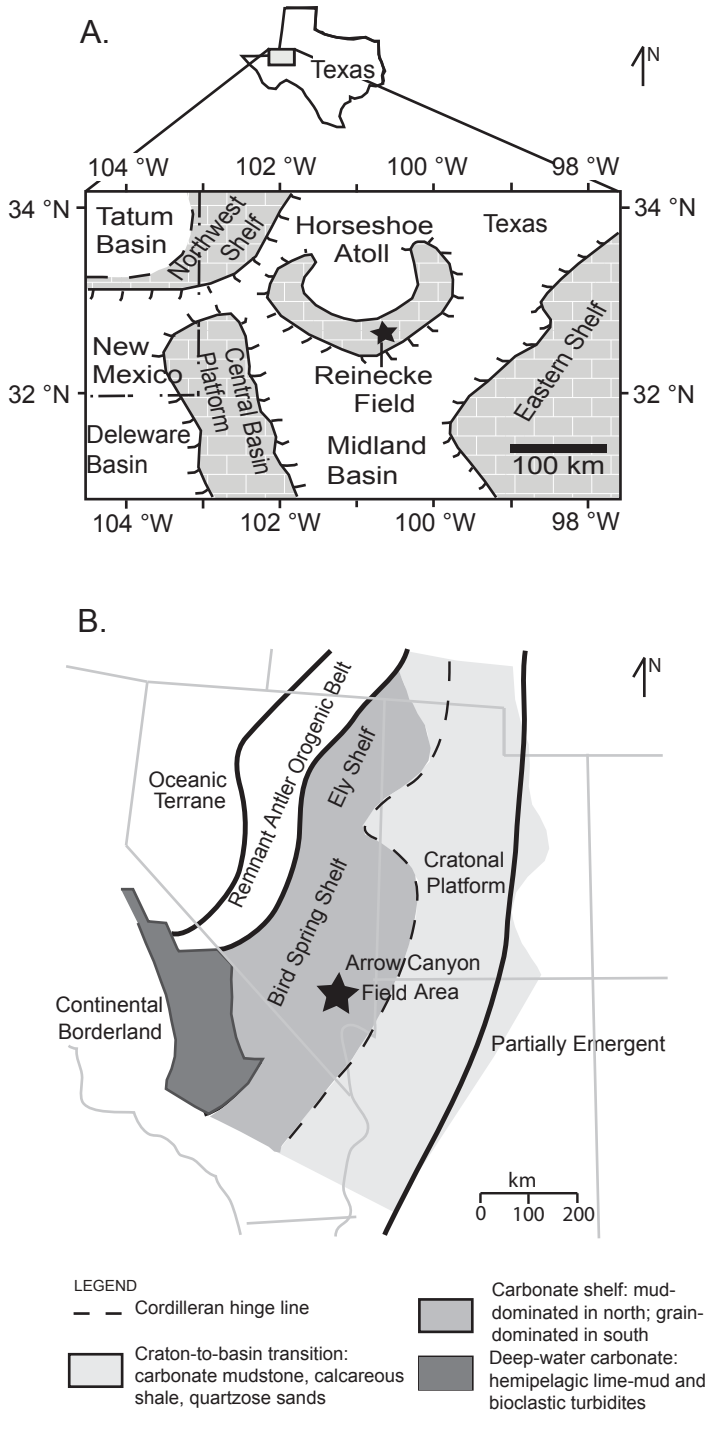
A.
Texas
N
104 °W
102 °W
100 °W
98 °W
34 °N
32 °N
Tatum Basin
Northwest Shelf
Horseshoe Atoll
Texas
New Mexico
Central Basin Platform
Reinecke Field
Eastern Shelf
Deleware Basin
Midland Basin
100 km
B.
N
Oceanic Terrane
Remnant Antler Orogenic Belt
Ely Shelf
Cratonal Platform
Bird Spring Shelf
Arrow Canyon Field Area
Continental Borderland
Partially Emergent
km
0 100 200
LEGEND
Cordilleran hinge line
Craton-to-basin transition: carbonate mudstone, calcareous shale, quartzose sands
Carbonate shelf: mud-dominated in north; grain-dominated in south
Deep-water carbonate: hemipelagic lime-mud and bioclastic turbidites

Figure 1.1

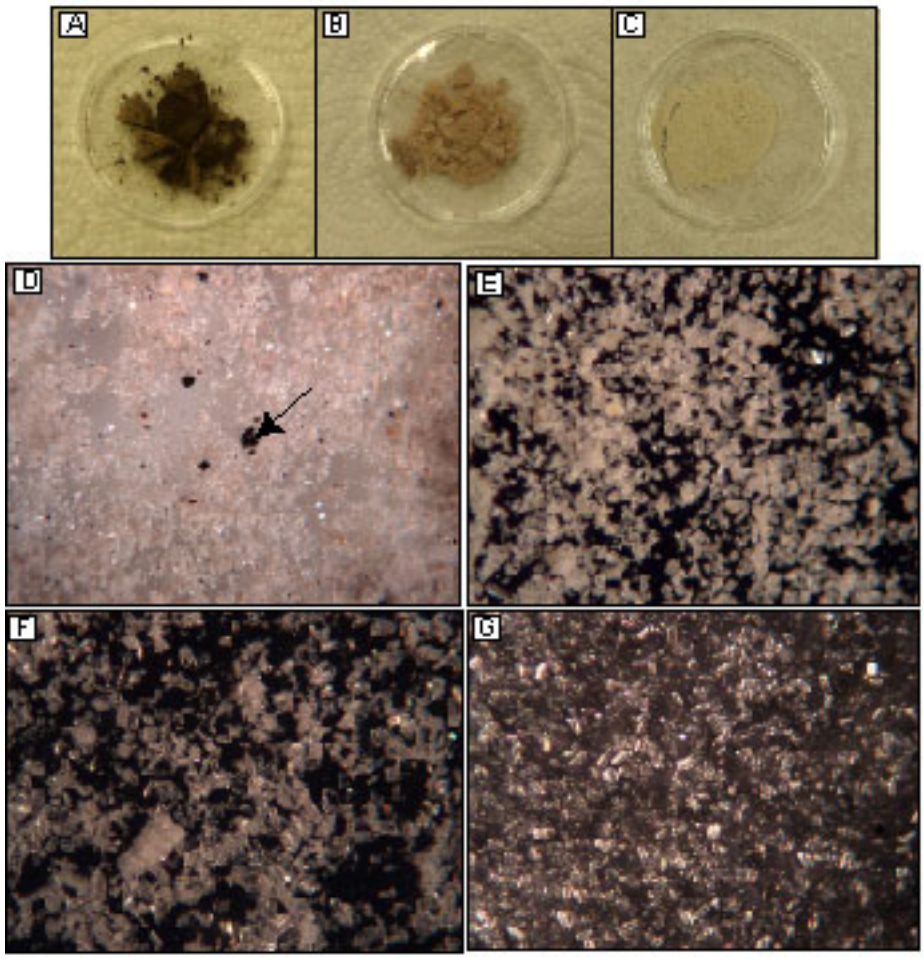

Figure 1.2

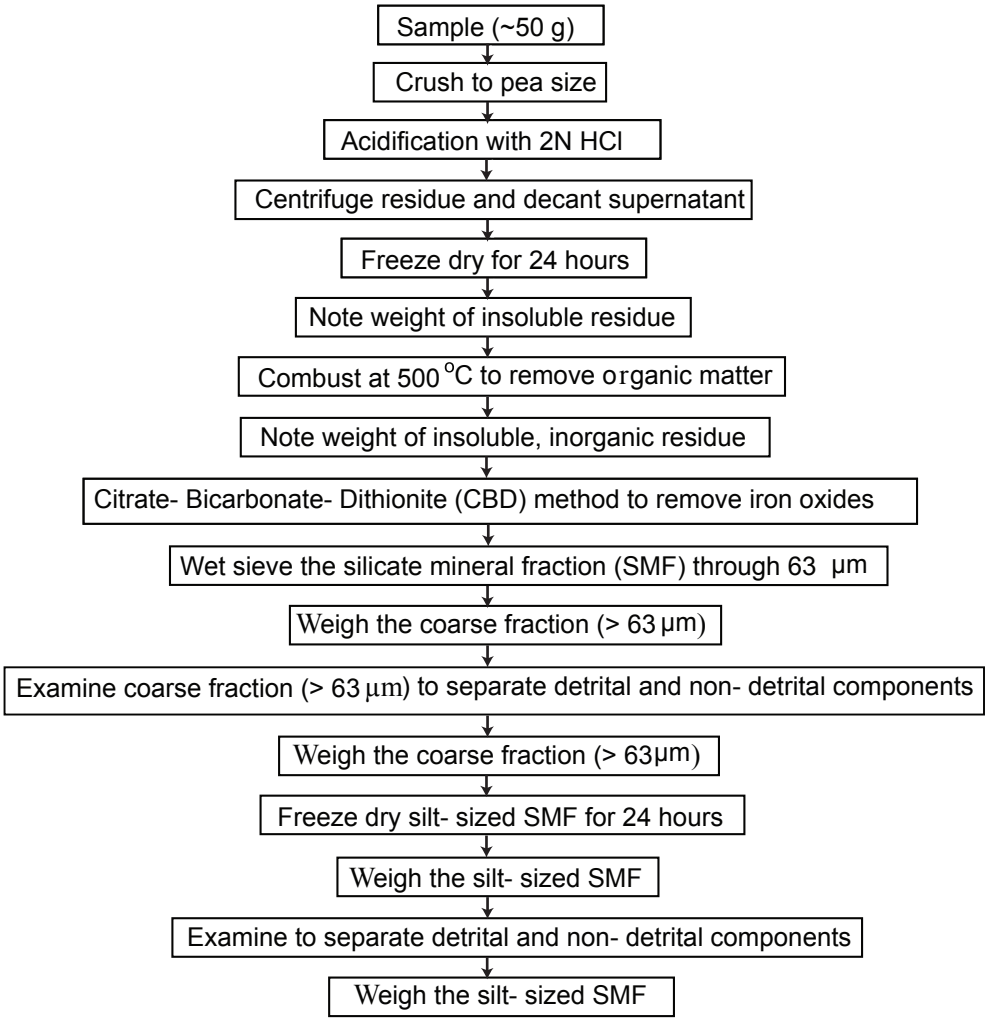
Sample (~50 g)
Crush to pea size
Acidification with 2N HCl
Centrifuge residue and decant supernatant
Freeze dry for 24 hours
Note weight of insoluble residue
Combust at 500 °C to remove organic matter
Note weight of insoluble, inorganic residue
Citrate- Bicarbonate- Dithionite (CBD) method to remove iron oxides
Wet sieve the silicate mineral fraction (SMF) through 63 µm
Weigh the coarse fraction (> 63 µm)
Examine coarse fraction (> 63 µm) to separate detrital and non- detrital components
Weigh the coarse fraction (> 63µm)
Freeze dry silt- sized SMF for 24 hours
Weigh the silt- sized SMF
Examine to separate detrital and non- detrital components
Weigh the silt- sized SMF

Figure 1.3

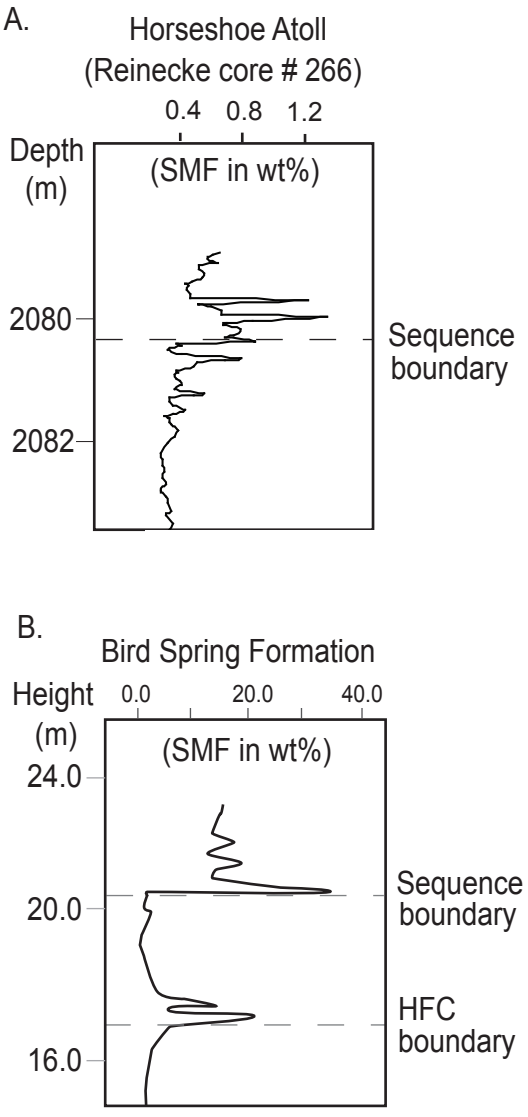
A.
Horseshoe Atoll
(Reinecke core # 266)
0.4
0.8
1.2
Depth
(m)
(SMF in wt%)
2080
2082
Sequence
boundary
B.
Bird Spring Formation
Height
(m)
0.0
20.0
40.0
(SMF in wt%)
24.0
20.0
16.0
Sequence
boundary
HFC
boundary

Figure 1.4

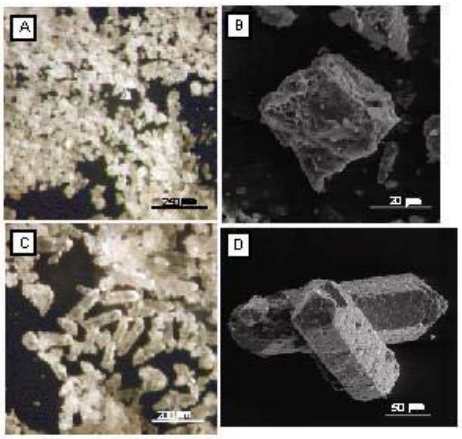

Figure 1.5

Chapter 2

A high-resolution record of atmospheric dust from the Pennsylvanian tropics

Abstract

Upper Pennsylvanian shallow- water carbonate buildups from the Midland basin consist of subtidal carbonate cycles separated from one another by exposure surfaces (sequence boundaries) that developed at glacioeustatic lowstands. These cycles consist almost entirely of carbonate, because they formed as "pinnacles" of the so –called "Horseshoe Atoll" within the middle of the basin, isolated from all fluvio- deltaic systems. However, thin (0.02 to 1 m) intervals of dark, pyritic mudrock occur commonly at sequence boundaries. In this study, by sequential removal of carbonate, organic matter and pyritic components, we isolated the silicate mineral fraction (SMF) at 10 cm intervals through a single middle Virgilian glacial cycle (~ 30 m thick). The SMF contains both (fine- grained) detrital as well as authigenic silica. We infer the origin for both components to be eolian owing to paleogeography, stratigraphic distribution, and geochemical, petrographic and grainsize characteristics and thus take the SMF as a proxy for atmospheric dust. This dust component varies in concentration over 2 orders of magnitude in the carbonate and over 3 orders of magnitude between carbonate and mudrock. The dust component is composed of quartz, clay and trace amount of feldspars and heavy minerals. The mudrock contains subtle but detectable pedogenic features such as rhizoliths, randomly oriented slickensides, clay cutans, and local carbonate nodules as well as scattered pyrite. Hence we infer the mudrock originated initially as a dust (loess)

deposit that was pedogenically modified and subsequently transgressed. Dust influx peaked in the dark gray- green mudrock (loess) deposited between the sequence boundary and the early transgressive foram/algal grainstone facies and thus suggests maximum aridity during lowstand to early transgression (glacial to incipient interglacial) time. Spectral analyses of the dust fraction within the carbonate suggest Milankovitch- scale variations in atmospheric dustiness. Provenance data suggest that dust in the studied section was ultimately derived from uplifts of the Ancestral Rocky Mountains with a possible minor contribution from active volcanic centers located to the south and southwest. Taken together our data suggest Milankovitch scale (primarily $<10^5$ yr) variations in atmospheric dust influx through carbonate (highstand) deposition and peak dustiness at lowstand to early transgression (glacial to incipient interglacial), reflecting peak aridity and dust availability during glacial time.

Introduction

In the late Cenozoic, eolian dust, preserved in both the continental (i.e. loess) and marine realm has long been recognized as a high-resolution climatic archive (e.g. Porter and An 1995; Rea et al. 1998; Muhs and Bettis 2000; Stevens et al. 2006). Increasingly, it is also viewed as an agent of climate change through its direct and indirect effects on radiative forcing (e.g. Houghton 2004) and biogeochemical cycles (e.g. Jickells et al. 2005; Mahowald et al. 1999, 2006). Late Cenozoic records of dust show that atmospheric dustiness varied on glacial– interglacial and higher frequencies, controlled by Milankovitch (e.g. Rea 1994) and sub- Milankovitch- scale cyclicity (e.g. Muhs and Bettis 2003). Relative to the Holocene, dust flux increased by an estimated 2- 20 times during the Last Glacial Maximum ~ 20,000 yrs ago; (e.g. Marino et al. 2005; Anderson et

al. 2006) probably owing to increased 1) wind strength, 2) aridity, and 3) potential dust source area (e.g. Mahowald et al. 1999, 2006).

Similar to the late Cenozoic, the late Paleozoic was also a time of large- scale glaciation. Recent research suggests the late Paleozoic consisted of multiple episodes of more- and less- intense glaciation extended over a longer time scale (several million years; e.g. Isbell et al. 2003; Jones and Fielding 2004; Fielding et al. 2008) rather than a single continuous glaciation as portrayed by various earlier workers (e.g. Veevers and Powell 1987; Crowell 1999). This late Paleozoic glaciation was characterized by periodic waxing and waning of Gondwanan ice sheets, accompanied by glacio- eustatic sea- level fluctuations ranging to high amplitudes (>100 m) during intervals of largest ice volume (e.g. Soreghan and Giles 1999), producing the classic "cyclothem" cyclicity in the rock record (e.g. Wanless and Shepard 1936; Heckel 1986). Glacial- interglacial scale and higher- frequency climate change drove and accompanied the glacioeustasy (e.g. Cecil 1990; Soreghan 1994 a, b; Rankey 1997; Olszewski and Patzkowsky 2003) and both models and data suggest that global circulation evolved from dominantly zonal to increasingly monsoonal from middle Pennsylvanian to early Permian time (e.g. Parrish 1982; Parrish 1993; Gibbs 2002; Soreghan, M. et al. 2002; Tabor and Montañez 2002). In marked contrast to the late Cenozoic, the late Paleozoic glaciation may have been, at least episodically, more extreme, as indicated by the hypothesis of low- elevation ice in equatorial Pangaea and widespread distribution of tropical loess (dust) deposits (Soreghan et al. 2008a, b).

In western equatorial Pangaea, dust deposits occur as massive and pedogenically altered siltstone or "loessite" and as marine silty units intercalated with carbonate shelf

and mound system that formed isolated from fluvio- deltaic input (Soreghan et al. 2008a and references therein). Studies from these continental loess-paleosol couplets (e.g. Soreghan et al. 2002; Kessler et al. 2001; Tramp et al. 2004) and marine strata (e.g. Soreghan et al. 2007) reveal a glacial- interglacial scale fluctuation of dust influx. Despite its widespread distribution and known importance in the climate system, climate models of the late Paleozoic have yet to incorporate the influence of dust as a climate forcing agent, primarily owing to poor constraints on the timing and character of dust fluctuation.

In this study, we document glacial- interglacial and higher- frequency fluctuations in dust influx in upper Pennsylvanian (middle Virgilian) marine carbonate of the so-called "Horseshoe Atoll," west Texas. Our data illustrate systematic fluctuations in timing, amount and character (mineralogy, grain size) of dust influx through a single glacial- interglacial cycle, reflecting Milankovitch- scale (primarily $<10^5$ yr) variations in atmospheric circulation.

Geological setting

The Midland basin of west Texas formed as a result of the collisional orogenesis between Gondwana and Laurasia during early Pennsylvanian time, when onset of the Central Basin uplift separated the ancient Tobosa basin into the Midland (east) and Delaware (west) basins (e.g. Frenzel et al. 1988). In this region tectonic activity reached its maximum during Virgilian (late Pennsylvanian) time, resulting in the continued rise of the Central basin uplift (Kluth 1986) and consequent subsidence of the Midland basin. The Midland basin remained equatorial (≤10° N) throughout the late Paleozoic (e.g. Walker et al. 1995; Scotese 2001), which led to the formation of broad carbonate shelves

along basin margins as well as isolated buildups within the basin interior (Frenzel et al. 1988; Fig. 2.1A).

The so- called "Horseshoe Atoll" forms complex buildups in the interior Midland basin, atop lower Pennsylvanian platform carbonate. It consists of a series of early Desmoinesian- to early Wolfcampian- aged phylloid- algal buildups and associated biota (e.g. bryozoa, crinoids, fusulinids, *Tubiphytes* and encrusting foraminifera) reaching up to 915 m thick (Myers et al. 1956; Stafford 1959; Vest 1970; Schatzinger 1988) and buried by lower Permian siliciclastic strata. Horseshoe Atoll now lies buried ~1830 m subsurface and is one of the most significant petroleum reservoirs of the Permian basin.

The Reinecke Field forms a pinnacle- shaped phylloid algal carbonate buildup located along the southern part of the Horseshoe Atoll. The current morphology and relief of the Reinecke structure is attributed to differential carbonate growth, followed by modification during exposure and, ultimately, deep- marine erosion upon drowning of the Reinecke buildup (Saller et al. 2004). Reinecke Field contains part of the "Canyon" (Missourian), "Cisco" (Virgilian) and "Wolfcamp" (Wolfcampian) series with four main sequences (~ 18 to 24 m thick) preserved, separated by subaerial exposure surfaces or sequence boundaries (horizons designated 100, 200, 300 and 400; Saller et al. 1999c; see Fig. 2.1B, C). The middle Virgilian strata consist predominantly (99%) of carbonate (limestone and dolostone), with <1% siliciclastic mudrock commonly found at sequence boundaries. The interval between exposure surfaces (sequence boundaries, or SB) 400 and 100 (e.g. Saller et al. 1999c) is of middle Virgilian (VC-2 of Wilde 1990) age on the basis of fusulinid biostratigraphy (Saller 1999); lower and upper Virgilian strata are

absent. The interval of interest for the current study spans a ~ 32 m middle Virgilian (Gzhelian) sequence bounded by SB 300 and 200 of Saller et al (1999c).

Methods

We studied and sampled a continuous, air- drilled core recovered from Reinecke # 266 located in Borden County, Texas (Fig 2.1A, C). The target middle Virgilian sequence was described at a centimeter scale and systematically sampled to analyze petrography, weight percent of extracted silicate mineral fraction, clay mineralogy and geochemistry. We also incorporated the work of Saller (1999) and Saller et al. (2004) to understand the depositional history and the cyclostratigraphy.

To assess the mass of the silicate mineral fraction (SMF) we collected ~ 50 g samples at 10 cm intervals throughout the study interval, and at 5 cm intervals within 20 cm of the sequence boundaries, for a total of 315 samples. We avoided sampling across stylolites. To extract the SMF, samples were treated with hydrochloric acid (HCl) to eliminate carbonate and combusted at 500° C for ~ 14 hours to oxidize pyrite and remove organic matter. Samples were then subjected to the citrate-bicarbonate-dithionite (CBD) method to remove iron oxides and subsequently sieved and visually examined. The detailed methodology is described in Sur et al. (in review b; Fig. 2.2). Sample splits of pristine core material were used to assess clay mineralogy (using X- ray diffraction, or XRD) and major and minor element geochemistry (using inductively coupled plasma mass spectroscopy, or ICP- MS). For XRD analysis, samples (3 samples) were subjected to a gentle carbonate dissolution in 0.3 M acetic acid and clay- sized residue was then extracted by the settling tube- decantation method (Folk 1974). Sedimentation slides were then made for analysis by XRD.

About 40 petrographic thin sections were studied to document the depositional facies. Reflected- light petrography, scanning electron microscopy (SEM) and microprobe analyses were also conducted to better understand the nature and origin of the SMF.

Spectral analyses on SMF data were performed using Analyseries- version 2.0.4 (Paillard et al. 1996) to assess the possible role of Milankovitch orbital- scale (eccentricity, obliquity, precession) cyclicity in the SMF data. Detailed methodology for this analysis is described in a later section.

Depositional facies

Analysis of core slabs and thin sections from the study interval revealed seven major depositional facies which are described below and summarized in Table 2.1.

Foram/algal grainstone (Fig. 2.3A, 2.4A): The foram/algal grainstone facies forms ~ 3% of the studied sequence and occurs within 0.5 m of (below and above) sequence boundaries (exposure surfaces). Allochems include fragments of algae (phylloid, dasycladacean) and forams (tubular forams and fusulinids), crinoids, bryozoans, ostracods, molluscs and brachiopods and coated and micritized grains, all very well sorted. The well- washed, grain- rich composition suggests a high- energy shallow subtidal to intertidal shoal environment for this facies. This is interpreted as the shallowest facies in the sequence.

Bioclastic grainstone (Fig. 2.3B, 2.4B): The bioclastic grainstone facies makes up ~ 30% of the studied sequence, predominantly in the upper part and consists largely of crinoid fragments with lesser amounts of fragmental tubular forams, phylloid algae,

fusulinids, bryozoans, *Tubiphytes* and brachiopods. Burrows and clay seams occur locally and stylolites are common throughout. The grain- rich fabric, with abundant fragmented allochems, and the occurrence close to the sequence top suggests deposition in a relatively high- energy shallow subtidal environment.

Bioclastic packstone (Fig. 2.3C, 2.4C): The bioclastic packstone facies composes ~ 17% of the studied sequence, predominantly in the upper half and consists of fragments of crinoids, forams (mainly fusulinids), phylloid algae, *Tubiphytes*, molluscs (e.g. gastropods) and ostracods. Near the sequence top, micritized grains and subordinate amounts of peloids and intraclasts occur. Burrows and clay seams occur locally and stylolites are common throughout. The packstone fabric, with abundant bioclasts, micritization and local peloids and intraclasts reflects moderate energy deposition in a shallow subtidal environment of <20 m depth (e.g. Soreghan 1994a; Saller et al. 2004).

Fusulinid packstone (Fig. 2.3D, 2.4D): The fusulinid packstone makes up ~ 2% of the studied sequence, occuring close to the base of the sequence and is composed of whole fusulinids with subordinate fragments of phylloid algae. Stylolites are less common in this facies. Similar to the bioclastic packstone facies, the fusulinid packstone is inferred to record shallow subtidal deposition (5-20 m depth) in open- marine conditions.

Bioclastic wackestone (Fig. 2.3E, 2.4E): The bioclastic wackestone facies composes ~ 12% of the studied sequence, occurring mostly in the middle part of the sequence and contains fragments of crinoids with subordinate fusulinids, *Tubiphytes* and phylloid algae. Clay seams are common and stylolites occur locally. The mud- rich fabric and stratal position suggest deposition in an open- marine, moderately deep subtidal

environment below wave base (≥15 to 30 m; e.g. Bishop et al. in review). This facies is inferred to be the deepest of the sequence.

Phylloid algal boundstone (Fig. 2.3F, 2.4F): The phylloid algal boundstone facies covers ~ 11% of the studied sequence, typically occuring in the middle part of the sequence. This facies exhibits a wackestone- boundstone to packstone- boundstone, autobrecciated texture and is dominated by algae (phylloid and others) with common leached and micritized phylloid algal plates. Locally, especially, above SB- 200, *Tubiphytes* and bryozoan predominate over algae. Fragments of crinoids, forams, ostracods and molluscs also occur, and stylolites are common. The boundstone fabric, presence of algae and abundant micritization indicate deposition in the photic zone (≤30 m water depth) with abundant baffling of mud.

Dark mudrock (Fig. 2.3G, 2.4G): This facies covers ~ 2% of the studied sequence (~ 0.37 m thick) typically occurring at the base of the sequence and exhibiting a very sharp contact with the carbonate facies below and above. We use the term "mudrock" to refer to non- fissile siliciclastic mudstone. To describe this facies in detail we also considered the analogous mudrock facies above SB 400. In general the mudrock facies is dark gray to greenish in color (N4 to 5G 4/1 in Munsell color scale) and lacks macrosopic bedding and fauna. Carbonate content in the mudrock facies varies from ~ 3 to 20 %. In thin section, we (Sur et al. in review b) recognize subtle pedogenic structures such as downwardly bifurcating (inferred root) traces, randomly oriented slickensides, clay cutans, rare carbonate nodules with circum- granular cracks and bright clay fabric (sepic plasmic fabric). Based on these pedogenic features the mudrock is interpreted as a paleosol; this is also consistent with its stratigraphic position directly atop carbonate

exhibiting calcrete development (see below). It also contains scattered pyrite, which we infer to reflect a marine influence. Overall, the dark gray- green mudrock, invariably associated with sequence boundaries, is interpreted to record pedogenesis of a fine-grained siliciclastic deposit, and subsequent transgression. We further examine the origin and depositional environment of the mudrock in a later section.

A dolomitized interval occurs close to the middle of the studied sequence; the dolomite is largely fabric destructive and likely formed during deep burial diagenesis (Saller 1999).

The stratigraphic column of the measured section with all facies is shown in fig. 2.5A.

Sequence- and cyclo- stratigraphy

As described by Saller et al (1999c; 2004) Virgilian (Gzhelian) strata of the Reinecke Field are predominantly carbonate and, like other Pennsylvanian strata from this region (e.g. Yang et al. 1998; Saller et al. 1999b) form repetitive successions of facies varying from 15- 30 m thick and bounded by subaerial exposure surfaces (sequence boundaries). These exposure surfaces are identified by fractures, inferred root traces, caliche layers, brecciation and negative excursions of bulk- rock stable carbon and oxygen isotope ratios (Saller et al. 2004; Dickson and Saller 2006). As described above, some cycle boundaries are marked by a thin interval of dark gray- green mudrock abruptly juxtaposed between the subjacent exposure surface and superjacent shallow water grainstone (bioclastic, foram/algal, oolitic) facies. Observation from seven cores (work of Saller 1999) of the Reinecke Field reveals that this mudrock facies varies in

thickness from 0.02 to 1 m (e.g. Dickson and Saller 2006). In general, the mudrock is thicker and more continuous above SB 400 and becomes discontinuous above successive sequence boundaries. Where the mudrock facies is absent the sequence begins with shallow- water grainstone to packstone which yields to deeper- water wackestone succeeded by photic- zone phylloid algal boundstone in the middle and is ultimately capped by shallow- water grainstone. In this sequence the upper grainstone facies is thicker than the basal grainstone facies. Saller et al. (1999c; 2004) presented a general depositional model which is consistent with our observations.

Saller's (1999) work indicates the presence of several bioclastic grainstone intervals within the Reinecke sequences. These grainstone- bounded intervals are 0.5 m-3.1 m thick and do not exhibit subaerial exposure but may represent high- frequency cycles within more major (4^{th} order) sequences.

Saller et al. (2004) inferred that each major sequence in the Reinecke Field represents a transgressive- regressive cycle. We infer that the major sequence boundaries mark the lowstand system tracts (LST) of the major sequences. The occurrences of mudrock at these major sequence boundaries are interpreted to record influx of fine-grained siliciclastic material deposited both during exposure (LST) and initial sea level rise (early transgressive system tract, TST) (see further discussion in a later section). The late TST of the low- frequency cycle is dominated by bioclastic packstone, the maximum flooding surface (MFS) is here interpreted to be marked by the deposition of bioclastic wackestone, the deepest- water facies in the sequence. During the highstand system tract (HST), the rate of change of low- frequency relative sea level decreased, resulting in progressively reduced accommodation space. Accordingly, the early to middle HST is

dominated by phylloid algal boundstone and bioclastic packstone, whereas the late HST is marked by bioclastic and foram/algal grainstone ultimately truncated by subaerial exposure that produced meteoric diagenesis during the LST.

The sequences observed in the Reinecke section are inferred to have been forced by late Paleozoic glacioeustasy, both owing to their own attributes and to regional considerations. For example, subtidal facies within the sequence are directly capped by subaerial exposure surfaces with expected intermediate facies (e.g. peritidal) missing. These types of abrupt facies changes reflect high amplitude sea- level change (e.g. Soreghan and Dickinson 1994) and are characteristic of "icehouse" carbonates (e.g. Goldhammer et al. 1991; Soreghan 1994b; Read 1995; Bishop et al. in review) formed from high- amplitude glacio- eustasy.

Furthermore, many other studies of Pennsylvanian carbonates from the greater Midland basin and surrounding regions have documented cyclic carbonate sequences inferred to reflect glacio- eustasy (e.g. Yancey and McLerran 1988; Boardman and Heckel 1989; Reid and Reid 1990; Yang et al. 1998; Yang and Kominz 1999; Saller et al. 1999b). Demonstration of high- amplitude (>80- 100 m) glacio- eustasy from age-equivalent middle Virgilian (Gzhelian) bioherms by Soreghan and Giles (1999) further supports a glacio- eustatic origin for the Reinecke cycles.

Sedimentology of the silicate mineral fraction (SMF)

SMF in the dark mudrock facies:

Petrographic study (e.g. binocular, SEM, microprobe) of the SMF of the Reinecke mudrock reveals that quartz and clay (illite) are the dominant components, followed by

muscovite, potassium feldspar, plagioclase feldspar, zircon and biotite, in decreasing abundance.

Most of the quartz is subrounded to subangular in shape; some exhibit clay coatings or pitted surface textures and are inferred to be of detrital origin. Very angular, vitreous quartz also occurs (Fig. 2.6A) and appears to reflect a volcanic origin (i.e. phenocrysts). To check that these are not a contaminant from laboratory glassware (e.g. beakers, stirring rods, pipets) we analyzed these grains under SEM attached with an EDS (energy dispersive X- ray spectroscopy) to confirm the quartz composition. Authigenic quartz does not occur in the mudrock facies. Grain size analyses of the total SMF reveals mean, median, and modal sizes of ~ 6 μm, ~ 5.5 μm and ~ 5 μm respectively (Fig. 2.5D, E, F). The clay- sized fraction, very fine to medium silt- sized fraction, coarse silt fraction and sand- sized fraction constitute ~ 43 %, ~ 46%, ~ 7% and ~ 3% of the total SMF respectively.

SMF in the carbonate facies:

Petrographic study (e.g. binocular, SEM, microprobe) of the SMF from the carbonate facies reveals quartz as the dominant component, followed by clay (illite), muscovite, plagioclase feldspar, hornblende and heavy minerals (rutile, tourmaline, magnesian chromite), in decreasing abundance.

Quartz in the SMF occurs as both doubly terminated euhedral crystals (Fig. 2.6B) and as rounded to subangular grains exhibiting pitted to fractured surface textures (Fig. 2.6C). The doubly terminated crystals are inferred to be authigenic on the basis of their morphology and the presence of host carbonate inclusions in the quartz grains, whereas the others are inferred to be of detrital origin. The doubly terminated authigenic quartz

constitutes ~ 95% (visual qualitative estimate) of the total quartz fraction in the SMF of the carbonate facies and exhibits various size ranges. Silicified fossil fragments or chert also occur, but are very rare overall. We sieved (through 63 μm) the SMF to eliminate any large chertified fraction (Sur et al in review b).The coarser sand material typically constitute a very small fraction < 10 % of the total (all- sized) SMF and nearly all of the SMF is silt- sized. The grain size analyses of the total SMF reveals mean, median, and modal sizes of ~ 18.75 μm, ~ 25.54 μm and ~ 31.3 μm respectively, and the grain- size distribution is fine- skewed (Fig. 2.5C, D, E). Similar to the SMF of the mudrock, the SMF of the carbonate facies also contains very angular, vitreous sand- sized quartz grains exhibiting concoidally fractured surface textures (Fig. 2.6D) which we similarly infer to have originated as volcanic phenocrysts. Out of a total of > 300 carbonate samples processed (representing > 15 kg of starting material), we recovered only three grains of sand- sized biogenic silica (probable radiolaria and dinoflagellates) (Fig. 2.6E, F). Plagioclase feldspar, hornblende and heavy minerals (rutile, tourmaline, magnesian chromite) together constitute <1% of the SMF. Plagioclase feldspar (much <1%) was only observed below SB 300. The euhedral habit of these feldspars indicates a probable authigenic origin. Muscovite and heavy minerals are distributed throughout the studied interval.

Stratigraphic distribution of the SMF

The amount (weight percent) of SMF in carbonate facies varies over 2 orders of magnitude (0.015 % to 6.69 %) through the studied glacio- eustatic cycle (Fig. 2.5B) [see Appendix Table 2A.1 for SMF data]. It increases at sequence boundaries (SB 300 and SB

200) and, secondarily, within shallow- water facies (bioclastic grainstone, foram/algal grainstone, fusulinid packstone, bioclastic packstone) and is very low within deeper-water facies (bioclastic wackestone). The amount (weight percent) of SMF in the mudrock varies from 81.6 to 97.6 %. Minor, high- frequency fluctuations in amount of the SMF are also evident from the SMF vs. depth plot (Fig. 2.5B). To minimize the differential compaction effect of different depositional facies on the SMF trend, we decompacted the SMF trend using Goldhammer's (1997) decompaction algorithms [see Appendix Table 2A.2A and Table 2A.2B]. However, the general trend remained the same; hence, for additional (e.g. spectral) analyses, we use the raw data in order to minimize data manipulation.

Geochemistry and provenance of the SMF

A total of 30 carbonate and 5 mudrock samples from the study section were analyzed (ICP- MS) for bulk rock geochemistry (Table 2.2 and Appendix Table 2A.3). As weathering, sorting, diagenesis and metamorphism all influence geochemical composition, we performed an element immobility test by plotting pairs of characteristically immobile elements (Al, Ti, Zr, Nb, and Y) (Fig. 2.7A, B, C). Our data suggest that Ti, Zr and Nb are relatively immobile in the mudrock and Al and Zr are relatively immobile in the carbonate facies. Some observed scatter of the data in the carbonate interval probably reflects sorting during deposition. A plot of Al/Zr with depth (Fig. 2.8B) shows that the ratio increases close to SB 300 and 200 with some variation within the sequence.

The CIA (Chemical Index of Alteration) was developed by Nesbitt and Young (1982) as a measure of chemical weathering and is a ratio of oxides = [Al_2O_3/ (Al_2O_3 + CaO* + Na_2O + K_2O)] * 100 where CaO* represents silicate- bound Ca. In this study CaO* is calculated using the equation CaO* = 0.35 * 2 * (wt% of Na_2O)/62 (e.g. Honda et al. 2004) where plagioclase components were assumed to be of average Upper Continental Crust (UCC) composition and Ca:Na ~ 1:3 (e.g. Honda et al. 2004). The plot of CIA with depth (Fig. 2.8D) also increases close to SB 300 and 200 with average values in mudrock of ~75, in carbonate close to the sequence boundary ~ 68, and in carbonate in the middle of the sequence ~ 51.

The high CIA and high Al/Zr values of the sediments close to sequence boundaries could reflect either, 1) high *in situ* weathering of carbonate during exposure or, 2) influx of fresh siliciclastic allochthonous sediment that weathered *in situ* post-depositionally or, 3) allochthonous influx of highly Al- rich materials. Within the third option there are several possibilities; a) influx of pre- weathered, clay- rich allochthonous sediments, b) influx of predominantly clay minerals owing to long- distance transport and/or weak transporting wind, c) a combination of the above. Our data show that the SMF varies from 0.19 to 2.5 % in the carbonate rock immediately below SB 300 (below the mudrock). Therefore to produce ~ 0.37 m of mudrock (SMF = 81.6 to 97.6 wt %) would require a geologically unreasonable amount (~ 200 m) of carbonate dissolution. This is very unlikely for the Reinecke field where exposure- related dissolution was minor, evidenced by an absence of major karstification (e.g. brecciation; pers. commun., A. Saller, 2008). Thus, high *in situ* weathering of carbonate as a major cause of the high CIA and Al/Zr values is unlikely and suggests an allochthonous source to explain the

high CIA and Al/Zr values. Weak development of the pedogenic structures, lack of horizonation and the change of Ti/Zr ratio through the mudrock profile (Fig. 2.8C) suggests that the high CIA and Al/Zr values near sequence boundaries are more a function of provenance than *in situ* weathering of fresh siliciclastic material. Hence, either influx of pre- weathered, clay- rich allochthonous sediments and/ or influx of exclusively clay minerals related to source distance could explain the high CIA and Al/Zr values near sequence boundaries.

Geochemical composition of shales provides valuable provenance information (e.g. Schieber 1992; Totten et al. 2000). Owing to the very low SMF content in the carbonate facies, we were unable to obtain reliable geochemical data from bulk carbonate facies. We therefore relied on the mudrock geochemistry for assessing the provenance of the SMF for the study interval. We also used geochemical data of the average upper continental crust (UCC) and Colorado Plateau Crust (CPC) (model for metasedimentary, metavolcanic and igneous rocks of ARM basement) from Taylor and McLennan (1985) and Condie and Selverstone (1999), respectively, to compare with our data.

The Th/Sc ratio provides a convenient and sensitive index of bulk composition (e.g McLennan et al. 1993). Th is incompatible and Sc is compatible in igneous processes, so Th/Sc increases with increasing magma differentiation. For UCC, the Th/Sc is 1 ± 0.1 and lower values indicate relative enrichment of compatible elements (Sc) and thus a more mafic source (Taylor and McLennan 1985). The Th/Sc ratio in the CPC is 0.25. The average Th/Sc ratio for mudstone in the Reinecke Field varies from 0.59 to 0.82, and thus may indicate contributions from both sources.

Similarly, a plot of Cr/Th vs. Th/Sc plot for shales have been used by various workers (e.g. Totten et al. 2000; Raza et al. 2002) to interpret provenance. For the studied mudrock the trace elements show (Fig. 2.9A) that composition of the mudrock is similar to UCC but includes a minor contribution from more mafic sources.

Owing to the immobile character of Al and Ti, Al:Ti ratios indicate average provenance composition (e.g. McLennan et al. 1979; Schieber 1992). The crossplot of Al_2O_3 vs. TiO_2 for the mudrock (Fig. 2.9B) is consistent with the other ratio plots discussed above and similarly indicate a mixed source.

Furthermore, presence of magnesiochromite (in carbonate) probably indicates direct derivation from an ultramafic rock or recycled derivative of these rocks. Presence of volcanic quartz and biotite (e.g. Potter et al. 2005) indicate direct derivation from volcanic ash.

Spectral analyses and periodicities of the SMF record

Similar to the late Cenozoic, many studies from the late Paleozoic have suggested a dominant Milankovitch- control for high frequency eustasy and cyclothem formation (e.g. Heckel 1986; Goldhammer et al. 1991; Yang and Kominz 1999). Therefore we applied spectral analysis to assess Milankovtich-scale (104-105 yr) periodicities in the SMF record, using Analyseries – version 2.0.4 (Paillard et al. 1996). The uncertainty in geological age always imposes the most critical challenge in accessing periodicity in rock records (Berger et al., 1991). Using age models the estimated duration of our studied section ranges from 133 to 1156 kyr and includes significant uncertainties owing to large errors associated with age dating for these upper Pennsylvanian strata (Table 2.3). This

limits the use of any one age model for time series analysis. Hence, the periodicity of SMF data was assessed using spectral analysis of SMF- depth series (SMF weight percent plotted against cumulative depth) where depth to time conversion of statistically significant peaks were done using calibration technique discussed below. Spectra of the carbonate section between SB 200 and 300 were computed, excluding the basal mudrock owing to different lithology and very high SMF values relative to the rest of the SMF dataset from the carbonate.

The SMF record shows an apparent long-term trend with relatively high values at the lower and upper parts (Fig. 2.10A, B, C, D). The strong peak of this trend at a low frequency suppressed the high-frequency peaks on the spectrum of the raw SMF record computed using the Multi-Taper method (MTM) of Thomson (1982; Fig. 2.11). Thus, the raw SMF depth series was detrended in order to analyze the high- frequency components. The middle interval (cumulative depth from 6.9 to 21.9 m) exhibits an insignificant linear trend ($R2 = 0.0001$) whereas the top and bottom sections show moderate linear trends ($R2 = 0.456$ and 0.31 respectively). The linear trends were subtracted from respective intervals to form a detrended SMF depth series (Fig. 2.10E). We also experimented various second-order polynomial detrending schemes which produced similar spectral results. To avoid excessive data manipulation, the composite depth series with linear detrending was used in subsequent spectral analyses.

Depth- SMF pairs were imported in Analyseries (Paillard et al. 1996). The spectra of the composite SMF depth series were computed using the algorithms of Paillard et al. (1996) of the Maximum entropy (ME) and Multi-taper methods (Thompson 1982; Berger et al. 1991). The two methods produced similar spectral results. MTM spectra have a

lower resolution than ME spectra, but have confidence levels independent of spectral results to allow selection of statistically-significant spectral peaks. In this study, a peak is regarded as statistically significant when its confidence level is 85% or greater (Fig. 2.12A).

The periods of statistically significant spectral peaks were calibrated using a procedure similar to that of Yang and Lehrmann (2003). The period of a Milankovitch cycle was assigned to a peak. This calibration scheme then allowed calculation of periods of other peaks. The periods were then compared with those of Milankovitch climatic cycles in late Paleozoic as predicted by Berger et al. (1992). Multiple calibration schemes were experimented. The scheme that resulted in a maximum number of Milankovitch peaks was selected (Table 2.4). The spectral configuration of the raw SMF depth series (Fig. 2.11) is similar to that of the detrended composite series (Fig. 2.12), suggesting that detrending did not contribute any spurious peaks but increased the power of high-frequency peaks.

It is well known that the dominant Milankovitch climatic forcings (i.e. eccentricity, obliquity, or precessional index) vary temporally at a specific site (e.g., Yang and Kominz, 1999; Yang and Lehrmann, 2003; and references therein). Thus, spectra of overlapping segments of the depth series were computed as evolutive spectra (Fig. 2.13) to detect any temporal changes in dominant periodicities during carbonate deposition. Evolutive spectra may also eliminate the effects of possible long-term variations in sedimentation rate (e.g., Yang and Lehrmann 2003). The calibration scheme used in calibrating the entire depth series was used to calibrate the periods of peaks on the evolutive spectra.

Six out of eight statistically-significant MTM spectral peaks from the detrended SMF depth series (Fig. 2.12A) have periods similar to those of late Paleozoic (300 Ma) Milankovitch cycles using the adapted calibration scheme. The spectral peaks with calibrated periods of 345-258 kyr and 90-79 kyr may match with the long (413 kyr) and short (123-95 kyr) eccentricity peaks (Berger, 1977), respectively; peaks at 31.8-30.8 kyr with short obliquity (34.2 kyr); and peaks at 23.2-22.2, 21.1-20.2, 16.2-15.9 kyr with precessional index (20.7 and 17.4 kyr) peaks (Berger et al., 1992). The remaining two statistically-significant non-Milankovitch peaks have periodicities at 11.5-11.3 kyr and 55-51 kyr, respectively. The 11.5-11.3 kyr peaks may be that of the 9.7-kyr constructional tone of short and long precessional index cycles as detected by Yang et al. (1995) and Yang and Lehrmann (2003) in cyclic shallow platform-carbonate successions. The periods of these peaks are also within the range of non-Milankovitch spectral peaks (15.4-10.8 kyr) caused by non-linear response with combination of forcing frequencies (Berger et al. 1991). The 55-51-kyr peak may be the ~ 50-80-kyr peaks as the combination tone of short and long precession index with short obliquity cycles (Yang and Kominz 1999). Berger (1977) also predicted some non-Milankovitch periodicities (e.g., 50, 54, 59 and 64 kyr) in geologic records due to combination of two or more Milankovitch periodicities which may be represented by 51-55-kyr peaks in the SMF spectra.

The spectral results and calibration of MTM spectral analyses are supported by the results of ME spectral analysis. The uncertainties in the period calibration of SMF spectral peaks against Milankovitch cycle periods may be attributable to various depositional and diagenetic factors that could have distorted or altered any original

Milankovitch climatic signals in the SMF record. Diagenetic processes, such as selective formation of stylolites and Dolomitization and differential compaction among carbonate facies. The six different carbonate depositional facies may have had different sedimentation rates, which invalidate the assumption of a uniform sedimentation rates for all facies in our spectral analyses (Yang et al. 1995; Yang and Lehrmann 2003; Yang et al. 2004). The limited length of the SMF record may prevent confident delineation of long-eccentricity cycles. Nonlinear transformation of Milankovitch climatic forcing by sedimentary processes, long-term variations of sedimentation rate and associated sedimentary processes together with the chaotic nature of the orbital forcing may also contribute to the uncertainties in period calibration. Finally, many other autogenic and allogenic non-Milankovitch processes (e.g. volcanic input) active during the formation of the SMF record further complicates the spectral characteristics.

The average sedimentation rate of the SMF record was estimated from the adapted period calibration as 4.9 cm/kyr. It is similar to the lower limit of estimated effective sedimentation rate (7 cm/kyr) of Virgilian-Wolfcampian carbonate rocks in the adjacent Eastern Shelf (Yang and Kominz 1999), and to the estimated accumulation rate of Strawn (3.3 cm/kyr) and Cisco (1.4 cm/kyr) carbonates on the Central Basin Platform (Saller et al. 1999b). The estimated duration of the studied sequence computed by dividing sequence thickness (23.88 m) by the average sedimentation rate is ~ 483 kyr. However, this value does not incorporate the time involved during exposure represented by the mudrock. In a study from approximately coeval strata of the upper Paleozoic Central Basin platform, Saller et al (1999c) used the intensity of early diagenesis and porosity evolution to estimate an exposure duration of 5 to 50 kyr. Similar attributes, and

hence intensities, prevail in the studied exposure surfaces. Using Saller's values for exposure, the estimated duration of the studied sequence is 488 to 533 kyr which falls within the range of age models (133 to 1156 kyr; Table 2.3) for the studied sequence. Our results, which yield, 1) a dominance of statistically significant Milankovitch- related peaks, 2) a reasonable sedimentation rate, and 3) age relations that approximate published age models suggest that the adapted calibration scheme is reasonable and Milankovtich precessional, obliquity and eccentricity signals are present in the SMF record.

The evolutive spectra (Fig. 2.13B to I) clearly demonstrates varying dominance of forcings of precessional index, obliquity, and short-eccentricity during the formation of the SMF record. Short precessional index and obliquity signals are significant in the lower 7.5 m, which evolved to short eccentricity and precessional index signals in overlying 7.5-15-m section. Precessional index and short obliquity signals become predominant again in the 12.5-20-m interval, followed by significant short eccentricity, short obliquity and short precessional index signals in the 17.5-22.5-m interval. The spectra for the 20-25-m interval is incomplete and cannot further evaluated. The evolving Milankovitch forcings suggest that during incipient interglacial time (lower section, Fig. 2.13I and J) SMF periodicity was mainly controlled by precessional index and obliquity cycles, whereas during the interglacial time (middle section, Fig. 2.13F and G) SMF was controlled by short eccentricity and precessional index cycles, followed by the dominance of short eccentricity, obliquity and precessional index cycles during interglacial to incipient glacial time (upper section, Fig. 2.13C, D and E). The dominance of Milankovitch orbital forcing in the SMF composite data as well as in the evolutive spectra suggests that high-frequency fluctuations of the SMF were probably controlled, at

least in part, by varying strength of Milankovitch precessional, obliquity and short eccentricity forcings, and the long- term trend in SMF was probably controlled by long eccentricity forcing through the glacial-interglacial cycle.

Origin of the SMF

Origin of the sequence- bounding mudrock:

Several possibilities exist for the origin of the SMF in the studied rocks: a) fluvio-deltaic input through distal turbidite plumes; b) concentration of insoluble residue by dissolution of host carbonate rock; or c) deposition by aeolian dust (continental and /or volcanic origin). We assess each of these below.

a) Fluvio- deltaic input via distal turbidite plumes: Horseshoe Atoll of the Midland basin was an isolated carbonate buildup surrounded largely by basin- rimming carbonate shelves during Virgilian (Gzhelian) time. The contemporaneous fluvio-deltaic system was present in the western (Central Basin platform) and eastern part (Eastern shelf) of the basin, which prograded basinward (up to ~ 100 km, Fig. 2.14A, B) during lowstands to feed submarine fan systems of the deep basin (e.g. Cleaves 2000). Within Horseshoe Atoll, however, lowstand intervals are recorded by exposure surfaces developed atop subtidal carbonate and the mudrock is juxtaposed between the sequence boundary and the early transgressive foram/algal grainstone. Hence, the timing of deposition of the mudrock precludes an origin via fluvio- deltaic plumes.

b) Concentration of insoluble residue by dissolution of host carbonate rock: As noted previously, our SMF data demonstrate that the carbonate strata in the studied system are typically very pure (typical residue values are < 0.5%). Therefore, formation

of the mudrock via dissolution would require geologically unreasonable amounts of limestone dissolution (nearly 200 m) and thus can be ruled out.

c) Deposition by aeolian dust (continental and /or volcanic origin):

Volcanic dust: The presence of very angular, vitreous quartz, together with biotite grains in the mudstone suggests derivation from a volcanic source (e.g. Potter et al. 2005) as noted above. Moreover, mixed felsic (predominate) and mafic (subordinate) composition of the mudrock provenance, together with the presence of coeval volcanism in the greater region (Fig. 2.14A, B), notably the Las Delicias volcanic arc of northern Mexico (e.g. Lopez 1997) further supports the possibility of a volcanic dust contribution to the study section. Such a mechanism, however, would produce influxes of silicate material at random intervals; in contrast, the pattern of our SMF data appears non-random, and possibly periodic. Hence, we reason that volcanic dust, although present, cannot be the major component of the SMF.

Continental dust: The presence of numerous subrounded to subangular detrital quartz grains and a mean particle size of fine silt (~ 6 μm), which is readily transportable by wind, suggests that windblown dust forms a major proportion of the SMF. This is consistent with the growing recognition of aeolian dust deposits (loessite) in late Paleozoic western equatorial Pangaea (e.g. Soreghan et al. 2008a and references therein).

Origin of the SMF in the carbonate

As discussed earlier, the SMF in carbonate facies is dominated by authigenic quartz (Fig. 2.6G) which could ultimately derive from various sources as follows: a) fluvio-deltaic plumes; b) submarine volcanism; c) dissolution-reprecipitation of biogenic

silica (sponge spicules, radiolaria, diatoms, dinoflagellates); d) compaction of associated siliciclastic facies; e) marine upwelling; or f) dissolution-reprecipitation of aeolian dust (continental and/or volcanic ash).

a) Fluvio- deltaic plume: The contribution of material from fluvio- deltaic plumes can be ruled out for the SMF in carbonate facies for the reasons forwarded above, i.e., the isolation of the Horseshoe Atoll from any fluvio- deltaic input, and the trapping of siliciclastics landward during transgression.

b) Submarine volcanism: Submarine volcanism has never been reported from the Midland basin and thus is not considered a viable source for silica.

c) Biogenic source (sponge spicules, radiolaria, diatoms, dinoflagellates): In our analysis of > 300 carbonate samples through the study interval, representing ~15 kg of material, we have found only 3 grains of biogenic silica (radiolaria and suspected dinoflagellates, Fig. 2.6E, F). No sponge spicules have been observed in thin section, nor in the SMF. Furthermore, siliceous spicules, which are more characteristic of slope facies, are very rare overall in strata of the studied sequence (pers. commun., A. Saller 2009). Moreover, it is difficult to explain the systematic trend of the SMF by biogenic silica, which is otherwise absent or randomly distributed.

d) Clay diagenesis: An allochthonous source of silica for the authigenic component could derive from transformation of smectite to illite during burial diagenesis. Although thick shales occur in the basinal facies, derivation of silica in this manner is unlikely for the following reasons. Such migration of silica- rich fluids would likely exploit permeable conduits such as fractures and porous facies. Yet, authigenic quartz is distributed throughout all facies, with no lenses of authigenic quartz and no preferential

occurrence in the most permeable facies (e.g. phylloid algal boundstone facies, e.g. Saller et al. 2004). Furthermore, systematic trends in oxygen and carbon isotope values across the sequence boundaries and their correlation across the other wells of the region (Saller 1999; Dickson and Saller 2006) do not support the possibility of major silica- rich fluid migration. The slightly higher values of $^{87}Sr/^{86}Sr$ (average 0.70837) near the mudrock of SB 300 relative to coeval marine carbonate (~ 0.70830) may reflect a minor contribution from clay mineral diagenesis of the mudrock above SB 300 (pers. commun., T. Rasbury, 2008). However, this would not provide a significant source of silica to explain the general trend of the SMF (Fig. 2.5B, C, D, E), as authigenic quartz is distributed throughout the section and high enrichment also occurs close to the sequence boundary lacking associated mudrock (SB 200). Finally, clay mineral diagenesis from clay within the carbonate facies is a very unlikely source of silica because clay generally composes <0.5% of the carbonate rock.

e) Marine upwelling: Silica can also be supplied by marine upwelling as upwelling brings cold, nutrient- rich water from intermediate depths to surface depths. The multiple basins of the ARM system and islands within the Midland basin area (Fig. 2.14A, B) during late Pennsylvanian time, however would have made it difficult to generate conditions favorable for upwelling (Parrish 1982). Paleogeographic analyses indicate modeled upwelling zones were far from regions of bioherm development (e.g. Midland basin) (Kiessling et al. 1999). Similarly, Algeo and Heckel (2008) also argued against upwelling as a major mechanism in epeiric late Pennsylvanian seas of western/ midcontinent North America owing to the paleogeographic setting and the absence of

high primary productivity. Hence, upwelling as a major silica source in this area seems unlikely.

f) Dissolution- reprecipitation of eolian- sourced (continental and/or volcanic) material:

Volcanic dust: The presence of suspected volcanic phenocrysts (of quartz) and relative proximity (< 500 km) of Horseshoe Atoll to active volcanism associated with the Ouachita- Marathon suture zone and Las Delicias volcanic arc (e.g. Lopez 1997) allow the possibility of volcanic dust as a source of authigenic silica. Such a source should have been random through time, however. Hence, we reason that volcanism could not be the major source of silica in the study section as it can not explain the observed trend of SMF enrichment preferentially near sequence boundaries.

Continental dust: Well- rounded to subangular abraded, pitted, fractured sand- sized quartz grains of detrital origin occur throughout the section, with the highest concentration close to sequence boundaries. Thin section studies indicate that most of the authigenic quartz occurs as individual crystals disseminated in the carbonate matrix, with some of the larger doubly terminated quartz near sequence boundaries (exposure surfaces) consistently exhibit fine to medium sand- sized detrital (quartz) cores (Fig. 2.6H, I, J). These types of detrital grains reflect a continental derivation. Corrosion along their boundary (Fig. 2.6J) suggests they act as nuclei for authigenic quartz growth. If this true, then the associated very fine- grained dust fraction, being more chemically reactive, would have served as a source for authigenic silica (Cecil 2004). This hypothesis is supported by the grain-size distribution histograms, which show a very fine-grained (typically < 4 μm) population present within the mudrock but missing within the

carbonate (Fig. 2.5C, D, E). This fine-grained background dust component should have been present throughout carbonate deposition as well, so its absence merits explanation. We hypothesize that this very fine-grained, chemically reactive fraction underwent early post-depositional dissolution and reprecipitation in the alkaline marine (carbonate-precipitating) waters, producing the coarser authigenic silica that dominates the SMF fraction within the carbonates. Moreover, the inferred Milankovitch periodicities observed in the SMF data of the carbonate are difficult to explain by any possible source of silica other than climatically influenced variations in eolian dust, ultimately sourced from continental dust with an occasional volcanic input. Recent recognition of abundant eolian dust deposits (loess) in western equatorial Pangaea during late Paleozoic time (see references above) and recognition of dust as a potential source for Phanerozoic bedded chert (Cecil 2004), lend further support for this hypothesis.

From the above reasoning we conclude that the mudrock of the study section represents loess (eolian dust) that accumulated primarily during subaerial exposure and was subjected to pedogenesis. Presence of scattered pyrite in the mudrock suggests marine reworking of the pedogenically modified loess during transgression. Aggradational soils are common in Quaternary strata where aeolian dust constitutes much of the pedogenic material (e.g. Jacobs and Mason 2007; Muhs et al. 2007).

Provenance of dust and wind direction

As discussed previously, geochemistry of the mudrock samples approximates both UCC and CPC compositions. Hence, depending on wind direction, possible source areas for the mudrock (and by extension, SMF) include: 1) lowstand (exposed) alluvial/

deltaic deposits to the east, southeast, south and southwest of the Horseshoe Atoll (Fig. 2.14A), ultimately derived from metasedimentary/ metavolcanic and granite/ gneissic rocks of the Amarillo- Wichita- Arbuckle uplift (part of ARM), 2) ARM uplifts to the north, northwest and west, or 3) coeval loess deposits located to the north and northwest and west (e.g. noted in Soreghan et al. 2008a).

Presence of volcanic quartz indicate direct derivation from a source of active volcanism. Active volcanism existed to the south- southwest, e.g. the Las Delicias volcanic arc of northern Mexico (e.g. Lopez 1997) which is also considered a possible source for middle Permian ash beds of the Cherry Canyon sandstone of the Guadalupe Mountains and subsurface equivalents (e.g. Nicklen et al. 2007). Therefore, it seems most likely that the volcanic components in the SMF were derived from this south-southwestern source.

Additionally, the presence of magnesiochromite (in carbonate) suggests direct derivation from, and/or a recycled derivative of, an ultramafic rock. Depending on wind direction, possible source areas for the magnesiochromite include: 1) exposed obducted oceanic crust of the southern Ouachita Mountains (e.g. Totten et al. 2000), or 2) the south- southwestern Coahuila and Sierra Madre terranes of Mexico (e.g. Centeno-Garcia 2005).

During Virgilian (Gzhelian) time the Midland basin was close to the equator (0° to 5°) (Fig. 2.14A, B) and Walker et al (1995) inferred that wind patterns were zonal easterlies. However, seasonal swinging of the ITCZ (intertropical convergence zone) could have produced variable wind directions from southeasterlies in the northern hemisphere summer to northeasterlies in the northern hemisphere winter. Most recent

studies in western equatorial Pangaea suggest a dominantly zonal circulation pattern during Desmoinesian (middle Pennsylvanian) time and monsoonal circulation by earliest Permian time (e.g. M.J. Soreghan, et al. 2002; Tabor and Montañez 2002). Given monsoonal circulation in western equatorial Pangaea, the dominant winds would have been westerlies during the northern hemisphere summer and southeasterlies during the northern hemisphere winter (e.g. M.J. Soreghan et al. 2008). Data from the late Paleozoic Cutler Formation (western equatorial Pangaea; M. Soreghan, unpublished) indicate a probable transitional wind regime between dominant zonal and monsoonal circulation during Virgilian (Gzhelian) time. In all scenarios of wind regime (zonal, transitional and monsoonal), Horseshoe Atoll should have experienced south- southeasterlies, consistent with our provenance data and consistent with the inference of a volcanic dust input from the south and southwest. However, deciphering among the other potential sources from the north, northeast or west is more difficult without additional provenance data (e.g. detrital- zircon provenance study, Sm- Nd isotope study).

Timing of dust influx and relation to climate change

From the previous discussion, variation in the amount of SMF in the study section provides an indicator of atmospheric dustiness that varied at both glacial- interglacial and higher frequency ($<10^5$ yr) scales, related to waxing and waning of ice sheets controlled, at least in part, by Milankovitch- scale cyclicity. Various studies from low latitudes of late Paleozoic North America have noted links between inferred glacioeustasy and glacial- interglacial scale climate change (e.g. Cecil 1990; Soreghan 1994a, b; Rankey 1997; Olszewski and Patzkowsky 2003). However, the timing of climate change with

respect to sea level remains debated. While some suggest low- latitude arid climate during glacial lowstand and humid climate during interglacial highstand (e.g. Soreghan 1994 a, b; Rankey 1997; Olszewski and Patzkowsky 2003; Tramp et al. 2004; Soreghan et al. 2007), others have inferred the opposite (e.g. Miller et al. 1996; Cecil et al. 2003).

The position of the Horseshoe Atoll in the interior of the Midland basin combined with rapid subsidence of the basin during Virgilian (Gzhelian) time (e.g. Waite 1993) would have allowed subaerial exposure in the study section only during the late stage of relative sea level fall (Rankey 1997). In the study section minimal amounts of dust (SMF) occur within deeper- water carbonate facies and dust increases within shallow- water facies near sequence boundaries. This suggest that, during interglacial (highstand) phases, climate of the source region experienced more humid conditions, enabling chemical weathering of the source material and lower dust influx to the study area. Arid conditions and expansion of regions of eolian deflation during sea- level fall and ensuing glacial lowstands likely allowed mobilization of weathered material (dust) present from the previous interglacial, as indicated by high CIA and high Al/Zr values near sequence boundaries. The high amount of SMF (inferred dust) at lowstands could also reflect the lack of carbonate deposition during lowstands, and consequent lack of dilution of the dust by carbonate accumulation, especially if the mudrock represents a long-duration interval. However, this alone cannot explain our data, in part because the SMF (dust) content in the shallow-water carbonate facies immediately below the sequence boundary also exhibits large (1 to 2 orders of magnitude) increases relative to the deeper-water facies (Fig. 5B). These increases are more than possible variations in effective carbonate sedimentation rate (1 order of magnitude; Yang and Kominz 1999),

and in fact oppose trends expected from changes in sedimentation rate alone, owing to the relatively greater sedimentation rates in shallow-water facies. Hence, even after considering the possible effects of changes in sedimentation rate we cannot account for the increase in SMF content without calling upon increased delivery of dust to the system at sea-level fall and lowstand. We thus infer greater aridity and dust availability during sea-level fall, lowstand (and early transgression) which corresponds in general to the glacial phase (Fig. 2.15A, B; Table 2.5).

These results are similar to atmospheric dust fluctuations inferred from the Quaternary ice-core record (e.g. Petit et al. 1999). As, noted earlier, dust flux was 2 to 20 times higher than the Holocene during the Last Glacial Maximum (LGM; 20 kyr ago). To compare the dust influx in the studied section with the LGM, we estimated the mass accumulation rate (MAR; e.g. Rea and Janecek 1981) of the dust component in the carbonate assuming a linear sedimentation rate (LSR) of 4.9 cm/kyr (estimated from spectral analysis for the carbonate) and a density of 2.65 g/cm^3. Initial porosity for the various carbonate facies are taken from Goldhammer (1997; see Appendix Table 2A.2B). Estimated MAR in the carbonate just below the exposure surface suggests that dust flux was typically 4 to 10 times higher during sea- level fall relative to interglacial time. This in turn suggests that dust flux was at least 4 to 10 times higher during the shift to glacial time relative to interglacial time. The character of the sequence- bounding pedogenesis, marked by minor pedogenic carbonate (within the mudrock) and lack of evidence for major dissolution (karstification; pers. commun., A. Saller 2008) support this inference of increased aridity at lowstand, although the vertic features within the pedogenically

modified loess (Sur et al. in review a) suggest some seasonality of climate in the overall drier glacial climate.

The glacial- interglacial and higher frequency (< 10^5 yr) variations in dust influx, recorded in our data and elsewhere from late Paleozoic equatorial Pangaea, probably had significant effects on radiative forcing and biogeochemical cycles and thus on the climate system (Soreghan and Soreghan 2002; Soreghan et al. 2008a, b; Sur et al. in review a), a hypothesis that merits further testing.

Conclusion

1) The silicate mineral fraction (SMF) extracted from carbonate rocks that formed isolated from fluvio- deltaic input can be used as a proxy for atmospheric dust influx, which is an indicator of various climatic parameters e.g. aridity, source area, atmospheric circulation and atmospheric dustiness.

2) In the study area, dust influx varied significantly >10^2 times in the carbonate in glacial- interglacial and higher scale (<10^5 yr).

3) Higher scale (<10^5 yr) variations in dust influx within the carbonate were probably controlled, at least in part, by precession, obliquity and short eccentricity influences on climate whereas the glacial- interglacial scale variation was probably controlled by long eccentricity variations.

4) Dust influx and thus aridity and atmospheric dustiness peaked at sea level fall, lowstand and early transgressive phases (glacial to incipient interglacial) and were lowest during late transgression to highstand time (interglacial). During climatic transition from

interglacial to glacial, dust flux was typically 4 to 10 times higher than during full interglacial phases, similar to inferences for the LGM.

Acknowledgements

The work presented here forms part of S. Sur's PhD dissertation under the supervision of G.S. Soreghan, M.J. Soreghan, R.D. Elmore, S.E. Postawko, A. Saller and T. Lyons and funded in part by grants from the American Chemical Society of the Petroleum Research Fund (PRF # 39198- AC8), the National Science Foundation (EAR-0746042), the American Association of Petroleum Geologists, the Geological Society of America, the Society for Sedimentary Geology (SEPM) Rocky Mountain Section (Donald L. Smith grant), Chevron (USA) and the ConocoPhillips School of Geology and Geophysics at the University of Oklahoma, Norman. We thank A. Saller, G. Hinterlong, A. Auffant, S. Randall for help in core access and sampling. Special thank to W. Yang for his continuous help in spectral analyses. Many helpful discussions with A. Saller, D. Elmore, L. Hinnov, T. Rasbury, P. Wright, P. Knauth, T. Lyons and V. Davydov contributed to the development of our work. We also thank S. Pereira, K. Marra, D. Sweet, G. Morgan, P. Larson, R. Conlon, R. Turner, R. Maynard and P. Roy for analytical help.

Figure captions

Fig. 2.1.—A) Location map of the Reinecke Field, Horseshoe Atoll and Midland basin. B) Chrono- stratigraphy of the late Paleozoic showing both global and regional stages

(modified after Saller et al. 1994; Wilde 1990; Gradstein et al. 2004). C) Generalized stratigraphy of the Reinecke Field (modified after Saller 1999).

Fig. 2.2.—Flowchart for methodology to extract silicate mineral fraction from carbonate (Sur et al. in review a).

Fig. 2.3.—Core photographs of depositional facies. A) Foram/algal grainstone just below sequence boundary. Note rhizoliths (e.g. arrow). B) Bioclastic grainstone with abundant fragmented crinoid grains (arrow). C) Bioclastic packstone. D) Fusulinid (arrow) packstone. E) Wavy bedded bioclastic wackestone. F) Autobrecciated texture of the phylloid algal boundstone. G) Dark gray- green mudrock just above sequence boundary 300 (arrow).

Fig. 2.4.—Photomicrographs of depositional facies. Horizontal field of view for A, B, C, D, E and F are ~ 3 mm. A) Dasyclads and forams in foram/algal grainstone with abundant pyrite (opaque grains). B) Bioclastic grainstone with dominant crinoid fragments. C) Bioclastic packstone. D) Fusulinids in the fusulinid packstone. E) Very sparsely fossiliferous bioclastic wackestone. F) Micritized phylloid algal plate in the phylloid algal boundstone. G) Dark gray- green mudrock; horizontal field of view is ~ 8 mm.

Fig. 2.5.—A) Litho-stratigraphic section of the study interval (core #266 from Reinecke Field) covering SB 300 and SB 200. B) Total SMF raw data. C), D) and E) are grain- size curve of total SMF of the mudrock and carbonate, illustrating the fine skewed population.

Fig. 2.6.—Photomicrographs of the SMF. A) SEM view of angular, clear quartz with conchoidal fracture surfaces. B) SEM view of a doubly terminated (authigenic) quartz grain. C) SEM view of a rounded and pitted sand- sized quartz grain. D) SEM view of a shard- like angular detrital quartz grain. E) SEM view of a probable radiolarian. F) SEM view of a suspected dinoflagellate. G) SEM view of a doubly terminated authigenic quartz and clay in the SMF of carbonates. H) Thin section view of a doubly terminated authigenic quartz grain with a detrital core; horizontal field of view is ~ 0.6 mm. I) SEM view of nucleation of authigenic quartz on a detrital quartz grain. The detrital quartz exhibits clay coating. J) Thin section view of a doubly terminated authigenic quartz grain with a detrital core; horizontal field of view is ~ 0.6 mm. Arrow indicate dissolution along the edges of detrital core.

Fig. 2.7.—A) Crossplot of Ti vs. Zr for mudrock. B) Crossplot of Nb vs. Zr for mudrock. C) Crossplot of Al vs. Zr for carbonates. See text for discussion.

Fig. 2.8.—A) Generalized stratigraphy of the study section. B) Al/Zr. C) Ti/Zr within the mudrock. D) Chemical Index of Alteration (CIA). See text for discussion.

Fig. 2.9.—A) Crossplot of Cr/Th vs. Th/Sc for mudrock samples (diamond symbol). B) Showing crossplot of Al_2O_3 vs. TiO_2 for mudrock samples (diamond symbol). The "granite", "6 granite+ 1 basalt", "3 granite+ 1 basalt" and "basalt" lines are plotted from McLennan et al. 1979. For both diagrams, UCC = upper continental crust; CPC = Colorado plateau crust and UPL = upper Paleozoic loess. The data for UPL is taken from Soreghan and Soreghan (2007).

Fig. 2.10.— A) Raw data (All- sized SMF) are plotted against cumulative depth (m) showing long term trends. Dashed lines mark depths with different trend patterns used to split the series in three intervals. Three regression equations, B, C, D corresponding to depth range B) >21.9 m, C) 6.9-21.9 m and D) <6.9 m are computed. E) Detrended data (All- sized SMF) is computed by subtracting trends from raw data.

Fig. 2.11.— SMF spectrum computed on raw- SMF data resampled at an equal interval of 5 cm, finer than physical sampling interval (~10 cm).by MTM-Multi taper method of Thompson (1982) with its significance level. Time periods (in kyr) corresponding to some statistically significant (greater than 85% significance level) peaks are also given.

Fig. 2.12.— A) SMF spectrum computed on detrended-SMF data resampled at an equal interval of 5 cm, finer than physical sampling interval (~10 cm).by MTM-Multi taper method of Thompson (1982) with its significance level. B) SMF spectrum computed on detrended-SMF data by Maximum entropy (ME) method. The frequency (0.009776) marked by star is calibrated with the long precession cycle at 20.7 Kyr and all other peaks

are computed based on the calibrated peak. Time periods (in kyr) corresponding to some prominent peaks are also given. Statistically significant Peaks (greater than 85% significance level) are marked by thick vertical lines.

Fig. 2.13.— A) Raw SMF data are plotted with depth (m) showing long term trends. B-J: Evolutive spectra of detrended- SMF data. A window of 500 cm with and overlap of 250 cm is considered to create nine overlapping data series. B to J: for each of the series spectra are computed (solid dark lines) by MTM method of Thompson (1982) with its significance level (dashed line). MTM Amplitudes estimates are marked along left side where as significance levels are marked along the right side of the Y axis. Dashed vertical lines are Milankovitch line spectra for ~ 300 Ma (Berger et al. 1992) and constructional tone. Star marks the calibration frequency. Some time periods (in kyr) corresponds to significance level greater than 0.8 is also given.

Fig. 2.14.— A) and B) showing late Paleozoic paleogeography of Midland basin and surrounding area during lowstand (A) and highstand (B) times. Sources used: Baldridge 2004; Blakey 1980; Brown 1973; Cleaves 2000; Dickinson and Lawton 2003; Frenzel et al. 1988; Garcia 2005; Heckel 1980; Kues and Giles 2004; Mazzullo 1995; McGookey 2004; Pereira 2005; Poole et al. 2005; Soreghan et al. 2002; Soreghan and Soreghan 2007; Tabor and Montanez 2002; Wermund and Jenkins 1969; Yang and Kominz 1999.

Fig. 2.15.— A) Timing of dust influx with respect to relative sea level in the study interval. For simplification we considered an idealized relative sea level curve. Low=

average dust influx value >1 to <3 times of average minimum value; Moderately high= average dust influx value >3 to <10 times of average minimum value; High= average dust influx value >10 to <1000 times of average minimum value; Maximum= average dust influx value up to 1000 times of average minimum value. HST= Highstand system tract; LST= Lowstand system tract; TS= Transgressive surface; TST= Transgressive system tract. B) Schematic of mudrock and carbonate deposition during various eustatic phases.

References

ALGEO, T.J., AND HECKEL, P.H., 2008, The Late Pennsylvanian Midcontinent Sea of North America: A review: Palaeogeography Palaeoclimatology Palaeoecology, v. 268, p. 205-221.

ANDERSON, R.F., FLEISHER, M.Q., AND LAO, Y., 2006, Glacial-interglacial variability in the delivery of dust to the central equatorial Pacific Ocean: Erath and Planetary Science Letters, v. 242, p. 406-414.

BALDRIDGE, W.S., 2004, Geology of the American Southwest: Cambridge University Press, p. 118-149.

BERGER, A., 1977, Support for the astronomical theory of climate change: Nature, v. 269, p. 44-45.

BERGER, A., LOUTRE, M.F., AND LASKAR, J., 1992, Stability of the astronomical frequencies over the earth's history for paleoclimate studies: Science, v. 255, p. 560-566.

BERGER, A., MÉLICE, J.L., AND HINNOV, L., 1991, A strategy for frequency spectra of Quaternary climate records: Climate Dynamics, v. 5, p. 227-240.

BISHOP, J.W., MONTANEZ, I.P., AND OSLEGER, D.A., in review, Dynamic Carboniferous climate change, Arrow Canyon, Nevada: submitted in Geosphere.

BLAKEY, R.C., 1980, Pennsylvanian and Early Permian Paleogeography, southern Colorado Plateau and vicinity, *in* Fouch, T.D., and Magathan, E.R., eds., Paleozoic paleogeography of West-Central United States. Rocky Mountain Section, Society of Economic Paleontologists and Minerologists, Denver, CO,USA, p. 239-269.

BOARDMAN, D.R., AND HECKEL, P.H., 1989, Glacial-eustatic sea-level curve for Early Late Pennsylvanian sequence in North-Central Texas and biostratigraphic correlation with curve for midcontinent North-America: Geology, v. 17, p. 802-805.

BROWN, L.F.JR., 1973, Cisco depositional systems in North-Central Texas, *in* Brown, L.F., Jr., Cleaves, A.W., II and Erxleben, A.W., eds., Pennsylvanian depositional systems in North-Central Texas, Bureau of Economic Geology, The University of Texas at Austin, Guide Book no. 14, p. 57-122.

CECIL, C.B., 1990, Paleoclimate controls on stratigraphic repetition of chemical and siliciclastic rocks: Geology, v. 18, p. 533-536.

CECIL, C.B., 2004, Eolian dust and the origin of sedimentary chert: U.S. Geological Survey Open-File Report 2004-1098, 15 p.

CECIL, C.B., DULONG, F.T., WEST, R.R., STAMM, R., WARDLAW, B., AND EDGAR, N.T., 2003, Climate controls on the stratigraphy of a Middle Pennsylvanian cyclothem in North America, *in* Cecil, C.B., and Edgar, N.T. eds., Climate Controls on Stratigraphy: SEPM Special Publication, v. 77, p. 151–180.

CENTENO-GARCIA, ELENA., 2005, Review of upper Paleozoic and lower Mesozoic stratigraphy and depositional environments of central and west Mexico; constraints on terrane analysis and paleogeography: Special Paper - Geological Society of America, v. 393, p. 233-258.

CLEAVES, ARTHUR W., 2000, Sequence stratigraphy and reciprocal sedimentation in Middle and Late Pennsylvanian carbonate-bank systems, eastern shelf of the Midland Basin, north-central Texas: Circular - Oklahoma Geological Survey, v.101, p. 227-257.

CONDIE, K.C., AND SELVERSTONE, J., 1999, The crust of the Colorado Plateau: New views of an old arc: Journal of Geology, v. 107, p. 387-397.

CROWELL, J.C., 1999, Pre-Mesozoic ice ages: their bearing on understanding the climate System: Geological Society of America, Memoir, v. 192, 106 p.

DICKINSON, W.R., AND LAWTON, T.F., 2003, Sequential intercontinental suturing as the ultimate control for Pennsylvanian Ancestral Rocky Mountains: Geology, v. 31, p. 609-612.

DICKSON, J.A.D., AND SALLER, A.H., 2006, Carbon isotope excursions and crinoid dissolution at exposure surfaces in carbonates, West Texas, USA: Journal of Sedimentary Research, v. 76, p. 404-410.

FIELDING, C.R., FRANK, T.D., BIRGENHEIER, L.P., RYGEL, M.C., JONES, A.T., AND ROBERTS, J., 2008, Stratigraphic imprint of the Late Palaeozoic Ice Age in eastern Australia: a record of alternating glacial and nonglacial climate regime: Journal of the Geological Society, v. 165, p. 129-140.

FOLK, R.L., 1974, Natural history of crystalline calcium carbonate – effect of magnesium content and salinity: Journal of Sedimentary Petrology, v. 44, p. 40-53.

FRENZEL, H.N., BLOOMER, R.R., CLINE, R.B., CYS, J.M., GALLEY, J.E., GIBSON, W.R., HILLS, J.M., KING, W.E., SEAGER, W.R., KOTTLOWSKI, F.E., THOMPSON, S., LUFF, G.C., PEARSON, B.T., AND SICLEN, D.C.V., 1988, The Permian basin region, *in* Sloss, L. L., ed., Sedimentary cover-North American craton: Boulder, Geological Society of America, The Geology of North America, v. D-2, p. 261–306.

GARCIA, E.C., 2005, Review of upper Paleozoic and lower Messozoic stratigraphy and depositional environments of central and west Mexico: constrants on terrane analysis and Paleogeography, *in* Anderson, T.H., Nourse, J.A., McKee, J.W., and Steimer, M.B., eds., The Mojave-Sonora megashear hypothesis: development, assessment, and alternatives: Geological Society of America, Special Paper, v. 393, p. 233-258.

GIBBS, M.T., 2002, Simulations of Permian climate and comparisons with climate-sensitive sediments: Palaeogeography, Palaeoclimatology, Palaeoecology, v. 110, p. 33-55.

GOLDHAMMER, R.K., 1997, Compaction and decompaction algorithms for sedimentary carbonates: Journal of Sedimentary Research, v. 67, p. 26-35.

GOLDHAMMER, R.K., OSWALD, E.J., AND DUNN, P.A., 1991, Hierarchy of stratigraphic forcing; example from Middle Pennsylvanian shelf carbonates of the Paradox Basin, in Franseen, E.K., Watney, W.L., Kendall, C.G.St.C., and Ross, W., eds., Sedimentary modeling: Computer simulations and methodsfor improved parameter definition: Kansas Geological Survey Bulletin, v. 233, p. 361-413.

GRADSTEIN, F.M., OGG, J.G., SMITH, A.G., BLEEKER, W., AND LOURENS, L.J., 2004, A new geologic time scale, with special reference to Precambrian and Neogene: Episodes, v. 27, p. 83-100.

HECKEL, P.H., 1980, Paleogeography of eustatic model for deposition of mid-continent upper Pennsylvanian cyclothems, *in* Fouch, T.D., and Magathan, E.R., eds., Paleozoic paleogeography of West-Central United States. Rocky Mountain Section: Society of Economic Paleontologists and Minerologists, Denver, CO, USA, p. 197-215.

HECKEL, P.H., 1986, Sea-level curve for Pennsylvanian eustatic marine transgressive-regressive depositional cycles along Midcontinent outcrop belt, North America: Geology, v. 14, p. 330-334.

HONDA, M., YABUKI, S., AND SHIMIZU, H., 2004, Geochemical and isotopic studies of aeolian sediments in China: Sedimentology, v. 51, p. 211–230.

HOUGHTON, J., 2004, Global Warming: The Complete Briefing: Cambridge University Press, Cambridge, 351 p.

ISBELL, J.L., MILLER, M.F., WOLFE, K.L., AND LENAKER, P.A., 2003, Timing of late Paleozoic glaciation in Gondwana: Was glaciation responsible for the development of Northern Hemisphere cyclothems?, *in* Chan, M.A., and Archer, A.W., eds., Extreme depositional environments: Mega end members in geologic time: Geological Society of America Special Paper, v. 370, p. 5-24.

JACOBS, P.M., AND MASON, J.A., 2007, Late Quaternary climate change, loess sedimentation, and soil profile development in the central Great Plains: A pedosedimentary model: Geological Society of America Bulletin, v. 119, p. 462-475.

JICKELLS, T.D., AN, Z.S., ANDERSEN, K. K., BAKER, A. R., BERGAMETTI, G., BROOKS, N., CAO, J. J., BOYD, P. W., DUCE, R. A., HUNTER, K. A., KAWAHATA, H., KUBILAY, N., LAROCHE, J.., LISS, P. S., MAHOWALD, N., PROSPERO, J. M., RIDGWELL, A. J., TEGEN, I., AND TORRES, R., 2005, Global iron connections between desert dust, ocean biogeochemistry, and climate: Science, v. 308, p. 67-71.

JONES, A.T., AND FIELDING, C.R., 2004, Sedimentological record of the late Paleozoic glaciation in Queensland, Australia: Geology, v. 32, p. 153-156.

KESSLER, J.L.P., SOREGHAN, G.S., AND WACKER, H.J., 2001, Equatorial aridity in western Pangea: lower Permian loessite and dolomitic paleosols in northeastern New Mexico, U.S.A.: Journal of Sedimentary Research, v. 71, p. 817-832.

KIESSLING W, FLUGEL E, AND GOLONKA J., 1999, Paleoreef maps: Evaluation of a comprehensive database on Phanerozoic reefs: Americal Association of Petroleum Geologists, Bulletin, v. 83, p. 1552-1587.

KLUTH, C.F., 1986, Plate tectonics of the Ancestral Rocky Mountains, in Peterson, J.A. ed., Paleotectonics and Sedimentation in the Rocky Mountain region: American Association of Petroleum Geologist Memoir, v. 41, p. 353-369.

KUES, B., AND GILES, K., 2004, The Late Paleozoic ancestral Rocky Mountains system in New Mexico, in Mack, G.H., and Giles, K.A., eds., The geology of New Mexico-A geological history: New Mexico Geological Society, special publication, v. 11, p. 95-136.

LOPEZ, R., 1997, The pre-Jurassic geotectonic evolution of the Coahuila terrane, northwestern Mexico: Grenville basement, a late Paleozoic arc, Triassic plutonism, and the events south of the Ouachita suture: PhD. Thesis, Santa Cruz, University of California, p. 55-147.

MAHOWALD, N., KOHFELD, K., HANSSON, M., BALKANSKI, Y., HARRISON, S.P., PRENTICE, I. C., SCHULZ, M., AND RODHE, H., 1999, Dust sources and deposition during the last glacial maximum and current climate: A comparison of model results with paleodata from ice cores and marine sediments: Journal of Geophysical Research, v. 104(D13), p. 15.895-15.916.

MAHOWALD, N.M., MUHS, D., LEVIS, S., RASCH, P., YOSHIOKA, M., AND ZENDER, C., 2006, Change in atmospheric mineral aerosols in response to climate: late glacial period, pre- industrial, modern and doubled-carbon dioxide climates: Journal of Geophysical Research, v. 111, D10202.

MARINO, F., MAGGI, V., DELMONTE, B., GHERMANDI, G., AND PETIT, J.R., 2005, Elemental composition (Si, Fe, Ti) of atmospheric dust over the last 220 kyr from the EPICA ice core (Dome C, Antarctica): Annals of Glaciology, v. 39, p. 110-118.

MAZZULO, S.J., 1995, Permian stratigraphy and facies, Permian basin (Texas-New Mexico) and adjoining areas in the Midcontinent United States, *in* Scholle, T.M., Peryt, T.M., and Scholle, U., eds., The Permian of Northern Pangea: Sedimentary basins and economic resources. Springer-Verlag, v. 2, p. 41-60.

MCGOOKEY, D.P., 2004, Geologic wonders of West Texas, Published by Donald P. McGookey, p. 51-64.

MCLENNAN, S.M., FRYER, B.J., FRYER, B.J., AND YOUNG, G.M., 1979, Geochemistry of the carbonate-rich Espanola Formation (Huronian) with emphasison the rare-earth elements: Canadian Journal of Earth Sciences, v. 16, p. 230-239.

MCLENNAN, S. M., HEMMING, S., MCDANIEL, D. K. AND HANSON, G. N., 1993, Geochemical approaches to sedimentation, provenance and tectonics, *in* Johnsson, M. J., and Basu, A., eds., Processes controlling the composition of clastic sediments: Geological Society of America Special Paper, v. 284, p. 21-40.

MILLER, K.B., MCCAHON, T.J., AND WEST, R.R., 1996, Lower Permian (Wolfcampian) paleosol-bearing cycles of the US midcontinent: Evidence of climatic cyclicity: Journal of Sedimentary Research, v. 66, p. 71-84.

MUHS, D.R., AND BETTIS, E.A., III, 2000, Geochemical Variations in Peoria Loess of Western Iowa Indicate Paleowinds of Midcontinental North America during Last Glaciation: Quaternary Research, v. 53, p. 49-61.

MUHS, D.R., AND BETTIS, E.A., III, 2003, Quaternary loess-paleosol sequences as an example of climate extremes: Geological Society of America Special Publication, v. 370, p. 53-74.

MUHS, D.R., BUDAHN, J.R., PROSPERO, J.M., AND CAREY, S.N., 2007, Geochemical evidence for African dust inputs to soils of western Atlantic islands: Barbados, the Bahamas, and Florida: Journal of Geophysical Research- Earth Surface, v. 112, issue F2, F02009.

MYERS, D. A., STAFFORD, P. T., AND BURNSIDE, R. J., 1956, Geology of the Late Paleozoic Horseshoe Atoll in West Texas: University of Texas Publication, v. 5607, p. 1-113.

NESBITT, H.W., AND YOUNG, G.M., 1982, Early Proterozoic climates and plate motions inferred from major element chemistry of lutites: Nature, v. 299, p. 715-717.

NICKLEN, B.L., BELL, G.L. JR., AND HUFF, W.D., 2007, Ancient ash beds in the type area of the Middle Permian, Guadalupe Mountains National Park, West Texas, USA: Abstracts with Programs - Geological Society of America, v. 39, p. 148

OLSZEWSKI, T.D., AND PATZKOWSKY, M.E., 2003, From cyclothems to sequences: the record of eustasy and climate on an icehouse epeiric platform (Pennsylvanian-Permian, North American Midcontinent): Journal of Sedimentary Research, v. 73, p. 15-30.

PARRISH, J.T., 1982, Upwelling and petroleum source beds, with reference to the Paleozoic: American Association of Petroleum Geologists, Bulletin, v. 66, p. 750-774.

PARRISH, J.T., 1993, Climate of the supercontinent Pangea: Journal of Geology, v.101, p. 215-233.

PAILLARD, D., LABEYRIE, L., AND YIOU, P., 1996, Macintosh program performs time-series analysis: Eos Trans. AGU, v. 77, p. 379.

PEREIRA, S., 2005, Variation in detrital flux records in upper Pennsylvanian mounds of Horseshoe atoll, Texas. Masters Thesis. University of Oklahoma, Norman, Oklahoma, 72 p.

PETIT, J.R., JOUZEL, J., RAYNAUD, D., BARKOV, N.I., BARNOLA, J.M., BASILE, I., BENDER, M., CHAPELLAZ, J., DAVIS, M., DELAYGUE, G., DELMOTTE, M., KOTLYAKOV, V.M., LEGRAND, M., LIPENDOV, V.Y., LORIUS, C., PEPIN, L., RITZ, C., SALTZMANN, E., AND STIEVENARD, M., 1999, Climate and atmospheric history of the past 420,000 years from the Vostok ice core, Antarctica: Nature, v. 399, p. 429–436.

POOLE, F.G., PERRY, W.J.JR, MADRID, R.J., AND MARTINEZ, R.A., 2005, in Scholle, T.M., Peryt, T.M., and Scholle, U., eds., The Permian of Northern Pangea, Sedimentary basins and economic resources (vol 2), Springer-Verlag, p. 41-60.

PORTER, S.C., AND AN, Z., 1995, Correlation between climate events in the North Atlantic and China during the last glaciation: Nature, v. 375, p. 305-308.

POTTER, P.E., MAYNARD, J.B., AND DEPETRIS, P.J., 2005, Mud and Mudstones: introduction and overview: Springer-Verlag, 297 p.

RANKEY, E.C., 1997, Relations between relative changes in sea level and climate shifts: Pennsylvanian–Permian mixed carbonate-siliciclastic strata, western United States: Geological Society of America, Bulletin, v. 109, p. 1089-1100.

RASBURY, E.T., HANSON, G. N., MEYERS, W. J., HOLT, W. E., GOLDSTEIN, R. H., AND SALLER, A. H., 1998, U-Pb dates of paleosols: Constraints on late Paleozoic cycle durations and boundary ages: Geology, v. 26, p. 403-406.

RAZA, M., CASSHYAP, S.M., AND KHAN, A., 2002, Geochemistry of Mesoproterozoic Lower Vindhyan shales from Chittaurgarh, southeastern Rajasthan and its bearing on source rock composition, palaeoweathering conditions and tectono-sedimentary environments: Journal of the Geological Society of India, v. 60, p. 505-518.

REA, D.K., 1994, The paleoclimatic record provided by eolian deposition in the deep sea: the geologic history of wind: Reviews of Geophysics, v. 32, p. 159-195.

REA, D.K., AND JANECEK, T.R., 1981, Late Cretaceous history of eolian deposition in the mid-Pacific mountains, central North Pacific Ocean: Palaeogeography, Palaeoclimatology, Palaeoecology, v. 36, p. 55-67.

REA, D.K., SNOECKX, H., AND JOSEPH, L.H., 1998, Late Cenozoic eolian deposition in the North Pacific; Asian drying, Tibetan uplift, and cooling of the Northern Hemisphere: Paleoceanography, v. 13, p. 215-224.

READ, J.F., 1995, Overview of carbonate platform sequences, cycle stratigraphy and reservoirs in greenhouse and icehouse worlds, in Read, J.F., Kerans, C., Weber, L.J., Sarg, J.F., and Wright, F.W., eds., Milankovitch sea level changes, cycles and reservoirs on carbonate platforms in greenhouse and icehouse worlds, SEPM short course notes 35, p. 1-102.

REID, A AND REID, S.T., 1990, Glacio-eustatic sea level fluctuations and the formation of Pennsylvanian age carbonate reservoirs in the Permian Basin of west Texas, *in* Grace, D.T., and Hinterlong, G.D., eds., The Permian Basin: Providing energy for America: West Texas Geological Society Publication, 99-106, p. 71-79.

SALLER, A.H., 1999, Core description and sedimentology of Upper Pennsylvanian and lowest Permian limestones and dolomite, South Dome of Reinecke Field, west Texas, Unpublished internal report, Unocal Corporation.

SALLER, A.H., DICKSON, J.A.D., AND BOYD, S.A., 1994, Cycle stratigraphy and porosity in Pennsylvanian and lower Permian shelf limestones, Eastern Central basin platform, Texas: American Association of Petroleum Geologists, Bulletin, v. 78, p. 1820-1842.

SALLER, A.H., DICKSON, J.A.D., AND MATSUDA, F., 1999a, Evolution and distribution of porosity associated with subaerial exposure in Upper Paleozoic platform limestones, West Texas: American Association of Petroleum Geologists, Bulletin, v. 83, p. 1835-1854.

SALLER, A.H., DICKSON, J.A.D., RASBURY, E.T., AND EBATO, T., 1999b, Effects of long-term accommodation change on short-term cycles, upper Paleozoic platform limestones, west Texas, in Harris, P.M., Saller, A.H., Simo, J.A., eds, Advances in Carbonate Sequence Stratigraphy: Application to Reservoirs, Outcrops, and Models: SEPM Special Publication, v. 63, p. 227-246.

SALLER, A.H., WALDEN, S., ROBERTSON, S., STECKEL, M., SCHWAB, J., HAGIWARA, H., AND MIZOHATA, S., 1999c, Reservoir characterization of a reefal carbonate for crestal CO_2 flood, Reinecke Field, west Texas, in Hentz, T.F., ed, Advanced Reservoir Characterization for the 21st Century: Gulf Coast Section SEPM Foundation 19th Annual Research Conference, p. 259-268.

SALLER, A.H., WALDEN, S., ROBERTSON, S., STECKEL, M., SCHWAB, J., HAGIWARA, H., AND MIZOHATA, S., 2004, Three-dimensional seismic imaging and reservoir modeling of an upper Paleozoic "reefal" buildup, Reinecke Field, west Texas, United States, *in* Seismic imaging of carbonate reservoirs and systems: American Association of Petroleum Geologists Memoir, 81, p. 107-122.

SCHATZINGER, R.A., 1988, Depositional environments and diagenesis of the eastern portion of the Horseshoe Atoll, west Texas: Dissertation Abstracts International B Sciences and Engineering, v. 48, p. 3230.

SCHIEBER, J., 1992, A combined petrographic geochemical provenance study of the Newland Formation, mid-Proterozoic of Montana: Geological Magazine, v. 129, p. 223-237.

SCOTESE, C.R., 2001, Atlas of Earth History, Volume 1 (Paleogeography): PALEOMAP Project, Arlington, Texas.

SOREGHAN, G.S., 1994a, The impact of glacioclimatic change on Pennsylvanian cyclostratigraphy, in Embry, A.F., Beauchamp, B., and Glass, D.J., eds., Pangea: Global environments and resources: Canadian Society of Petroleoum Geologists Memoir, v. 17, p. 523-543.

SOREGHAN, G.S., 1994b, Stratigraphic responses to geologic processes: Late Pennsylvanian eustasy and tectonics in the Pedregosa and Orogrande basin, Ancestral Rocky Mountains: Geological Society of America, Bulletin, v. 106, p. 1195-1211.

SOREGHAN, G.S., AND DICKINSON, W.R., 1994, Generic types of stratigraphic cycles controlled by eustasy: Geology, v. 22, p. 759-761.

SOREGHAN, G.S., ELMORE, R.D., AND LEWCHUK, M.T., 2002, Sedimentologic-magnetic record of western Pangean climate in upper Paleozoic loessite (lower Cutler beds, Utah): Geological Society of America, Bulletin, v. 114, p. 1019-1035.

SOREGHAN, G.S., AND GILES, K.A., 1999, Amplitudes of late Pennsylvanian glacioeustasy: Geology, v. 27, p. 255-258.

SOREGHAN, G.S., MOSES, A.M., SOREGHAN, M.J., HAMILTON, M.A., FANNING, C.M., AND LINK, P.K., 2007, Palaeoclimatic inferences from upper Palaeozoic siltstone of the Earp Formation and equivalents, Arizona-New Mexico (USA): Sedimentology, v. 54, p. 701-719.

SOREGHAN, G.S., AND SOREGHAN, M.J., 2002, Atmospheric dust and algal dominance in the late Paleozoic: A hypothesis: Journal of Sedimentary Research, v. 72, p. 457-461.

SOREGHAN, G.S., SOREGHAN, M.J., AND HAMILTON, M.A., 2008a, Origin and significance of loess in late Paleozoic western Pangaea: A record of tropical cold?: Palaeogeography, Palaeoclimatology, Palaeoecology, v. 268, p. 234-259.

SOREGHAN, G.S., SOREGHAN, M.J., POULSEN, C.J., YOUNG, R.A., EBLE, C.F., SWEET, D.E., AND DAVOGUSTTO, O.C., 2008b, Anomalous cold in the Pangaean tropics: Geology, v. 36, p. 659-662.

SOREGHAN, M.J., AND SOREGHAN, G.S., 2007, Whole rock geochemistry of upper Paleozoic loessites, western Pangaea: Implications for paleo-atmosphere circulation: Earth and Planetary Science Letters, v. 255, p. 117-132.

SOREGHAN, M.J., SOREGHAN, G.S., AND HAMILTON, M.A., 2002, Paleowinds inferred from detrital zircon geochronology of upper Paleozoic loessite, western equatorial Pangea: Geology, v. 30, p. 695-698.

SOREGHAN, M.J., SOREGHAN, G.S., AND HAMILTON, M.A., 2008, Glacial-interglacial shifts in atmospheric circulation of western tropical Pangaea: Palaeogeography, Palaeoclimatology, Palaeoecology, v. 268, p. 260-272.

STAFFORD, P.T., 1959, Pennsylvanian and lower Permian rocks of parts of west and central Texas, *in* Myers, D.A., Stafford, P.T., and Burnside, R.J., eds., Geology of part of the Horseshoe Atoll in Scurry and Kent Counties, Texas: University of Texas, Bureau of Economic Geology, Report: 5607, 113 p.

STEVENS, T., ARMITAGE, S.J., LU, H., AND THOMAS, D.S.G., 2006, Sedimentation and diagenesis of Chinese loess: Implications for the preservation of continuous, high-resolution climate records: Geology, v. 34, p. 849-852.

SUR, S., SOREGHAN, G.S., SOREGHAN, M.J., AND LYONS, T.W., in review a, Glacial-stage eolian delivery of highly reactive iron to late Paleozoic oceans: submitted in Geology.

SUR, S., SOREGHAN, G.S., SOREGHAN, M.J., AND STAGNER, A.F., in review b, Extraction methodology for the silicate mineral fraction (eolian dust) from ancient carbonate: assessing the geologic record of dust: submitted in Journal of Sedimentary Research.

TABOR, N.J., AND MONTANEZ, I.P., 2002, Shifts in late Paleozoic atmospheric circulation over western equatorial Pangea: Insights from pedogenic mineral $\delta^{18}O$ compositions: Geology, v. 30, p. 1127-1130.

TAYLOR, S. R., AND MCLENNAN, S. M., 1985, The Continental Crust: Its Composition and Evolution. Blackwell (Oxford), 312 p.

THOMSON, D. J., 1982, Spectrum estimation and harmonic analysis: Proceedings of IEEE, v. 70, p. 1055-1096.

TOTTEN, M.W., HANAN, M.A., AND WEAVER, B.L., 2000, Beyond whole-rock geochemistry of shales: The importance of assessing mineralogic controls for revealing tectonic discriminants of multiple sediment sources for the Ouachita Mountain flysch deposits: Geological Society of America Bulletin, v. 112, p. 1012-1022.

TRAMP, K.L., SOREGHAN, G.S., AND ELMORE, R.D., 2004, Paleoclimatic inferences from paleopedology and magnetism of the Permian Maroon Formation loessite, Colorado, USA: Geological Society of America Bulletin, v. 116, p. 671-686.

VEEVERS, J.J., AND POWELL, C.M., 1987, Late Paleozoic glacial episodes in Gondwanaland reflected in transgressive-regressive depositional sequences in Euramerica: Geological Society of America Bulletin, v. 98, p. 475-487.

VEST, E.L.JR., 1970, Oil fields of Pennsylvanian-Permian Horseshoe atoll, West Texas, *in* Halbouty, M.T., ed., Geology of giant petroleum fields: American Association of Petroleum Geologists Memoir, v. 14, p. 185-203.

WAITE, L.E., 1993, Upper Pennsylvanian seismic sequences and facies of the eastern and southern Horseshoe Atoll, Midland Basin, West Texas, *in* Loucks, R.G., and Sarg, J.F., eds., Carbonate sequence stratigraphy: recent developments and advancements: American Association of Petroleum Geologists Memoir, v. 57, p. 213-240.

WALKER, D.A., GOLONKA, J., REID, A., AND REID, S., 1995, The effects of Paleolatitude and Paleogeography on late Paleozoic carbonate sedimentation in west Texas; part II: Permian: West Texas Geological Society Bulletin, v. 34, p. 5-14.

WANLESS, H. R., AND SHEPARD, J. P., 1936, Sea level and climatic changes related to late Paleozoic cycles: Geological Society of America Bulletin, v. 47, p. 1177-1206.

WERMUND, E.G., AND JENKINS, W.A.JR., 1969, Late Pennsylvanian series in North-Central Texas, *in* Brown, L.F.Jr., and Wermund, E.G., eds., Late Pennsylvanian shelf sediments North-Central Texas: Published by Dallas Geological Society, p.1-20.

WILDE, G.L., 1990, Practical fusulinid zonation: The species concept; with Permian basin emphasis: West Texas Geological Society Bulletin, v. 29, p. 5-34.

YANCEY, T.E., AND MCLERRAN, R.D., 1988, Cyclic stratigraphy of the Late Pennsylvanian of north-central Texas, in Cunningham, B.K.., ed., Permian and Pennsylvanian stratigraphy, Midland Basin, west Texas: Studies to aid hydrocarbon exploration: Society of Economic Paleontologists and Mineralogists, Permian Basin Section Seminar No. 1, p. 65-77.

YANG, W., HARMSEN, F., KOMINZ, M.A., 1995, Quantitative analysis of cyclic peritidal carbonate sequence, the Middle and Upper Devonian Lost Burro Formation, Death Valley, California; a possible record of Milankovitch climatic cycles: Journal of Sedimentary Research, v. 65B, p. 306-322.

YANG, W., AND KOMINZ, M.A., 1999, Testing periodicity of depositional cyclicity Cisco Group (Virgilian and Wolfcampian), Texas: Journal of Sedimentary Research, v. 69, p. 1209-1231.

YANG, W., KOMINZ, M.A., AND MAJOR, R.P., 1998, Distinguishing the roles of autogenic versus allogenic processes in cyclic sedimentation, Cisco Group (Virgilian and Wolfcampian), north-central Texas: Geological Society of America Bulletin, v. 110, p. 1333-1353.

YANG, WAN, AND LEHRMANN, D. J., 2003, Milankovitch climatic signals in Lower Triassic (Olenekian) Peritidal carbonate successions, Nanpanjiang Basin, south China: Palaeogeography, Palaeoclimatology, Palaeoecology, v. 201, p. 283-306.

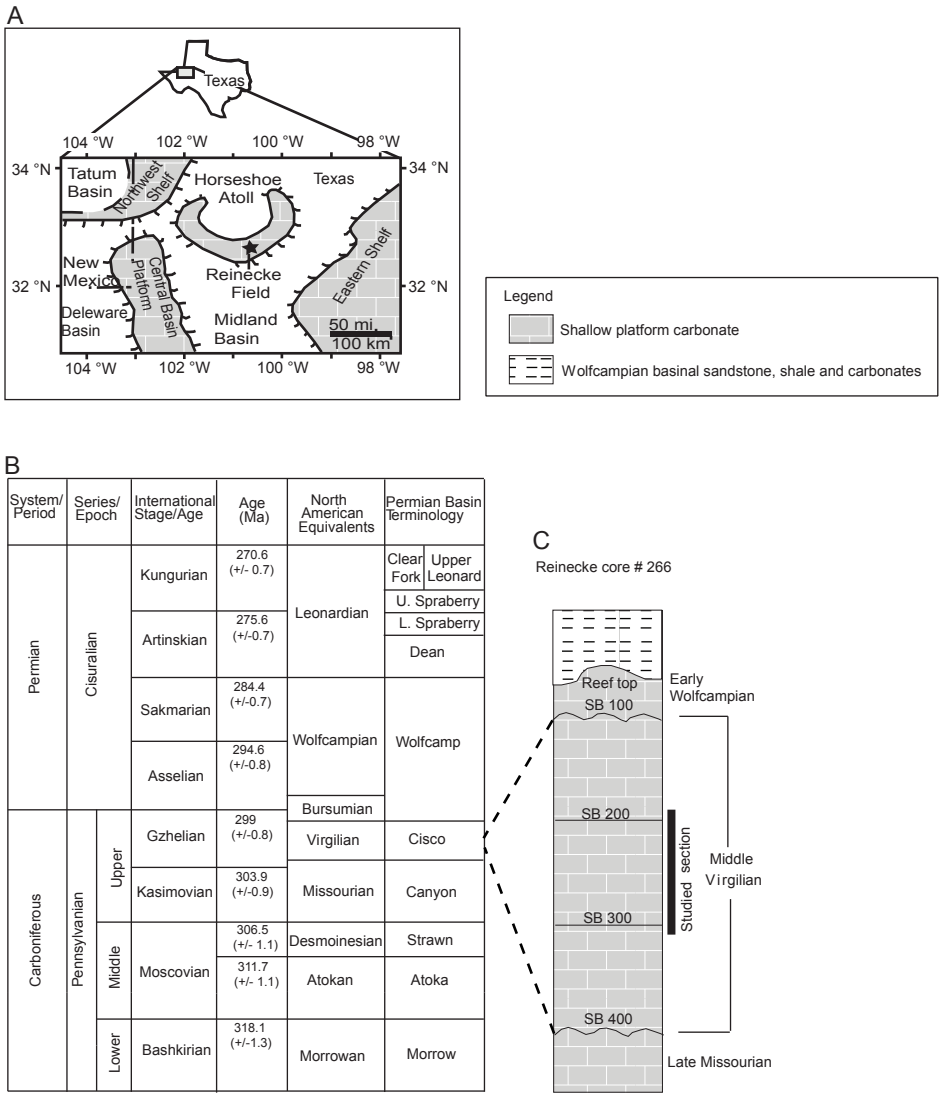
A
Texas
104 °W
102 °W
100 °W
98 °W
34 °N
32 °N
Tatum Basin
Northwest Shelf
Horseshoe Atoll
Texas
New Mexico
Central Basin Platform
Reinecke Field
Eastern Shelf
Deleware Basin
Midland Basin
50 mi.
100 km
Legend
Shallow platform carbonate
Wolfcampian basinal sandstone, shale and carbonates
B
System/ Period
Series/ Epoch
International Stage/Age
Age (Ma)
North American Equivalents
Permian Basin Terminology
Permian
Cisuralian
Kungurian
270.6 (+/- 0.7)
Leonardian
Clear Fork
Upper Leonard
U. Spraberry
L. Spraberry
Artinskian
275.6 (+/-0.7)
Dean
Sakmarian
284.4 (+/-0.7)
Wolfcampian
Wolfcamp
Asselian
294.6 (+/-0.8)
Bursumian
Carboniferous
Pennsylvanian
Upper
Gzhelian
299 (+/-0.8)
Virgilian
Cisco
Kasimovian
303.9 (+/-0.9)
Missourian
Canyon
Middle
Moscovian
306.5 (+/- 1.1)
Desmoinesian
Strawn
311.7 (+/- 1.1)
Atokan
Atoka
Lower
Bashkirian
318.1 (+/-1.3)
Morrowan
Morrow
C
Reinecke core # 266
Reef top
SB 100
SB 200
SB 300
SB 400
Studied section
Early Wolfcampian
Middle Virgilian
Late Missourian

Figure 2.1

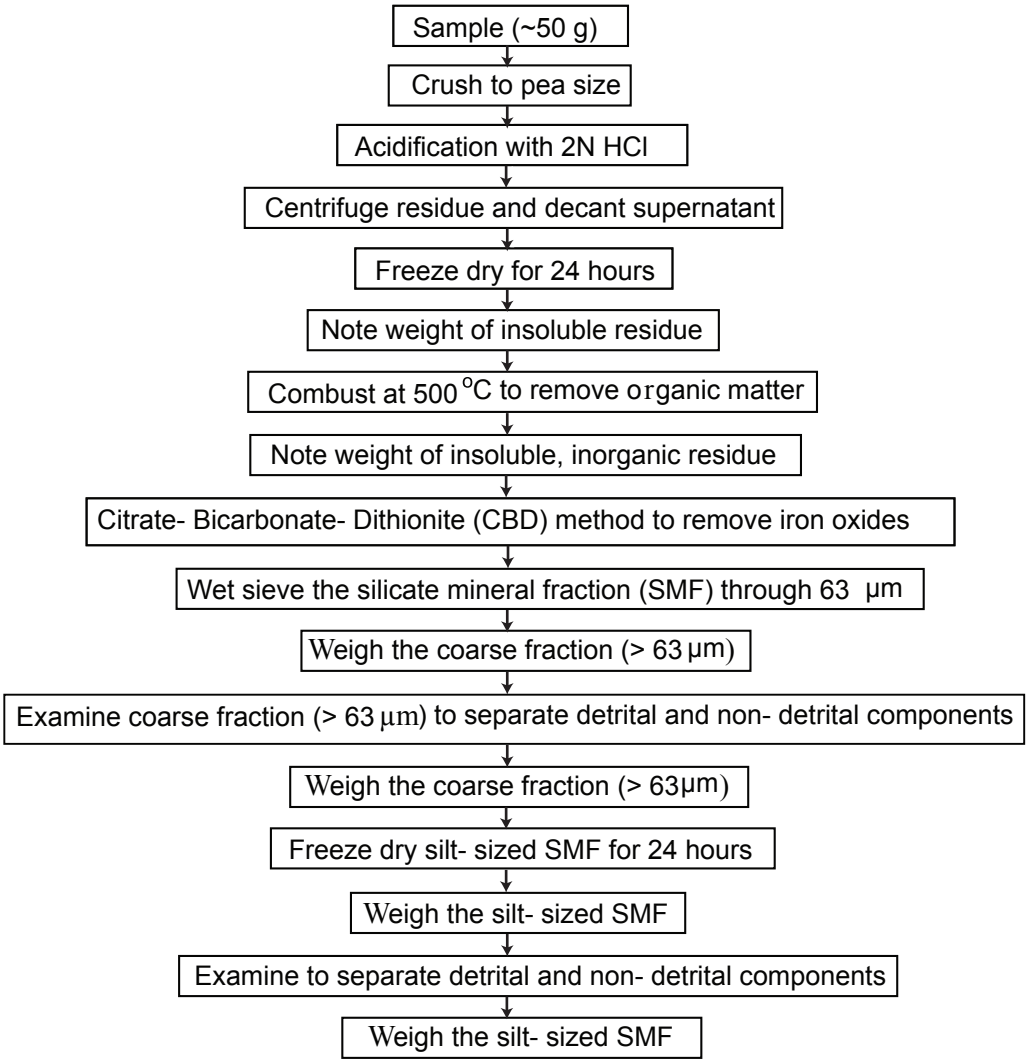
Sample (~50 g)
Crush to pea size
Acidification with 2N HCl
Centrifuge residue and decant supernatant
Freeze dry for 24 hours
Note weight of insoluble residue
Combust at 500 °C to remove organic matter
Note weight of insoluble, inorganic residue
Citrate- Bicarbonate- Dithionite (CBD) method to remove iron oxides
Wet sieve the silicate mineral fraction (SMF) through 63 µm
Weigh the coarse fraction (> 63 µm)
Examine coarse fraction (> 63 µm) to separate detrital and non- detrital components
Weigh the coarse fraction (> 63µm)
Freeze dry silt- sized SMF for 24 hours
Weigh the silt- sized SMF
Examine to separate detrital and non- detrital components
Weigh the silt- sized SMF

Figure 2.2

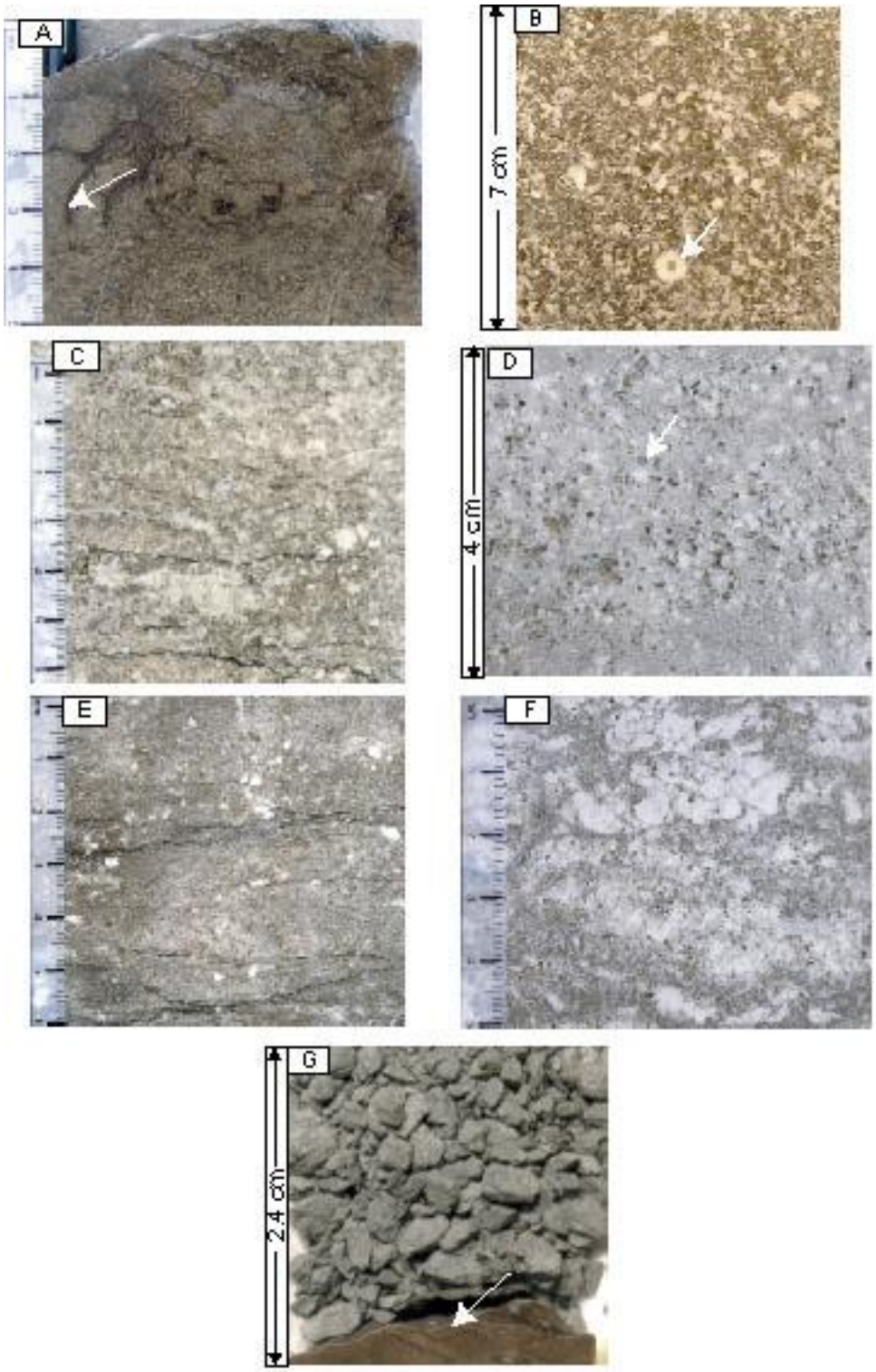

Figure 2.3

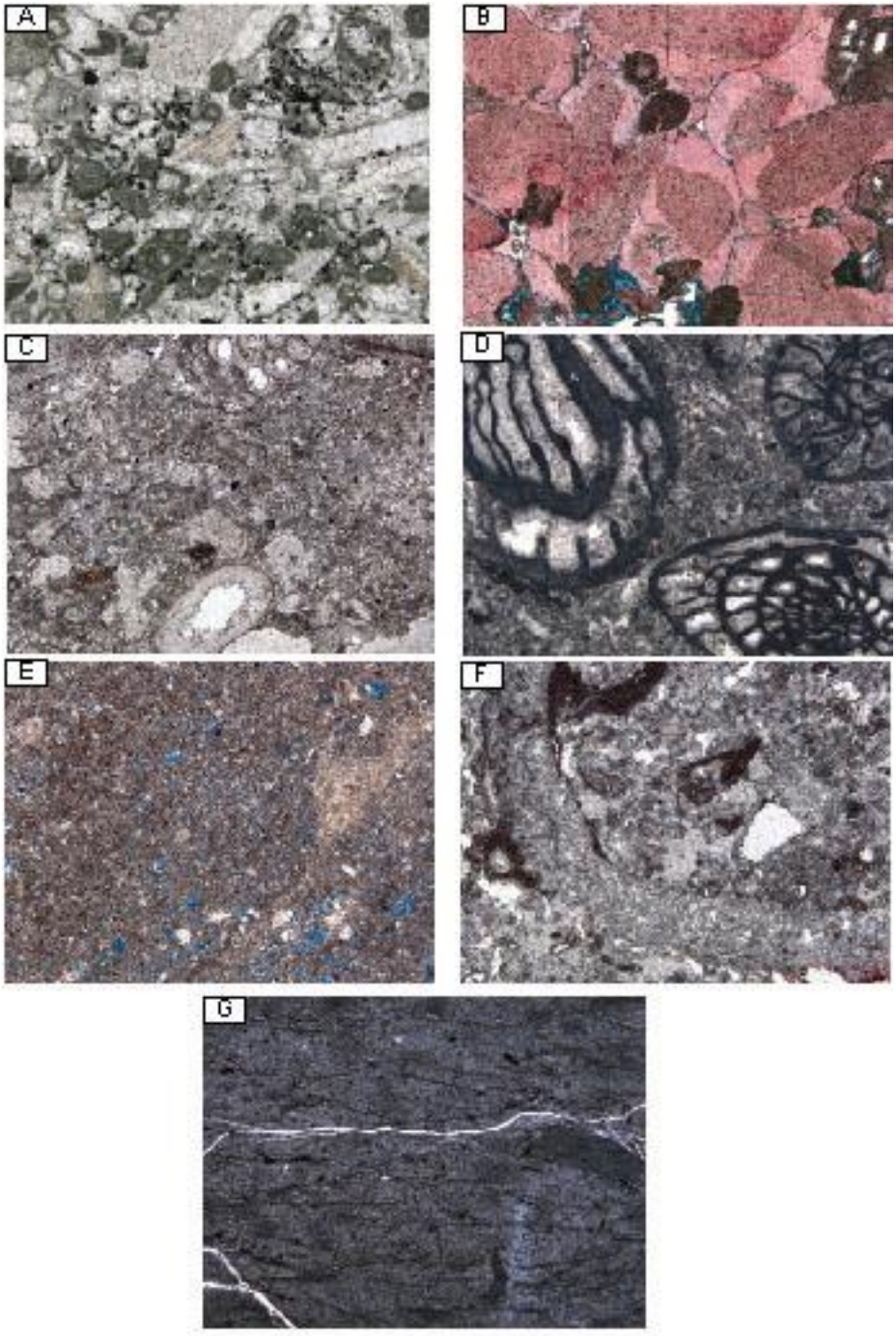

Figure 2.4

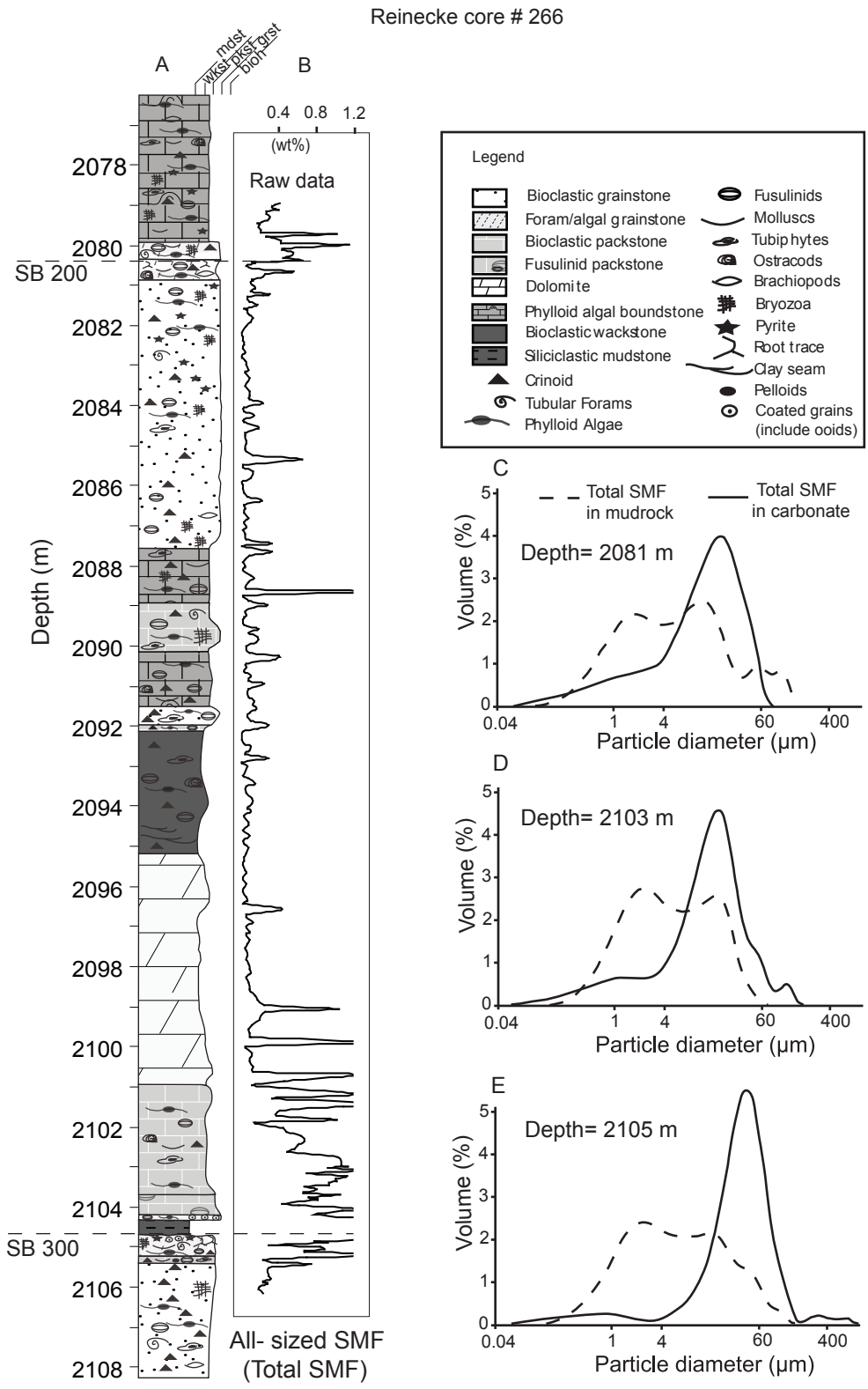
Reinecke core # 266
A
B
mdst
wkst
pkst
grst
dlom
0.4 0.8 1.2
(wt%)
Raw data
2078
2080
SB 200
2082
2084
2086
2088
2090
2092
2094
2096
2098
2100
2102
2104
SB 300
2106
2108
Depth (m)
All- sized SMF
(Total SMF)
Legend
Bioclastic grainstone
Foram/algal grainstone
Bioclastic packstone
Fusulinid packstone
Dolomite
Phylloid algal boundstone
Bioclastic wackstone
Siliciclastic mudstone
Crinoid
Tubular Forams
Phylloid Algae
Fusulinids
Molluscs
Tubiphytes
Ostracods
Brachiopods
Bryozoa
Pyrite
Root trace
Clay seam
Pelloids
Coated grains
(include ooids)
C
Total SMF
in mudrock
Total SMF
in carbonate
Depth= 2081 m
Volume (%)
Particle diameter (μm)
0.04
1
4
60
400
D
Depth= 2103 m
E
Depth= 2105 m

Figure 2.5

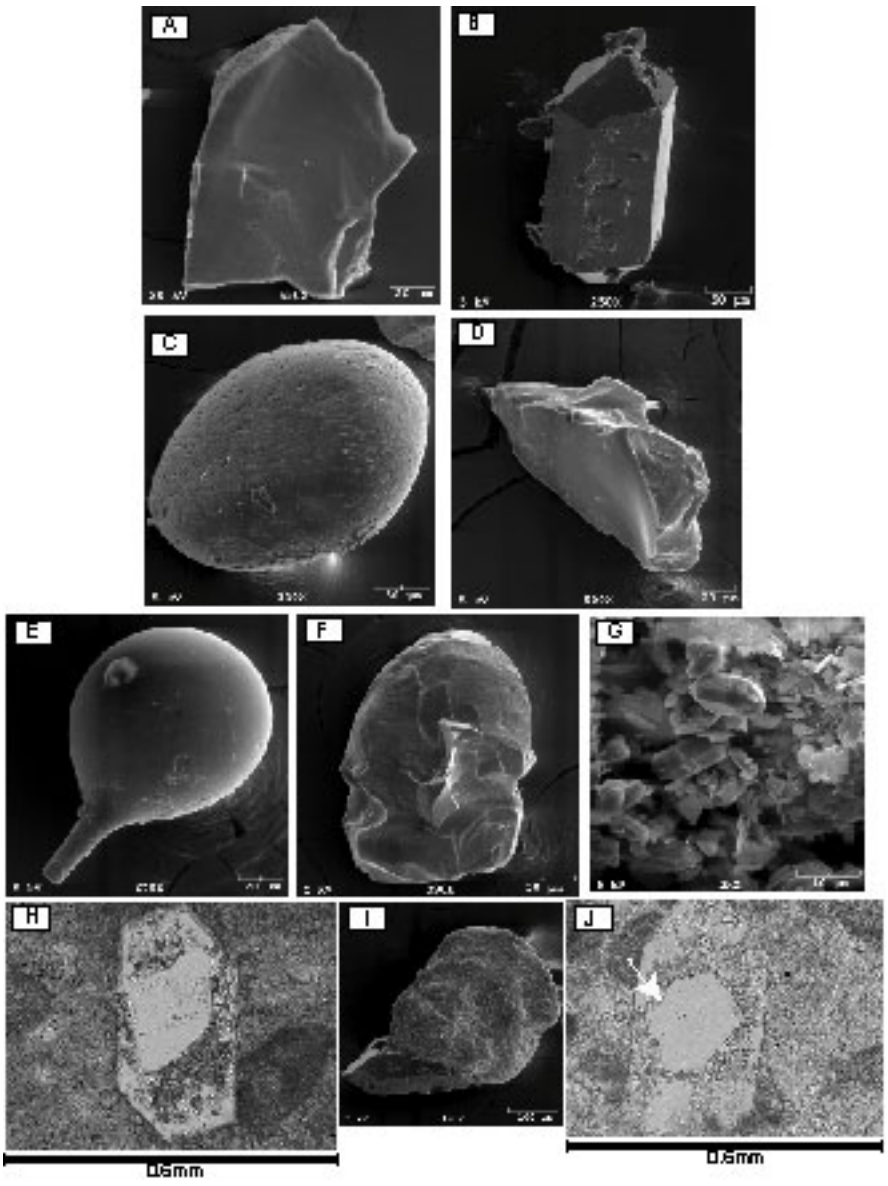

Figure 2.6

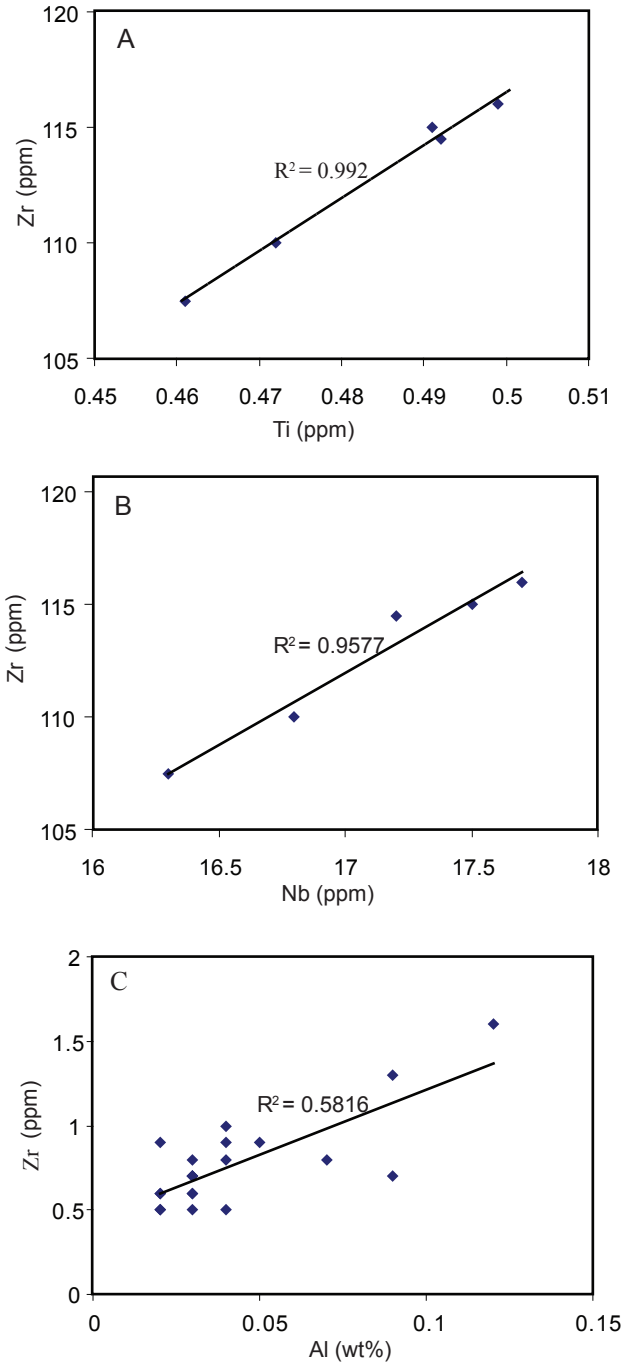
A
R² = 0.992
Zr (ppm)
Ti (ppm)
120
115
110
105
0.45
0.46
0.47
0.48
0.49
0.5
0.51
B
R² = 0.9577
Zr (ppm)
Nb (ppm)
120
115
110
105
16
16.5
17
17.5
18
C
R² = 0.5816
Zr (ppm)
Al (wt%)
2
1.5
1
0.5
0
0
0.05
0.1
0.15

Figure 2.7

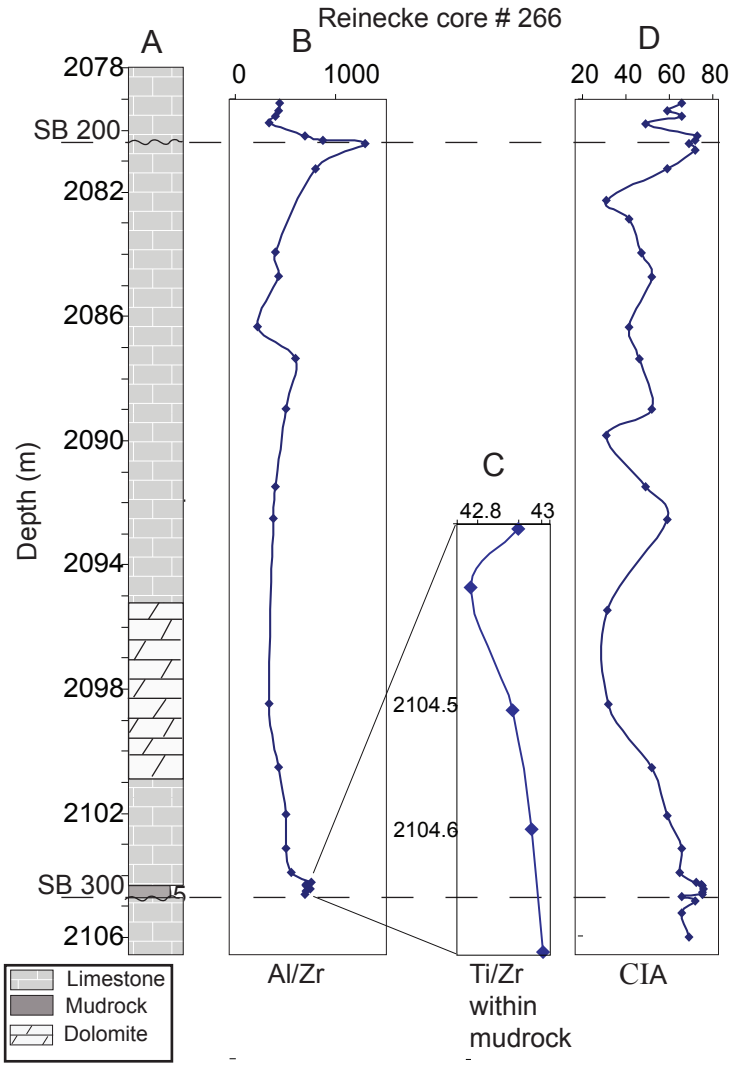
Reinecke core # 266
A
B
C
D
2078
SB 200
2082
2086
2090
2094
2098
2102
SB 300
2106
Depth (m)
0
1000
42.8
43
2104.5
2104.6
20
40
60
80
Limestone
Mudrock
Dolomite
Al/Zr
Ti/Zr
within
mudrock
CIA

Figure 2.8

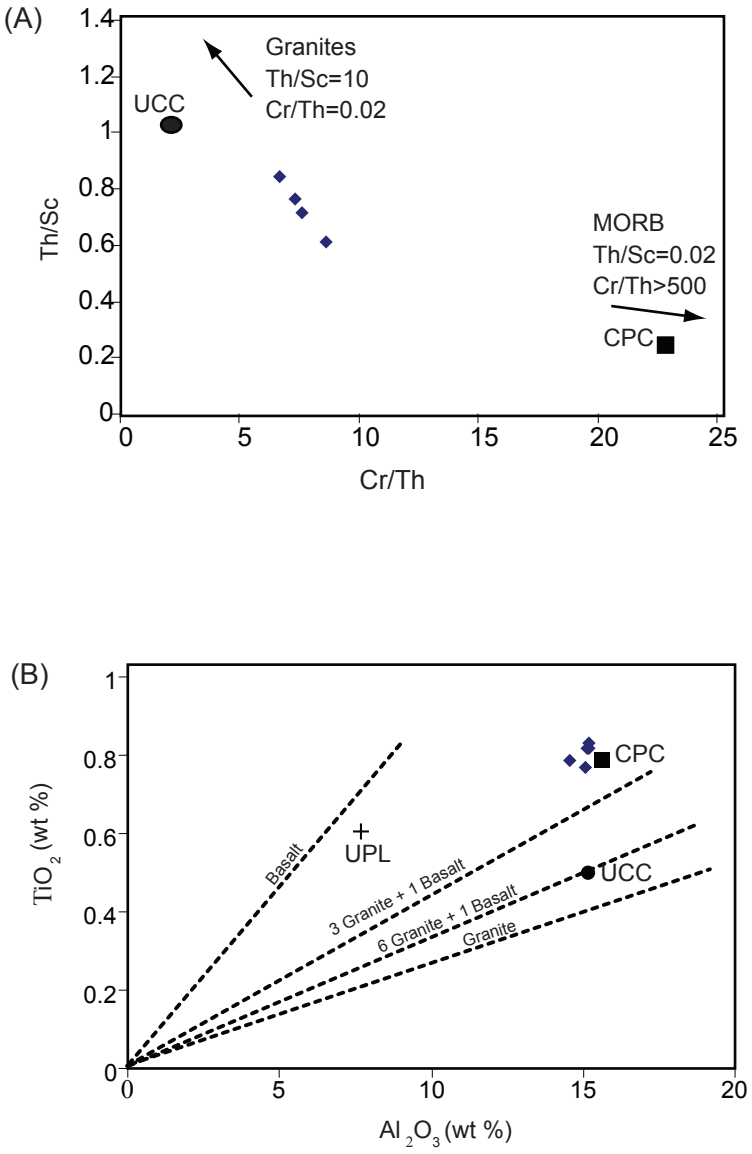
(A)
Granites
Th/Sc=10
Cr/Th=0.02
UCC
MORB
Th/Sc=0.02
Cr/Th>500
CPC
Th/Sc
Cr/Th
(B)
CPC
UPL
UCC
Basalt
3 Granite + 1 Basalt
6 Granite + 1 Basalt
Granite
TiO2 (wt %)
Al2O3 (wt %)

Figure 2.9

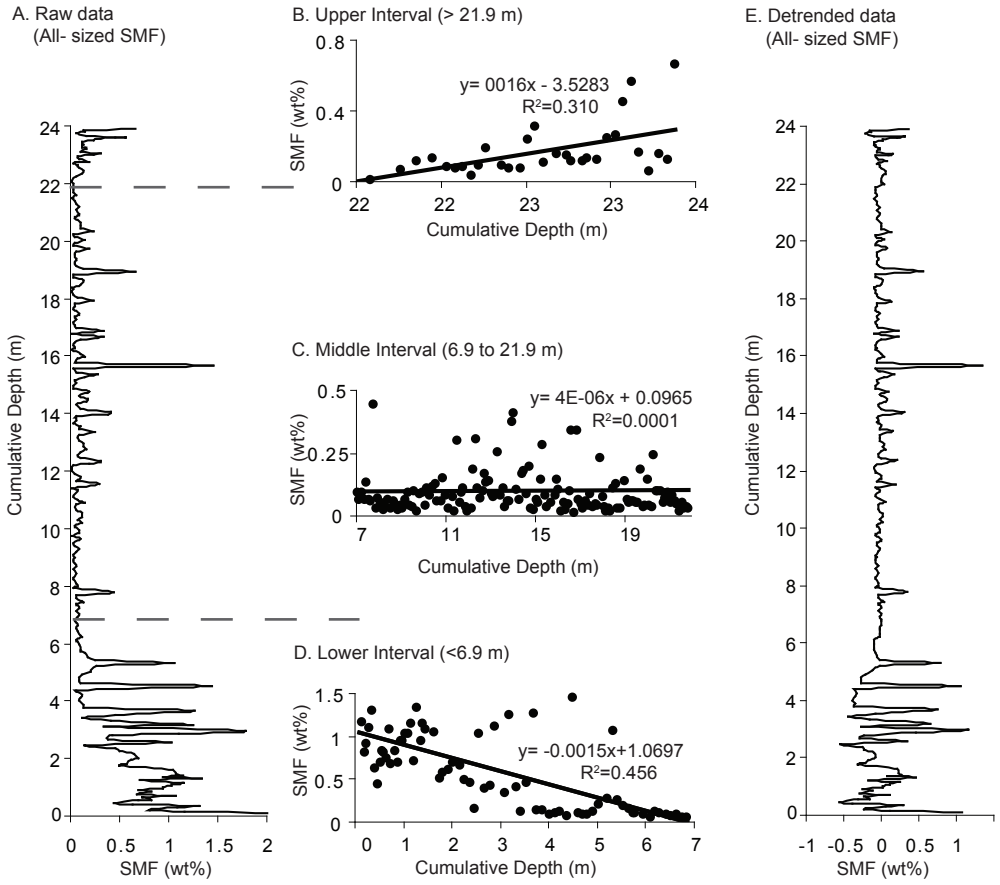
A. Raw data
(All- sized SMF)
Cumulative Depth (m)
SMF (wt%)
B. Upper Interval (> 21.9 m)
y= 0016x - 3.5283
R²=0.310
SMF (wt%)
Cumulative Depth (m)
C. Middle Interval (6.9 to 21.9 m)
y= 4E-06x + 0.0965
R²=0.0001
SMF (wt%)
Cumulative Depth (m)
D. Lower Interval (<6.9 m)
y= -0.0015x+1.0697
R²=0.456
SMF (wt%)
Cumulative Depth (m)
E. Detrended data
(All- sized SMF)
Cumulative Depth (m)
SMF (wt%)

Figure 2.10

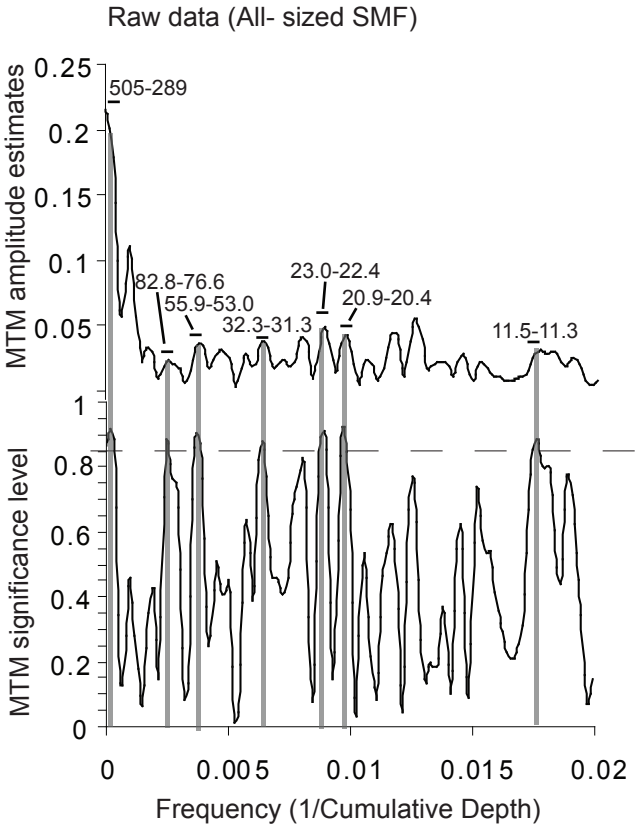
Raw data (All- sized SMF)
MTM amplitude estimates
0.25
0.2
0.15
0.1
0.05
505-289
82.8-76.6
55.9-53.0
32.3-31.3
23.0-22.4
20.9-20.4
11.5-11.3
1
0.8
0.6
0.4
0.2
0
MTM significance level
0
0.005
0.01
0.015
0.02
Frequency (1/Cumulative Depth)

Figure 211

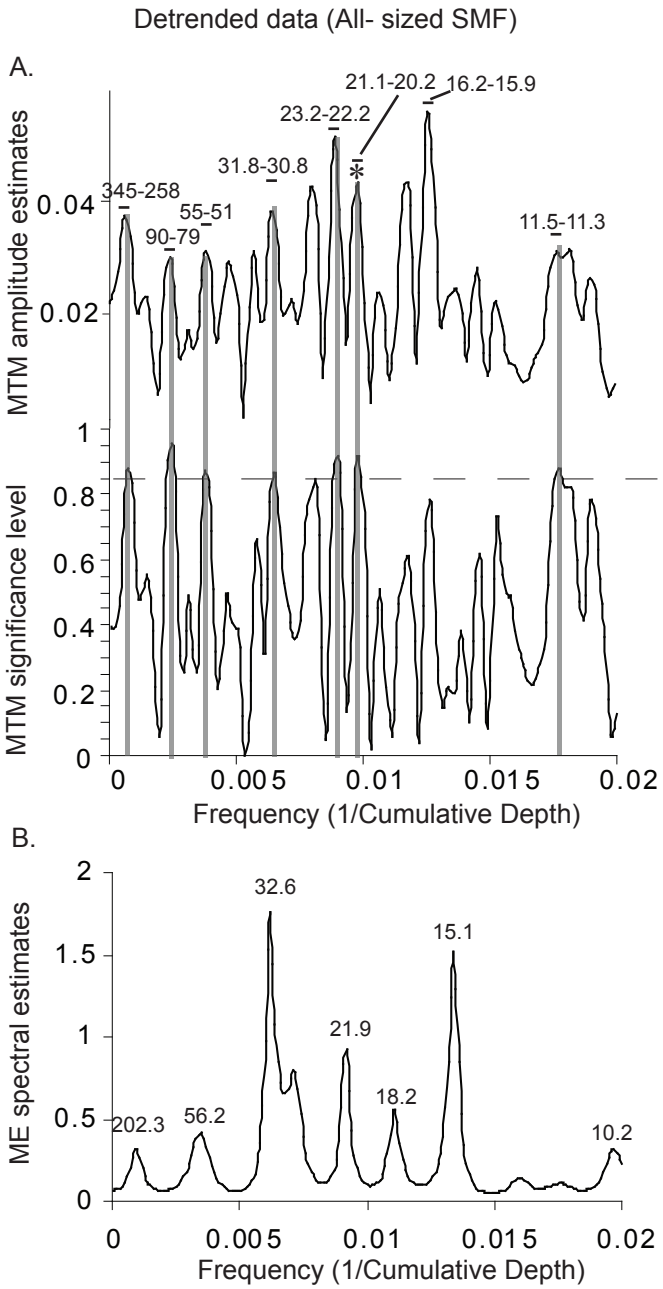
Detrended data (All- sized SMF)
A.
MTM amplitude estimates
MTM significance level
345-258
90-79
55-51
31.8-30.8
23.2-22.2
21.1-20.2
16.2-15.9
11.5-11.3
0.04
0.02
1
0.8
0.6
0.4
0.2
0
0
0.005
0.01
0.015
0.02
Frequency (1/Cumulative Depth)
B.
ME spectral estimates
2
1.5
1
0.5
0
32.6
15.1
21.9
18.2
202.3
56.2
10.2
0
0.005
0.01
0.015
0.02
Frequency (1/Cumulative Depth)

Figure 2.12

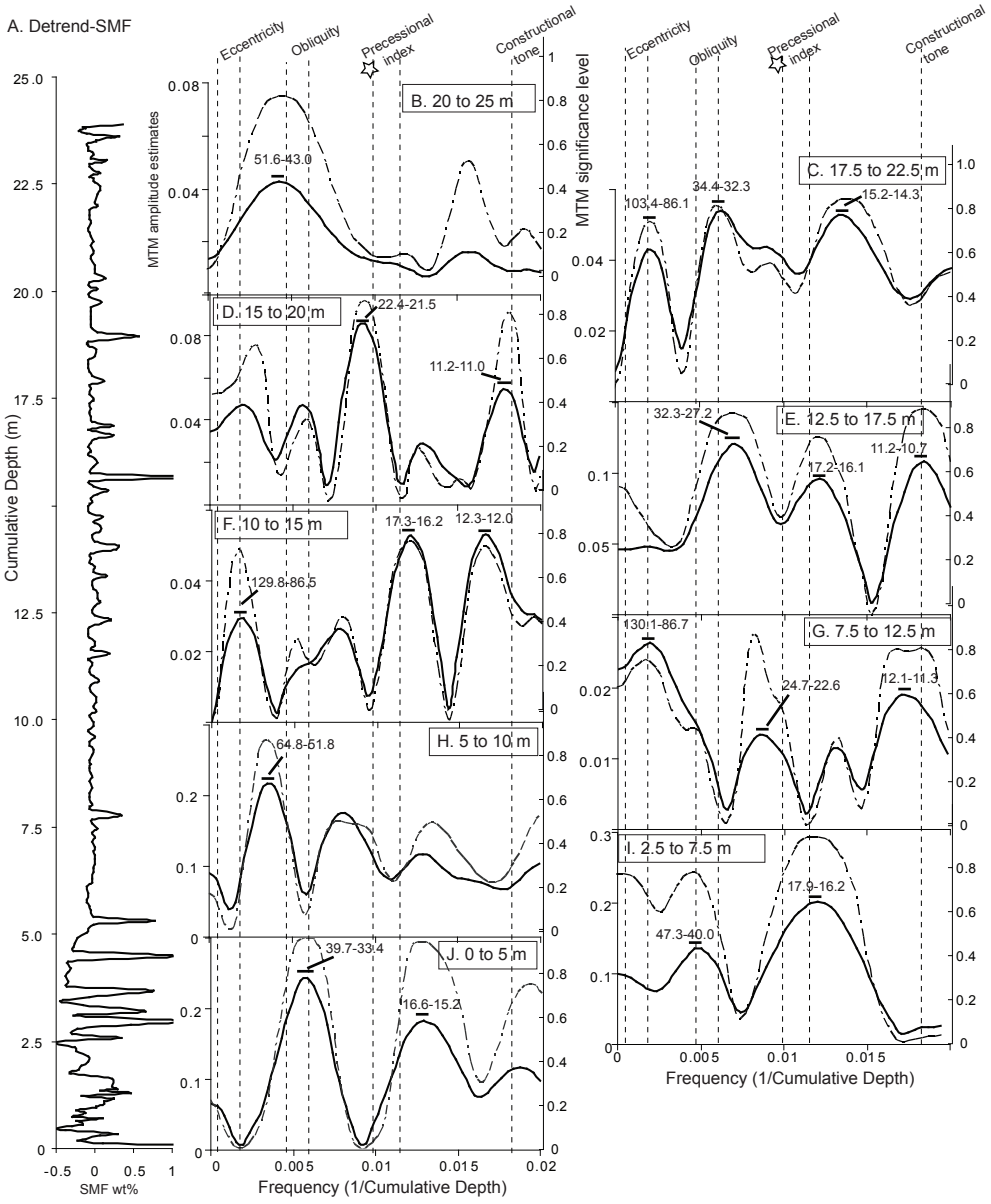
A. Detrend-SMF
Cumulative Depth (m)
SMF wt%
MTM amplitude estimates
MTM significance level
Frequency (1/Cumulative Depth)
Eccentricity
Obliquity
Precessional index
Constructional tone
B. 20 to 25 m
51.6-43.0
C. 17.5 to 22.5 m
103.4-86.1
34.4-32.3
15.2-14.3
D. 15 to 20 m
22.4-21.5
11.2-11.0
E. 12.5 to 17.5 m
32.3-27.2
17.2-16.1
11.2-10.7
F. 10 to 15 m
17.3-16.2
12.3-12.0
129.8-86.5
G. 7.5 to 12.5 m
130.1-86.7
24.7-22.6
12.1-11.3
H. 5 to 10 m
64.8-51.8
I. 2.5 to 7.5 m
17.9-16.2
47.3-40.0
J. 0 to 5 m
39.7-33.4
16.6-15.2

Figure 2.13

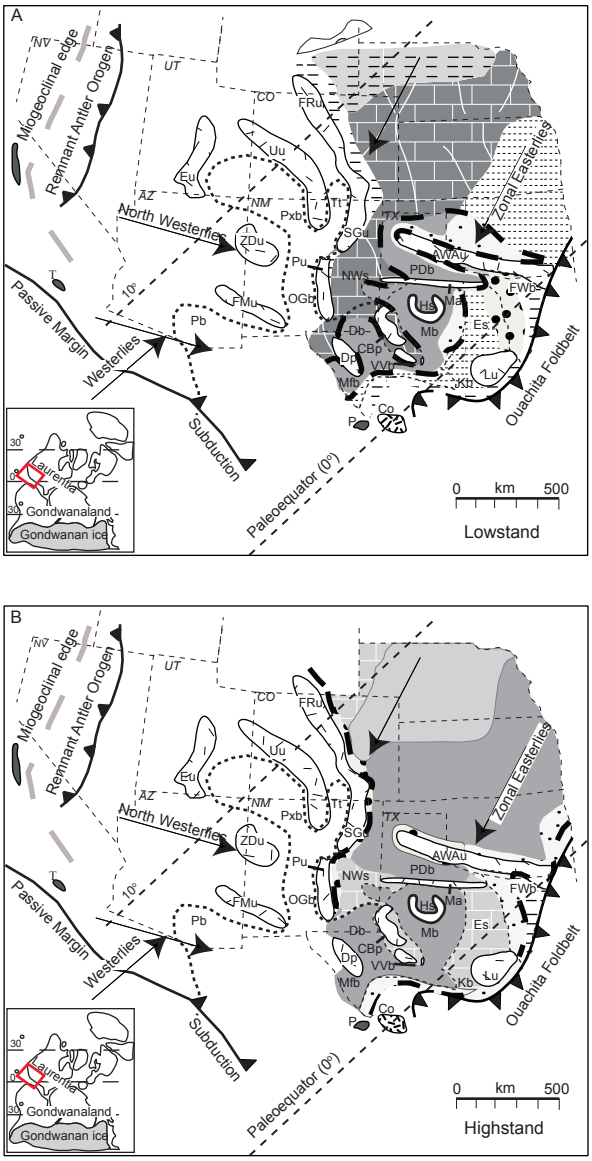

Legend

- Shallow platform carbonate
- Deep basinal shale
- Gray shale (shallower)
- Delta/Prodelta deposits
- Shallow water/Fluvial deposits
- Dunes
- Alluvial deposits
- Exposed carbonate, thin prodeltaic or nonmarine admixture
- Exposed prodelta and delta
- Red soil
- MORB/Volcanic rocks
- Volcanic rocks
- ARM uplift
- Tectonic boundary
- Shoreline position
- Basin boundary
- State boundary
- Miogeoclinal edge

Abbreviations:

AWAu: Amarillo-Wichita-Arbuckle uplift
CBp: Central Basin platform
Co: Coahuila terrane
Db: Delaware basin
Dp: Diablo platform
Es: Eastern shelf
Eu: Emery uplift
FMu: Florida-Moyotes uplift
FRu: Frontal Range uplift
FWb: Fort Worth basin
HS: Horseshoe atoll
Kb: Kerr basin
Lu: Llano uplift
Ma: Matador arch
Mfb: Marfa basin
Mb: Midland basin
NWs: Northwest shelf
OGb: Orogrande basin
P: Parral terrane
PDb: Palo Duro basin
Pb: Pedregosa basin
Pu: Pedernal uplift
Pxb: Paradox basin
SGu: Sierra Grande uplift
T: Tahue terrane
Tt: Taos trough
Uu: Uncompahgre uplift
VVb: Val Verde basin
ZDu: Zuni-Defiance uplift

Figure 2.14

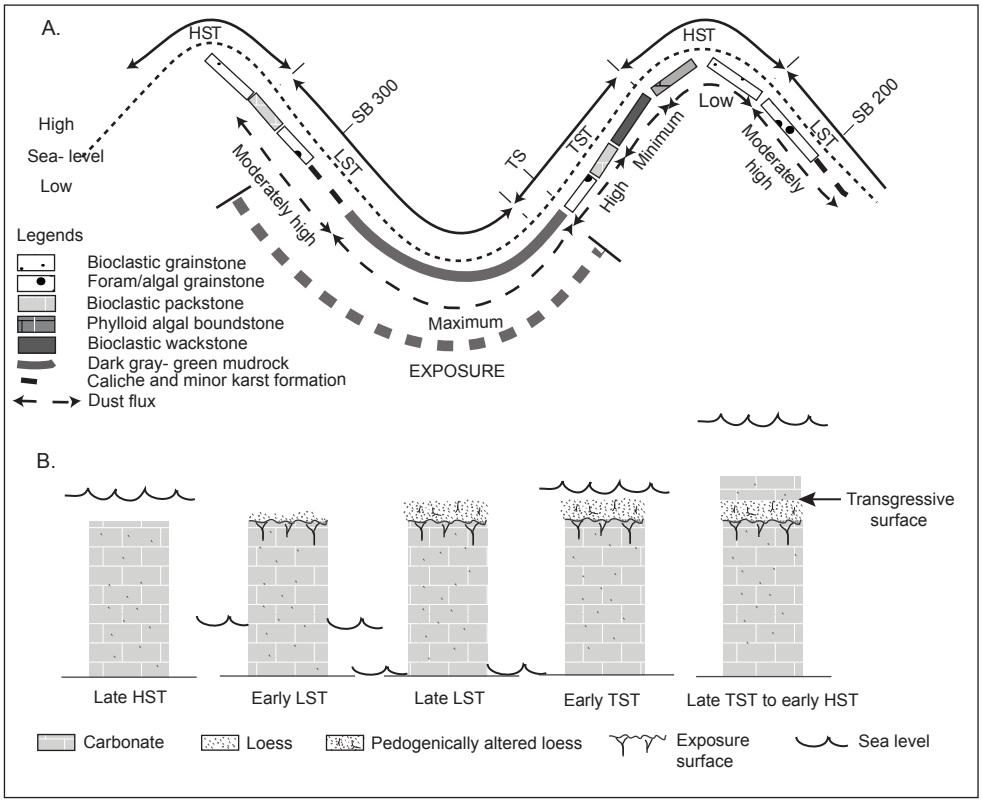
A.
HST
HST
SB 300
SB 200
High
Sea- level
Low
LST
LST
TS
TST
Minimum
High
Low
Moderately high
Moderately high
Legends
Bioclastic grainstone
Foram/algal grainstone
Bioclastic packstone
Phylloid algal boundstone
Bioclastic wackstone
Dark gray- green mudrock
Caliche and minor karst formation
Dust flux
Maximum
EXPOSURE
B.
Transgressive surface
Late HST
Early LST
Late LST
Early TST
Late TST to early HST
Carbonate
Loess
Pedogenically altered loess
Exposure surface
Sea level

Figure 2.15

TABLE 2.1.— Summary of depositional facies

Facies name	Lithology	Grain type	Bedding and structure	Environment	Position in sequence
Foram/algal grainstone	Packstone to grainstone; grainstone	Fragments of algae (phylloid, dasycladacean) and forams (tubular forams and fusulinids), crinoids, bryozoans, ostracods, molluscs, brachiopods and coated and micritized grains	Clay seams; stylolites	High- energy shallow subtidal to intertidal shoal	Sequence top (very late HST to early LST) and sequence base (very early TST)
Bioclastic grainstone	Packstone to grainstone; grainstone	Fragments of crinoids, tubular forams, phylloid algae, fusulinids, bryozoans, tubiphytes and brachiopods	Burrows; clay seams; stylolites	Relatively high-energy shallow subtidal	Sequence top (late HST)
Bioclastic packstone	Packstone	Fragments of crinoids, forams (mainly fusulinids), phylloid algae, tubiphytes, molluscs (e.g. gastropods), ostracods, micritized grains and subordinate peloids and intraclasts	Locally burrows; clay seams; stylolites	Moderate energy shallow subtidal; <20 m depth	Variable positions in the sequence, starting from close to sequence base (early TST) to mid sequence (early HST) to close to sequence top (mid to late HST)
Fusulinid packstone	Packstone	Whole fusulinids with subordinate fragments of phylloid algae	Rare stylolites	Shallow subtidal; 5-20 m depth	Close to the base of the sequence (early to mid TST)
Bioclastic wackestone	Wackestone to mudstone; wackestone	Fragments of crinoids with subordinate fusulinids, tubiphytes and phylloid algae	Clay seams; locally stylolites	Moderately deep subtidal environment below wave base (≥15 to 30 m)	Mid- sequence (MFS)
Phylloid algal boundstone	Wackestone to boundstone; packstone to boundstone	Dominated by algae (phylloid and others) with leached and micritized phylloid algal plates; also contains fragments of crinoids, forams, ostracods and molluscs; locally, tubiphytes and bryozoans predominate over algae.	Autobrecciated texture; styloloites	Photic zone (≤30 m water depth) with abundant baffling of mud.	Generally mid-sequence (early –mid HST)
Dark gray- green mudrock	Mudrock	Dominated by silt sized quartz and clay; 3- 20 % carbonate	Massive; locally micro- laminated; pedogenic structure	Terrestrial	At sequence boundary (LST to early TST)

TABLE 2.2.— Major and Trace Element

Depth (m)	Al (wt%)	Ca (wt%)	Fe (wt%)	K (wt%)	Mg (wt%)	Na (wt%)	S (wt%)	Ti (wt%)	Cr (ppm)	Th (ppm)	Zr (ppm)	CIA
2106.05	0.03	36.4	0.03	0.01	0.16	0.01	0.03	<0.005	8	<0.2	<0.5	68.83
2105.28	0.04	36.5	0.05	0.01	0.17	0.02	0.04	<0.005	7	<0.2	<0.5	65.79
2104.88	0.02	36.1	0.05	<0.01	0.15	0.01	0.05	<0.005	8	<0.2	<0.5	71.81
2104.77	0.04	34.3	0.19	0.01	0.2	0.02	0.22	<0.005	6	<0.2	<0.5	65.79
2104.69	8.04	0.19	3.2	3.58	0.97	0.53	2.77	0.499	90	11.2	116	75.11
2104.60	8	0.15	2.88	3.51	0.99	0.52	2.4	0.492	90	12.7	114.5	75.38
2104.50	7.98	0.81	3.31	3.46	1	0.51	2.97	0.461	89	14.5	107.5	75.61
2104.41	8.04	0.14	2.56	3.51	1	0.54	2.03	0.491	90	13.3	115	75.37
2104.36	7.69	0.34	2.55	3.41	0.96	0.56	2.09	0.472	85	13	110	74.89
2104.29	0.12	34.2	0.08	0.05	0.17	0.02	0.05	0.005	6	0.2	1.6	72.16
2103.99	0.05	35.7	0.04	0.02	0.16	0.02	0.03	<0.005	3	<0.2	0.9	64.79
2103.20	0.04	34.3	0.13	0.01	0.77	0.02	0.02	<0.005	4	<0.2	0.8	65.79
2102.13	0.03	30.4	0.59	0.01	3.36	0.02	0.1	<0.005	2	<0.2	0.6	59.05
2100.61	0.03	24.3	1.1	0.01	6.11	0.03	0.06	<0.005	4	<0.2	0.7	51.71
2098.55	0.02	17.9	1.97	0.01	11.3	0.05	0.08	<0.005	2	<0.2	0.6	32.03
2095.53	0.02	18.4	1.45	<0.01	11.75	0.06	0.02	<0.005	4	<0.2	<0.5	31.29
2092.57	0.03	35	0.1	0.01	0.6	0.02	0.02	<0.005	2	<0.2	0.8	59.05
2091.54	0.02	36.1	0.03	0.01	0.14	0.02	0.02	<0.005	2	<0.2	0.5	49.02
2089.88	0.01	36.2	0.02	<0.01	0.14	0.03	0.02	<0.005	2	<0.2	<0.5	30.98
2089.04	0.03	41.8	0.03	0.01	0.15	0.03	<0.01	<0.005	<1	<0.2	0.6	51.71
2087.42	0.03	37.5	0.06	0.01	0.18	0.04	0.05	<0.005	2	<0.2	0.5	45.99
2086.39	0.02	36.9	0.03	0.01	0.15	0.03	0.02	<0.005	1	<0.2	0.9	41.65
2084.77	0.03	36.1	0.06	0.01	0.15	0.03	0.06	<0.005	3	<0.2	0.7	51.71
2083.98	0.02	35.2	0.11	<0.01	0.15	0.03	0.1	<0.005	2	<0.2	0.5	47.31
2082.91	0.02	37.4	0.04	0.01	0.17	0.03	0.04	<0.005	3	<0.2	<0.5	41.65
2082.30	0.01	35.9	0.98	<0.01	0.25	0.03	1.25	<0.005	3	<0.2	<0.5	30.98
2081.28	0.04	33.9	0.25	0.01	1.68	0.03	0.04	<0.005	3	<0.2	0.5	58.81
2080.67	0.02	35.8	0.08	<0.01	0.42	0.01	0.01	<0.005	3	<0.2	<0.5	71.81
2080.46	0.09	41.2	0.07	0.04	0.3	0.02	0.01	<0.005	5	<0.2	0.7	69.27
2080.35	0.07	35.4	0.13	0.02	0.51	0.02	0.07	<0.005	5	<0.2	0.8	72.03
2080.21	0.09	34.5	0.15	0.03	0.3	0.02	0.12	<0.005	4	0.2	1.3	72.84
2079.82	0.02	36.3	0.79	0.01	0.54	0.02	0.96	<0.005	4	<0.2	0.6	49.02
2079.59	0.04	32.4	0.94	0.01	1.42	0.02	0.96	<0.005	2	<0.2	1	65.79
2079.41	0.03	33.9	0.78	0.01	1.71	0.02	0.7	<0.005	2	<0.2	0.7	59.05
2079.16	0.04	34	0.5	0.01	0.64	0.02	0.54	<0.005	2	<0.2	0.9	65.79

TABLE 2.3.— Age models

Age model references	Top of Virgilian	Base of Virgilian	Model no.	Top error	Base error	Duration of Virgilian	Duration of middle Virgilian*	Calculated time interval of studied sequence (SB 300 to SB 200)†
	(Ma)	(Ma)		(My)	(My)	(My)	(My)	(kyr)
Vladimir Davydov (pers. commun. 2008)	299.7	302.4	1	n.a.	n.a.	2.7	0.90	300
Gradstein et al. 2004	300.2 (±0.8)	303.1 (±0.9)	2	-0.8	-0.9	2.8	0.93	311
			3	0	-0.9	2	0.67	222
			4	0.8	-0.9	1.2	0.40	133
			5	-0.8	0	3.7	1.23	411
			6	0	0	2.9	0.97	322
			7	0.8	0	2.1	0.70	233
			8	-0.8	0.9	4.6	1.53	511
			9	0	0.9	3.8	1.27	422
Rasbury et al. 1998	302 (±2.4)	307 (±3)	11	-2.4	-3	4.4	1.47	489
			12	0	-3	2	0.67	222
			13	2.4	-3	-0.4	-0.13	n.d.
			14	-2.4	0	7.4	2.47	822
			15	0	0	5	1.67	556
			16	2.4	0	2.6	0.87	289
			17	-2.4	3	10.4	3.47	1156
			18	0	3	8	2.67	889
			19	2.4	3	5.6	1.87	622
Wilde 1990	288.5	292	20	n.a.	n.a.	3.5	1.17	389
	-	-	21	n.a.	n.a.	n.a.	1.00	333

* Age of middle Virgilian is estimated by dividing duration of Virgilian by three for all age models except model no. 21.

† Time interval of the studied sequence is estimated by dividing duration of Middle Virgilian by three for all age models.

n.a. = Data not available

n.d. = Not determined as the computed age of Virgilian is negative for the age model

TABLE 2.4.— Calibration scheme of SMF spectra

		Detrended data (All- sized SMF)	
	Expected Milankovitch periodicity and constructional tone during 300 Ma	Calibration scheme-1 (20.7 kyr calibrated to frequency = 0.009776)*	Calibration scheme-2 (100 kyr calibrated to frequency = 0.002248)§
Precession-1	17.4 kyr (Berger et al. 1992)	16.2 to 15.9 kyr	19.6 to 19.2 kyr
Precession-2	20.7 kyr (Berger et al. 1992)	23.2 to 20.2 kyr	28.0 to 24.5 kyr
Obliquity-1	34.2 kyr (Berger et al. 1992)	31.8 to 30.8 kyr	38.4 to 37.3 kyr
Obliquity-2	42.9 kyr (Berger et al. 1992)	not detected	not detected
Eccentricity-1	123 to 95 kyr (Berger. 1977)	90.0 to 79.6 kyr	108.7 to 96.1 kyr
Eccentricity-2	413 kyr (Berger. 1977)	345.3 to 258.7 kyr	417.0 to 312.5 kyr
Constructional tone-1[t]	9.45 kyr	11.5 to 11.3 kyr	13.9 to 13.7 kyr
Constructional tone-2[†]	49.8 kyr	55.9 to 51.7 kyr	62.5 to 67.5 kyr

* Calculated sedimentation rate = 4.94 cm/kyr.

§ Calculated sedimentation rate = 4.44 cm/kyr.

[t] Constructional tone between short and long precessional index cycles (see text for details).

[†] Constructional tone by combination of short and long precessional index with short obliquity cycles (see text for details).

TABLE 2.5.— Summary of dust influx

Eustatic phase		Climatic phase	Lithology and environment	Average SMF (wt%)	Relative variation of SMF with respect to minimum SMF*	Atmospheric dustiness and aridity	Average SMF MAR ($g/cm^2/kyr$)
LST	Early	Incipient glacial	Very shallow marine Carbonate	0.3034	3.76	Moderately high	0.022
	Late	Glacial	Terrestrial mudrock (pedogenically altered loess)	89.7254	1113.22	Maximum	3.524
TST	Early	Incipient interglacial	Terrestrial mudrock (pedogenically altered loess) and very shallow to shallow marine carbonate	0.847	10.51	High	0.0506
	Late	Interglacial	Relatively deep marine carbonate	0.0806	1.00	Minimum	0.0033
HST	Early	Interglacial	Intermediate depth marine carbonate	0.0806 to 0.1036	1 to 1.28	Minimum to low	0.0033 to 0.0089
	Late	Interglacial	Shallow marine carbonate	0.1036	1.29	Low	0.0089

* Relative variation of SMF is calculated by dividing average SMF (wt%) by minimum average SMF (wt%).

TABLE 2A.1: Stratigraphic location and SMF analysis

Depth	Facies	Bulk Wt.	Insoluble residue - Organic matter	Silicate mineral fraction (SMF)			Grain size of silt- sized SMF					
				Silt sized (<62.5 µm)	Sand sized (>62.5 µm)	Total (All-sized)	Mean	Median	Mode	d10	d90	SD
(m)		(g)	(wt%)	(wt%)	(wt%)	(wt%)	(µm)	(µm)	(µm)	(µm)	(µm)	(µm)
2106.05	b-gst	50.00	0.30	0.21	0.03	0.24	8.94	12.12	21.69	1.30	36.08	3.58
2105.92	b-gst	50.01	0.21	0.16	0.03	0.19	17.31	24.30	37.97	2.83	63.32	3.83
2105.86	b-gst	50.01	0.23	0.17	0.03	0.20	17.63	24.73	31.50	3.18	60.81	3.87
2105.82	b-gst	50.01	0.42	0.23	0.06	0.29	8.34	11.99	19.76	1.09	32.92	3.65
2105.77	b-gst	50.00	0.29	0.21	0.05	0.26	16.18	23.13	28.70	2.30	54.99	3.84
2105.73	b-gst	50.00	0.28	0.20	0.04	0.24	14.85	20.33	26.14	1.91	58.47	3.94
2105.68	b-gst	50.00	0.35	0.16	0.16	0.33	13.41	19.38	21.14	1.52	48.50	3.90
2105.62	b-gst	50.00	0.43	0.14	0.16	0.30	11.55	16.75	23.81	1.25	45.44	4.05
2105.41	b-pkst	50.00	0.41	0.13	0.16	0.30	15.91	22.64	34.58	2.06	59.02	3.91
2105.31	b-pkst	50.00	1.57	0.45	0.30	0.76	7.67	13.01	21.69	0.54	40.44	5.12
2105.28	b-pkst	50.00	0.48	0.26	0.14	0.40	12.57	18.34	26.14	1.32	47.90	4.05
2105.22	fa-gst	49.00	0.33	0.20	0.05	0.25	9.37	13.31	19.76	1.21	36.08	3.74
2105.18	fa-gst	50.00	0.56	0.20	0.27	0.47	8.72	9.50	23.81	1.67	39.53	3.33
2105.13	fa-gst	50.00	0.76	0.17	0.54	0.71	18.88	26.97	41.68	3.11	65.84	3.77
2105.07	fa-gst	50.01	2.58	0.25	2.24	2.49	10.51	13.71	21.69	1.73	40.54	3.44
2105.01	fa-gst	50.01	1.21	0.43	0.26	0.69	12.18	17.58	23.81	1.41	46.13	3.87
2104.98	fa-gst	50.01	0.76	0.36	0.32	0.68	12.89	18.42	23.81	1.42	48.80	3.92
2104.93	fa-gst	50.01	2.40	0.53	0.36	0.90	9.87	13.76	19.76	1.19	40.66	3.91
2104.88	fa-gst	38.36	1.19	0.41	0.44	0.86	12.13	16.90	28.70	1.34	52.43	4.07
2104.83	fa-gst	50.00	0.38	0.22	0.07	0.30	9.69	12.48	18.00	1.76	34.84	3.31
2104.77	fa-gst	50.00	1.01	0.42	0.52	0.94	10.89	15.11	21.69	1.37	41.75	3.79
2104.74	fa-gst	50.01	0.88	0.44	0.35	0.79	13.16	18.47	26.14	1.44	56.52	4.16
2104.69	mdrk	50.01	92.65	nd	nd	88.90	nd*	nd	nd	nd	nd	nd
2104.67	mdrk	50.01	91.73	nd	nd	87.87	nd	nd	nd	nd	nd	nd
2104.64	mdrk	50.01	93.03	nd	nd	92.42	nd	nd	nd	nd	nd	nd
2104.62	mdrk	50.00	93.55	nd	nd	nd	nd	nd	nd	nd	nd	nd
2104.60	mdrk	50.01	90.20	nd	nd	87.90	nd	nd	nd	nd	nd	nd
2104.57	mdrk	50.00	93.98	nd	nd	91.26	nd	nd	nd	nd	nd	nd
2104.55	mdrk	50.00	86.95	nd	nd	81.89	nd	nd	nd	nd	nd	nd
2104.53	mdrk	50.00	94.26	nd	nd	92.84	nd	nd	nd	nd	nd	nd
2104.50	mdrk	50.00	91.90	nd	nd	89.03	nd	nd	nd	nd	nd	nd
2104.48	mdrk	50.01	93.75	nd	nd	90.04	nd	nd	nd	nd	nd	nd
2104.46	mdrk	50.01	92.35	nd	nd	89.69	nd	nd	nd	nd	nd	nd
2104.43	mdrk	50.01	92.60	nd	nd	87.71	nd	nd	nd	nd	nd	nd
2104.41	mdrk	50.00	93.01	nd	nd	89.76	nd	nd	nd	nd	nd	nd
2104.39	mdrk	50.00	97.62	nd	nd	nd	nd	nd	nd	nd	nd	nd
2104.36	mdrk	50.01	93.97	nd	nd	93.02	nd	nd	nd	nd	nd	nd
2104.34	mdrk	49.43	93.45	nd	nd	91.74	nd	nd	nd	nd	nd	nd
2104.29	fa-gst	50.01	3.94	3.60	0.04	3.64	5.24	6.54	10.30	0.82	23.62	3.62
2104.25	fa-gst	50.00	7.34	6.66	0.03	6.69	3.69	3.50	2.54	0.97	15.61	2.82
2104.20	fu-pkst	50.01	1.82	2.10	0.03	2.13	7.18	10.34	16.40	0.87	29.57	3.89
2104.16	fu-pkst	50.01	1.38	1.14	0.02	1.16	7.48	10.75	16.40	0.92	28.32	3.78
2104.10	fu-pkst	50.00	1.03	0.72	0.09	0.81	9.78	14.33	21.69	1.05	38.36	4.01
2104.06	fu-pkst	50.01	0.98	0.88	0.03	0.91	8.18	11.62	16.40	1.00	31.37	3.78
2103.99	fu-pkst	50.01	1.24	1.00	0.09	1.09	9.92	14.48	19.76	1.06	38.80	3.98
2103.94	fu-pkst	50.01	1.38	1.27	0.04	1.31	8.46	12.05	18.00	1.04	32.67	3.79
2103.87	fu-pkst	50.01	0.70	0.55	0.07	0.63	10.13	14.61	21.69	1.20	38.38	3.84
2103.82	fu-pkst	50.01	0.48	0.43	0.02	0.44	8.78	12.37	18.00	1.12	32.35	3.69
2103.76	fu-pkst	50.00	0.77	0.57	0.11	0.69	11.05	16.20	21.69	1.19	41.54	3.95
2103.73	fu-pkst	50.01	0.86	0.80	0.02	0.83	8.80	12.69	18.00	1.10	32.29	3.73
2103.68	b-pkst	50.01	0.89	0.75	0.05	0.80	9.43	13.37	18.00	1.17	35.17	3.72
2103.64	b-pkst	50.00	0.77	0.72	0.02	0.73	8.87	12.74	18.00	1.08	33.99	3.81
2103.58	b-pkst	50.00	1.21	0.94	0.13	1.07	10.58	14.97	21.69	1.31	40.96	3.81
2103.55	b-pkst	50.00	0.73	0.65	0.02	0.67	9.04	12.96	18.00	1.09	34.46	3.83
2103.46	b-pkst	50.01	0.87	0.80	0.02	0.82	9.29	13.06	19.80	1.23	36.03	3.69
2103.39	b-pkst	50.00	0.77	0.65	0.04	0.69	12.70	18.18	23.81	1.36	48.50	4.01
2103.35	b-pkst	50.01	1.01	0.92	0.03	0.95	9.41	12.83	19.80	1.38	35.22	3.57
2103.30	b-pkst	50.00	1.01	0.86	0.08	0.94	11.00	16.08	21.69	1.17	42.44	4.01
2103.24	b-pkst	50.01	1.12	1.00	0.03	1.03	10.90	15.11	21.70	1.39	41.94	3.78
2103.20	b-pkst	50.01	1.14	0.93	0.09	1.02	7.70	11.17	16.40	0.89	31.45	3.94
2103.12	b-pkst	50.01	1.17	1.12	0.02	1.14	9.04	12.75	18.90	1.14	35.04	3.74

2103.06	b-pkst	50.01	0.84	0.63	0.08	0.71	11.57	16.04	21.69	1.45	44.15	3.84
2103.00	b-pkst	50.01	1.35	1.31	0.03	1.34	11.70	16.71	26.10	1.33	48.70	4.04
2102.94	b-pkst	50.00	1.08	0.86	0.08	0.94	8.96	12.49	18.00	1.13	35.81	3.80
2102.91	b-pkst	50.01	1.20	1.11	0.03	1.15	8.73	12.47	18.00	1.13	31.96	3.67
2102.85	b-pkst	50.01	1.14	1.04	0.04	1.08	8.73	12.31	17.20	1.13	31.84	3.65
2102.66	b-pkst	50.01	1.10	1.01	0.03	1.04	7.58	10.69	16.40	0.99	30.43	3.78
2102.54	b-pkst	50.01	0.55	0.49	0.01	0.50	10.18	14.63	19.80	1.25	37.86	3.79
2102.46	b-pkst	50.00	0.61	0.57	0.01	0.58	8.71	12.32	18.00	1.09	33.37	3.77
2102.36	b-pkst	50.01	0.70	0.52	0.09	0.61	11.13	15.54	21.69	1.31	44.30	3.92
2102.27	b-pkst	50.00	1.08	0.61	0.08	0.69	10.53	14.42	18.88	1.27	42.94	3.91
2102.13	b-pkst	50.01	0.68	0.56	0.09	0.65	9.02	12.39	16.40	1.11	36.06	3.86
2102.02	b-pkst	50.01	0.56	0.44	0.06	0.50	8.58	11.62	16.40	1.20	31.66	3.59
2101.92	b-pkst	50.00	0.63	0.38	0.08	0.46	9.39	13.39	18.00	1.22	33.17	3.64
2101.81	b-pkst	50.01	0.17	0.13	0.02	0.15	22.64	31.82	41.68	6.06	70.14	3.73
2101.72	b-pkst	50.00	1.13	0.92	0.11	1.03	13.64	19.37	31.50	1.46	57.77	4.11
2101.63	b-pkst	50.01	0.42	0.32	0.06	0.38	9.19	12.93	18.00	1.09	34.36	3.80
2101.50	b-pkst	50.01	0.46	0.37	0.05	0.42	9.39	13.06	18.00	1.22	35.22	3.67
2101.41	b-pkst	50.00	1.23	0.96	0.15	1.11	16.43	23.63	37.97	1.91	63.22	4.05
2101.32	b-pkst	50.01	1.95	1.55	0.23	1.78	10.09	14.36	19.76	1.18	40.69	3.90
2101.20	b-pkst	50.01	0.37	0.26	0.07	0.33	15.81	21.67	37.97	1.88	65.21	4.03
2101.11	b-pkst	50.00	1.44	1.09	0.15	1.24	8.90	12.41	18.00	1.11	36.31	3.83
2100.96	b-pkst	50.01	0.48	0.35	0.05	0.41	8.10	11.41	16.40	1.01	31.81	3.77
2100.86	dolo	50.01	0.17	0.10	0.02	0.11	6.40	8.60	13.61	0.84	23.46	3.69
2100.76	dolo	50.00	0.58	0.41	0.06	0.46	7.84	10.00	13.61	1.18	30.11	3.63
2100.61	dolo	50.01	1.38	1.05	0.22	1.27	15.38	20.83	28.70	2.13	58.83	3.88
2100.53	dolo	50.00	0.21	0.12	0.02	0.14	6.19	8.20	12.40	1.05	21.82	3.33
2100.41	dolo	50.00	0.19	0.12	0.01	0.13	8.42	11.19	14.94	1.42	28.95	3.37
2100.29	dolo	50.01	0.13	0.08	0.01	0.09	9.00	11.68	16.40	1.39	32.00	3.60
2100.16	dolo	50.00	0.47	0.09	0.01	0.11	7.20	9.77	14.94	1.12	25.56	3.45
2100.07	dolo	50.00	0.19	0.10	0.02	0.12	6.44	8.45	12.40	1.08	23.31	3.38
2099.92	dolo	50.00	0.09	0.05	0.02	0.07	7.04	9.42	13.67	1.14	24.92	3.39
2099.80	dolo	50.01	0.14	1.43	0.02	1.45	7.64	10.39	14.94	1.20	26.52	3.41
2099.68	dolo	50.00	0.14	0.09	0.02	0.10	8.08	10.83	14.94	1.32	27.49	3.35
2099.58	dolo	50.01	0.11	0.08	0.01	0.09	8.39	11.13	16.40	1.36	29.95	3.41
2099.49	dolo	50.01	0.10	0.07	0.02	0.08	7.40	10.10	14.94	1.16	25.46	3.42
2099.37	dolo	50.01	0.19	0.10	0.01	0.11	6.50	8.71	13.01	1.09	22.52	3.33
2099.25	dolo	50.00	0.28	0.17	0.03	0.20	6.81	9.28	14.28	1.04	24.82	3.48
2099.07	dolo	50.00	0.33	0.23	0.04	0.27	6.70	8.96	12.40	1.06	23.99	3.43
2098.97	dolo	50.01	nd	0.79	0.27	1.06	10.75	14.08	18.00	1.64	39.09	3.48
2098.88	dolo	50.01	0.30	0.20	0.05	0.25	8.97	11.72	15.81	1.41	33.06	3.45
2098.75	dolo	50.01	0.47	0.15	0.03	0.18	7.19	9.36	13.61	1.18	27.03	3.43
2098.64	dolo	50.00	0.25	0.12	0.04	0.15	10.96	13.72	16.40	1.38	54.22	4.14
2098.55	dolo	50.00	0.14	0.08	0.02	0.10	8.54	11.50	16.40	1.37	29.89	3.44
2098.50	dolo	50.00	0.13	0.08	0.02	0.10	6.49	8.59	13.61	1.07	23.80	3.39
2098.33	dolo	50.01	0.13	0.07	0.02	0.08	7.04	9.35	13.61	1.10	26.37	3.50
2098.18	dolo	50.01	0.12	0.05	0.01	0.06	7.72	10.60	14.94	1.11	28.22	3.56
2098.09	dolo	50.01	0.16	0.10	0.01	0.11	5.63	7.47	12.40	0.92	20.97	3.42
2098.00	dolo	50.00	0.15	0.09	0.00	0.10	9.46	11.20	13.61	1.28	54.16	4.20
2097.85	dolo	50.00	0.14	0.07	0.00	0.08	6.44	8.98	13.61	0.93	23.48	3.58
2097.76	dolo	50.01	0.09	0.05	0.01	0.06	7.38	10.17	14.28	1.05	26.70	3.58
2097.66	dolo	50.01	0.09	0.07	0.01	0.08	6.94	9.60	14.94	0.92	25.86	3.83
2097.54	dolo	50.00	0.10	0.04	0.01	0.05	7.59	10.16	14.94	1.13	29.44	3.60
2097.45	dolo	50.00	0.07	0.04	0.01	0.05	8.26	10.65	14.94	1.17	32.02	3.79
2097.36	dolo	50.01	0.08	0.06	0.02	0.08	9.41	10.90	14.94	1.01	75.48	4.99
2097.25	dolo	50.01	0.09	0.07	0.02	0.09	7.51	10.70	16.40	1.01	27.33	3.64
2097.15	dolo	50.00	0.08	0.06	0.01	0.06	5.93	8.40	13.61	0.78	23.72	3.78
2097.05	dolo	50.01	0.12	0.08	0.01	0.09	6.48	8.72	13.61	1.10	22.28	3.32
2096.93	dolo	50.00	0.09	0.05	0.02	0.06	6.42	9.56	14.94	0.76	25.53	3.91
2096.84	dolo	50.00	0.16	0.10	0.03	0.13	7.22	9.95	14.94	1.01	27.53	3.65
2096.72	dolo	50.00	0.09	0.05	0.01	0.06	5.32	6.75	11.29	0.94	20.35	3.33
2096.63	dolo	50.00	0.07	0.05	0.01	0.06	7.00	9.60	13.61	1.03	25.69	3.55
2096.52	dolo	50.01	0.61	0.05	0.39	0.44	7.45	9.68	13.61	1.09	32.28	3.70
2096.38	dolo	50.00	0.03	0.01	0.01	0.03	7.58	10.16	13.61	1.16	27.31	3.46
2096.29	dolo	50.00	0.08	0.04	0.02	0.07	10.73	9.86	11.29	0.89	27.67	6.99
2096.20	dolo	50.01	0.06	0.03	0.02	0.05	6.99	9.05	12.40	0.92	28.03	4.04
2096.08	dolo	50.00	0.03	0.01	0.01	0.03	7.88	10.25	13.61	1.07	32.97	3.82
2095.99	dolo	50.00	0.04	0.03	0.01	0.03	6.53	9.07	13.61	0.95	23.92	3.53
2095.87	dolo	50.00	0.06	0.04	0.03	0.06	6.11	7.96	12.40	0.93	24.97	3.60
2095.73	dolo	50.00	0.04	0.02	0.01	0.03	6.55	9.04	13.61	0.97	24.37	3.53

2095.62	dolo	50.00	0.06	0.02	0.04	0.06	5.65	7.56	13.61	0.71	28.71	4.13
2095.53	dolo	50.00	0.06	0.03	0.02	0.04	5.75	7.69	11.85	0.84	23.41	3.66
2095.42	dolo	50.00	0.04	0.02	0.00	0.02	6.14	8.31	12.40	0.85	24.67	3.74
2095.32	dolo	50.00	0.05	0.03	0.01	0.04		6.18	9.37	0.85	20.07	3.44
2095.23	b-wkst	50.01	0.04	0.02	0.01	0.03	5.17	6.36	10.29	0.88	21.90	3.49
2095.10	b-wkst	50.00	0.08	0.06	0.00	0.06	9.09	12.00	16.40	1.19	37.43	3.79
2095.00	b-wkst	50.00	0.11	0.08	0.01	0.09	9.16	12.61	20.73	1.23	35.77	3.69
2094.89	b-wkst	50.00	0.04	0.03	0.01	0.04	11.90	14.75	20.73	1.64	53.42	3.79
2094.80	b-wkst	50.00	0.03	0.02	0.01	0.03	11.82	16.30	26.14	1.41	50.70	3.95
2094.68	b-wkst	50.00	0.11	0.09	0.01	0.10	9.89	13.62	21.69	1.19	43.10	4.00
2094.56	b-wkst	50.00	0.02	0.01	0.01	0.02	11.62	15.69	26.14	1.53	47.33	3.64
2094.43	b-wkst	50.00	0.10	0.07	0.01	0.08	7.08	9.56	18.00	0.89	33.04	3.99
2094.34	b-wkst	50.00	0.11	0.08	0.01	0.09	7.61	9.95	16.40	1.07	33.86	3.80
2094.19	b-wkst	50.00	0.04	0.03	0.01	0.04		9.28	13.61	1.13	32.53	3.61
2094.10	b-wkst	50.00	0.15	0.10	0.01	0.11	6.92	9.56	18.00	0.84	32.83	4.08
2093.98	b-wkst	50.00	0.09	0.07	0.01	0.08	5.78	7.27	14.94	0.83	28.14	3.84
2093.88	b-wkst	50.00	0.13	0.06	0.05	0.12	5.85	7.38	13.61	0.85	27.63	3.79
2093.76	b-wkst	50.00	0.16	0.11	0.02	0.12	4.67	5.73	11.29	0.66	24.47	3.99
2093.64	b-wkst	50.00	0.08	0.05	0.01	0.06	5.64	6.64	11.29	0.93	26.62	3.59
2093.47	b-wkst	50.00	0.06	0.03	0.02	0.06	5.17	6.06	9.37	0.78	27.43	3.89
2093.40	b-wkst	50.00	0.19	0.08	0.07	0.15	4.88	5.56	8.54	0.84	23.52	3.54
2093.27	b-wkst	50.01	0.11	0.07	0.01	0.08	4.45	4.77	5.88	0.89	20.46	3.27
2093.18	b-wkst	50.01	0.19	0.03	0.00	0.03	10.92	14.27	26.10	1.54	47.98	3.89
2092.97	b-wkst	50.01	0.13	0.04	0.03	0.07	4.60	5.24	7.78	0.77	22.74	3.63
2092.88	b-wkst	50.00	0.12	0.01	0.00	0.02	21.11	20.22	26.10	1.65	38.20	6.96
2092.76	b-wkst	50.01	0.34	0.04	0.26	0.30	9.39	11.39	24.95	1.20	53.66	4.28
2092.67	b-wkst	50.00	0.10	0.05	0.00	0.05	6.37	7.14	8.54	0.95	34.93	3.99
2092.57	b-wkst	50.00	0.21	0.09	0.00	0.09	4.39	4.64	5.88	1.05	11.24	2.91
2092.48	b-wkst	50.00	0.22	0.10	0.01	0.11	8.75	7.84	6.45	1.04	108.65	5.48
2092.39	b-wkst	50.01	0.11	0.03	0.01	0.04	9.58	9.67	9.37	1.10	99.40	5.10
2092.30	b-wkst	50.00	0.03	0.02	0.00	0.02	9.15	10.74	23.80	1.16	54.14	4.34
2092.12	b-pkst	50.00	0.10	0.03	0.00	0.03	9.84	9.32	8.54	1.15	122.30	5.27
2092.03	b-pkst	50.00	0.25	0.14	0.05	0.18	9.80	11.31	12.40	1.30	56.52	4.22
2091.93	b-gst	50.00	0.38	0.14	0.16	0.30	6.71	7.98	11.29	0.94	36.01	4.01
2091.84	b-gst	50.00	0.19	0.07	0.03	0.11	6.61	7.97	10.29	0.98	31.51	3.85
2091.74	b-gst	50.01	0.10	0.06	0.01	0.07	10.22	12.43	14.94	1.28	55.62	4.24
2091.63	b-gst	50.00	0.13	0.08	0.01	0.10	11.63	14.23	19.76	1.79	51.68	3.84
2091.54	b-gst	50.00	0.25	0.17	0.00	0.17	7.22	7.40	8.54	1.14	51.48	4.09
2091.45	pa-bdst	50.00	0.19	0.08	0.05	0.13	6.39	7.37	9.37	0.96	35.15	3.94
2091.34	pa-bdst	50.00	0.22	0.14	0.00	0.14	6.00	7.02	9.37	0.98	28.42	3.67
2091.23	pa-bdst	50.00	0.13	0.08	0.00	0.08	5.65	6.52	8.54	1.14	22.34	3.16
2091.14	pa-bdst	50.00	0.10	0.07	0.01	0.07	7.18	8.15	10.30	0.97	43.30	4.29
2091.03	pa-bdst	50.00	0.12	0.07	0.02	0.09	8.07	9.87	12.40	1.01	43.33	4.21
2090.93	pa-bdst	50.01	0.29	0.09	0.17	0.25	7.35	8.01	9.37	1.41	32.25	3.42
2090.84	pa-bdst	50.00	0.11	0.05	0.03	0.08	7.69	9.17	12.40	1.12	37.14	3.91
2090.71	pa-bdst	50.01	0.14	0.08	0.03	0.11	5.63	6.46	9.83	1.10	23.31	3.20
2090.62	pa-bdst	50.01	0.06	0.04	0.00	0.04	6.54	7.84	10.29	1.02	29.75	3.72
2090.53	pa-bdst	50.00	0.08	0.06	0.00	0.06	7.28	8.74	11.85	1.09	35.07	3.79
2090.41	pa-bdst	50.00	0.08	0.06	0.00	0.06	6.79	8.13	10.29	1.08	31.56	3.65
2090.32	pa-bdst	50.00	0.42	0.09	0.28	0.38	5.21	6.00	8.54	1.00	22.21	3.29
2090.23	pa-bdst	50.00	0.44	0.08	0.33	0.41	7.42	8.39	10.29	1.26	35.90	3.62
2090.14	b-pkst	50.01	0.13	0.04	0.06	0.10	6.56	8.31	12.40	0.94	30.33	3.84
2089.98	b-pkst	50.00	0.09	0.06	0.00	0.06	6.29	8.08	12.40	0.95	27.28	3.63
2089.88	b-pkst	50.00	0.21	0.08	0.09	0.17	7.64	10.46	16.40	1.02	32.74	3.78
2089.77	b-pkst	50.01	0.21	0.05	0.12	0.18	7.30	9.60	16.40	1.03	31.98	3.72
2089.66	b-pkst	50.00	0.11	0.04	0.04	0.09	6.71	8.70	12.40	0.96	29.58	3.74
2089.56	b-pkst	50.01	0.23	0.06	0.14	0.20	6.84	8.71	12.40	1.07	29.13	3.54
2089.45	b-pkst	50.00	0.05	0.03	0.00	0.03	6.98	8.70	11.29	1.01	32.44	3.81
2089.31	b-pkst	50.01	0.05	0.02	0.00	0.02	5.64	6.32	7.78	1.20	22.15	3.16
2089.22	b-pkst	50.00	0.11	0.06	0.00	0.06	6.06	7.37	10.29	1.10	24.06	3.24
2089.13	b-pkst	50.00	0.07	0.03	0.02	0.05	5.55	6.75	9.37	0.92	24.82	3.56
2089.04	b-pkst	50.00	0.18	0.05	0.10	0.15	5.29	6.27	8.54	1.01	21.30	3.27
2088.95	pa-bdst	50.00	0.30	0.07	0.22	0.28	6.84	8.93	13.61	1.03	27.78	3.55
2088.86	pa-bdst	50.00	0.15	0.06	0.02	0.08	5.10	5.92	8.54	1.04	20.14	3.12
2088.73	pa-bdst	50.01	0.05	0.02	0.02	0.03	6.71	8.11	10.29	1.21	26.47	3.33
2088.64	pa-bdst	50.01	1.52	0.08	1.38	1.45	6.11	7.54	10.06	1.05	24.40	3.42
2088.55	pa-bdst	50.01	0.10	0.03	0.02	0.05	5.50	6.97	9.83	0.89	22.33	3.51
2088.40	pa-bdst	50.00	0.49	0.06	0.02	0.08	4.92	6.03	8.95	0.86	20.35	3.41
2088.31	pa-bdst	50.01	0.28	0.13	0.01	0.14	4.91	5.69	8.54	0.98	19.76	3.19

2088.22	pa-bdst	50.01	0.14	0.02	0.08	0.10	6.15	7.75	10.29	0.97	25.98	3.60
2088.09	pa-bdst	50.00	0.05	0.01	0.01	0.02	6.13	7.25	8.54	1.15	24.55	3.26
2088.00	pa-bdst	50.01	0.20	0.05	0.00	0.05	6.23	7.86	10.29	1.09	23.85	3.43
2087.91	pa-bdst	50.00	0.07	0.02	0.00	0.02	5.37	6.23	7.78	1.04	22.06	3.31
2087.82	pa-bdst	50.00	0.22	0.04	0.01	0.04	5.51	6.80	9.37	0.96	22.25	3.41
2087.73	pa-bdst	50.00	0.48	0.08	0.02	0.10	5.62	6.64	9.37	1.15	21.15	3.14
2087.64	pa-bdst	50.01	1.90	0.27	0.07	0.34	4.09	5.01	8.54	0.62	20.25	3.80
2087.51	b-gst	50.00	0.03	0.00	0.01	0.01	14.57	17.46	26.14	2.25	69.09	3.71
2087.42	b-gst	50.00	0.38	0.03	0.31	0.34	8.45	9.42	9.37	1.27	49.85	3.98
2087.33	b-gst	50.01	0.10	0.01	0.05	0.06	5.84	6.08	6.45	1.10	29.75	3.50
2087.21	b-gst	50.01	0.07	0.01	0.03	0.04	5.42	5.81	7.08	1.05	25.64	3.41
2087.12	b-gst	50.01	0.12	0.02	0.01	0.03	5.12	5.81	7.78	0.86	25.69	3.65
2087.03	b-gst	50.01	0.08	0.02	0.04	0.06	5.59	6.17	7.78	0.97	27.99	3.56
2086.90	b-gst	50.00	0.06	0.01	0.03	0.04	5.20	5.64	7.78	0.99	24.86	3.38
2086.81	b-gst	50.01	0.07	0.08	0.01	0.08	5.08	5.60	7.78	0.87	26.30	3.63
2086.69	b-gst	50.00	0.05	0.01	0.02	0.03	5.26	5.67	6.17	0.99	26.01	3.45
2086.57	b-gst	50.00	0.07	0.01	0.04	0.05	5.11	5.58	7.35	0.95	24.85	3.44
2086.48	b-gst	50.01	0.11	0.04	0.00	0.04	4.97	5.49	8.54	0.91	23.68	3.44
2086.39	b-gst	50.00	0.26	0.04	0.19	0.23	6.40	6.35	21.69	1.03	44.16	4.00
2086.26	b-gst	49.56	0.17	0.05	0.02	0.07	8.00	8.45	9.37	1.21	49.66	4.05
2086.17	b-gst	50.01	0.06	0.01	0.02	0.04	7.20	7.40	15.53	1.12	46.91	4.02
2086.08	b-gst	50.00	0.05	0.02	0.00	0.02	6.99	7.45	16.77	1.04	43.70	4.08
2085.99	b-gst	50.00	0.04	0.02	0.01	0.03	6.78	7.50	18.00	0.95	40.49	4.15
2085.90	b-gst	50.00	0.06	0.01	0.00	0.01	8.41	9.28	14.28	1.12	55.07	4.32
2085.81	b-gst	50.00	0.20	0.08	0.03	0.11	5.71	6.16	7.78	1.10	26.38	3.34
2085.65	b-gst	50.01	0.19	0.05	0.08	0.13	5.37	6.17	10.29	0.89	26.11	3.61
2085.56	b-gst	50.00	0.04	0.02	0.00	0.03	5.81	6.77	13.75	0.90	29.64	3.76
2085.47	b-gst	50.01	0.05	0.02	0.00	0.03	6.25	7.38	17.20	0.91	33.17	3.90
2085.35	b-gst	50.00	0.73	0.13	0.54	0.67	4.98	4.76	2.79	0.99	27.22	3.47
2085.26	b-gst	50.00	0.17	0.03	0.11	0.14	4.54	4.43	2.54	0.93	23.73	3.38
2085.17	b-gst	50.00	0.09	0.02	0.04	0.06	8.61	9.44	26.14	1.06	61.76	4.63
2085.08	b-gst	50.00	0.09	0.04	0.01	0.05	4.89	4.91	5.35	1.11	21.92	3.10
2084.95	b-gst	50.00	0.08	0.02	0.04	0.06	7.50	8.62	14.94	1.00	46.19	4.23
2084.89	b-gst	50.01	0.08	0.03	0.02	0.06	5.38	5.89	8.54	1.01	25.46	3.42
2084.77	b-gst	50.00	0.10	0.04	0.01	0.05	4.94	5.52	7.78	0.87	23.96	3.53
2084.68	b-gst	50.00	0.11	0.04	0.01	0.05	5.35	6.11	9.37	0.98	23.64	3.40
2084.56	b-gst	50.00	0.32	0.05	0.14	0.19	3.70	4.34	8.54	0.48	22.15	4.28
2084.44	b-gst	50.00	0.07	0.02	0.02	0.04	6.25	7.62	11.29	0.93	30.67	3.77
2084.34	b-gst	50.00	0.09	0.02	0.02	0.04	6.02	7.47	10.29	0.88	29.46	3.78
2084.25	b-gst	50.00	0.42	0.12	0.03	0.15	7.57	10.19	12.40	1.01	28.68	3.71
2084.16	b-gst	50.00	0.13	0.02	0.02	0.04	5.89	7.60	11.29	0.86	26.86	3.74
2084.07	b-gst	50.00	0.21	0.02	0.01	0.03	6.80	8.89	13.61	0.99	29.28	3.70
2083.98	b-gst	50.00	0.57	0.17	0.06	0.24	4.97	6.20	10.29	0.82	21.11	3.51
2083.86	b-gst	50.01	0.16	0.09	0.01	0.10	5.17	5.90	8.54	0.96	22.28	3.42
2083.77	b-gst	50.01	0.18	0.06	0.04	0.10	5.10	5.98	8.54	0.98	20.84	3.25
2083.67	b-gst	50.00	0.16	0.06	0.04	0.10	4.32	4.73	7.08	0.83	20.11	3.38
2083.52	b-gst	50.00	0.08	0.02	0.03	0.05	6.69	7.83	9.37	1.23	27.66	3.35
2083.43	b-gst	50.00	0.19	0.05	0.02	0.07	5.40	6.62	9.37	0.92	23.11	3.47
2083.34	b-gst	50.01	0.13	0.01	0.08	0.09	6.23	7.73	10.79	1.02	26.15	3.48
2083.22	b-gst	50.00	0.88	0.03	0.02	0.05	5.29	6.36	9.37	0.90	23.22	3.50
2083.13	b-gst	50.01	0.49	0.08	0.01	0.08	5.22	6.47	9.37	0.92	20.79	3.35
2083.00	b-gst	50.00	0.45	0.05	0.00	0.05	5.95	7.27	10.29	0.99	26.04	3.51
2082.91	b-gst	50.01	0.76	0.04	0.00	0.04	5.73	7.21	11.29	0.88	25.74	3.69
2082.82	b-gst	50.01	0.03	0.01	0.01	0.02	8.50	10.38	15.67	1.18	42.41	3.77
2082.70	b-gst	50.00	0.08	0.05	0.00	0.05	5.65	6.93	9.37	0.97	23.81	3.45
2082.61	b-gst	50.00	0.07	0.02	0.00	0.03	6.42	8.14	11.29	0.94	29.07	3.75
2082.52	b-gst	50.00	0.81	0.03	0.01	0.03	7.16	8.97	11.29	1.10	31.07	3.68
2082.39	b-gst	50.01	0.97	0.02	0.01	0.03	8.67	10.69	13.61	1.23	40.60	3.93
2082.30	b-gst	50.00	1.88	0.02	0.00	0.03	6.65	8.52	11.85	0.96	29.53	3.75
2082.21	b-gst	50.01	0.02	0.01	0.00	0.01	9.31	11.56	20.73	1.33	36.43	3.35
2082.03	b-gst	50.00	0.26	0.04	0.02	0.06	8.64	10.17	13.61	1.86	31.80	3.04
2081.94	b-gst	50.00	0.26	0.07	0.05	0.11	7.23	9.73	14.94	1.07	28.05	3.54
2081.84	b-gst	50.00	0.71	0.11	0.01	0.13	7.33	10.10	14.94	1.00	30.15	3.73
2081.75	b-gst	50.00	0.60	0.08	0.00	0.08	7.36	9.93	14.94	1.12	27.52	3.51
2081.71	b-gst	50.00	0.15	0.07	0.00	0.07	6.75	9.22	13.61	0.94	27.33	3.69
2081.66	b-gst	50.01	0.12	0.07	0.01	0.08	6.88	9.30	13.61	0.99	27.34	3.63
2081.62	b-gst	50.00	0.05	0.03	0.01	0.04	9.66	13.53	19.76	1.14	39.02	3.87
2081.57	b-gst	50.01	0.28	0.08	0.01	0.09	7.93	11.29	16.40	1.01	30.78	3.75
2081.52	b-gst	50.01	0.36	0.16	0.03	0.18	7.56	10.49	16.40	1.03	30.45	3.73

2081.43	b-gst	50.01	0.23	0.07	0.02	0.09	7.36	10.28	14.94	0.99	28.79	3.69
2081.39	b-gst	50.00	0.11	0.05	0.02	0.07	9.39	12.94	18.00	1.30	35.29	3.66
2081.33	b-gst	50.01	0.21	0.06	0.01	0.08	7.32	10.15	14.94	1.03	27.92	3.63
2081.28	b-gst	50.00	0.47	0.24	0.00	0.24	7.06	9.58	14.94	1.10	25.88	3.47
2081.24	b-gst	50.01	0.91	0.27	0.05	0.31	7.27	9.79	14.94	1.05	29.75	3.63
2081.19	b-gst	50.01	0.15	0.09	0.02	0.11	6.56	9.03	13.61	0.93	26.05	3.65
2081.11	b-gst	50.00	0.47	0.12	0.03	0.16	6.22	8.24	13.61	0.97	24.43	3.49
2081.05	b-gst	50.00	0.26	0.11	0.04	0.15	5.80	7.76	12.40	0.87	23.84	3.60
2081.02	b-gst	50.00	0.20	0.09	0.02	0.11	6.46	8.58	13.61	1.03	24.46	3.44
2080.96	b-gst	50.00	0.17	0.09	0.02	0.11	6.12	7.80	11.29	1.08	22.84	3.27
2080.93	fa-gst	50.00	0.21	0.10	0.02	0.13	7.00	9.48	14.94	1.10	25.60	3.42
2080.87	fa-gst	50.00	0.18	0.09	0.04	0.12	6.20	8.31	13.01	0.98	23.34	3.44
2080.81	fa-gst	50.00	0.35	0.22	0.02	0.24	5.76	7.54	12.40	0.96	22.01	3.35
2080.76	fa-gst	50.00	0.35	0.25	0.01	0.26	6.20	8.34	13.61	0.97	23.43	3.43
2080.72	fa-gst	50.01	0.61	0.44	0.01	0.45	4.56	5.36	8.54	0.89	18.17	3.17
2080.67	fa-gst	50.00	0.68	0.55	0.02	0.56	4.88	5.46	7.78	1.11	17.99	2.93
2080.63	fa-gst	50.00	0.28	0.16	0.01	0.16	5.04	6.36	11.29	0.84	20.84	3.40
2080.56	fa-gst	50.00	0.12	0.05	0.00	0.06	5.85	7.44	14.94	0.97	23.81	3.40
2080.50	fa-gst	50.00	0.22	0.15	0.00	0.15	5.32	6.84	11.29	0.92	20.41	3.29
2080.46	fa-gst	50.00	0.17	0.13	0.00	0.13	5.69	6.14	8.54	1.04	26.27	3.53
2080.41	fa-gst	50.00	0.85	0.65	0.01	0.66	4.69	5.13	7.78	1.03	18.79	3.01
2080.35	fa-gst	50.01	0.67	0.46	0.00	0.46	6.08	7.81	14.94	1.01	24.17	3.43
2080.32	fa-gst	50.00	0.82	0.52	0.00	0.52	5.58	7.27	12.40	0.94	21.59	3.37
2080.21	fa-gst	50.01	0.77	0.56	0.01	0.57	5.33	7.05	12.40	0.87	20.59	3.40
2080.17	fa-gst	50.00	0.66	0.44	0.01	0.45	6.60	9.02	14.94	1.01	25.07	3.49
2080.12	fa-gst	50.00	0.72	0.46	0.01	0.47	6.02	8.23	14.94	0.89	24.03	3.61
2080.08	fa-gst	50.01	0.96	0.64	0.01	0.65	6.19	8.72	14.94	0.88	24.56	3.64
2080.03	fa-gst	50.01	1.85	1.12	0.04	1.17	4.96	6.60	13.61	0.71	22.52	3.81
2079.99	fa-gst	50.00	1.07	0.42	0.01	0.43	7.19	9.86	16.40	1.01	28.87	3.68
2079.92	pa-bdst	50.00	1.20	0.41	0.02	0.43	6.23	8.78	14.94	0.80	27.11	3.88
2079.86	pa-bdst	50.00	2.12	0.34	0.01	0.36	7.73	10.90	18.00	1.02	31.28	3.76
2079.82	pa-bdst	50.00	2.72	0.25	0.02	0.28	5.35	7.81	14.94	0.61	24.64	4.15
2079.77	pa-bdst	50.00	1.73	1.00	0.04	1.04	8.95	11.88	18.00	1.42	34.09	3.51
2079.71	pa-bdst	50.01	1.03	0.16	0.05	0.21	7.17	9.94	16.40	1.10	28.03	3.63
2079.67	pa-bdst	50.01	1.08	0.21	0.01	0.22	7.53	10.44	16.40	1.07	28.53	3.61
2079.59	pa-bdst	50.01	0.95	0.17	0.03	0.20	6.94	9.48	14.94	1.05	26.24	3.51
2079.54	pa-bdst	50.00	1.39	0.19	0.01	0.20	7.14	9.84	16.40	1.01	28.49	3.66
2079.50	pa-bdst	50.01	1.61	0.18	0.01	0.18	7.59	10.45	16.40	1.11	28.41	3.57
2079.45	pa-bdst	50.00	1.98	0.21	0.02	0.23	8.01	10.84	18.00	1.16	31.39	3.63
2079.41	pa-bdst	50.01	2.09	0.29	0.01	0.30	7.44	10.50	18.00	0.97	30.15	3.79
2079.32	pa-bdst	50.00	1.64	0.29	0.02	0.31	6.65	9.28	14.94	0.97	24.78	3.57
2079.25	pa-bdst	50.00	2.39	0.25	0.03	0.28	6.57	8.95	14.94	0.98	25.42	3.56
2079.21	pa-bdst	50.00	1.10	0.26	0.02	0.28	5.91	8.14	13.61	0.87	22.83	3.57
2079.16	pa-bdst	50.01	1.16	0.39	0.01	0.41	7.52	10.75	18.00	0.98	30.10	3.78
2079.10	pa-bdst	50.00	0.91	0.32	0.01	0.33	6.87	9.54	16.40	0.98	26.90	3.62
2079.04	pa-bdst	50.00	0.93	0.36	0.01	0.37	6.98	9.74	16.40	0.99	26.81	3.61
2079.01	pa-bdst	50.01	1.34	0.40	0.02	0.43	7.72	11.00	18.00	1.02	30.59	3.73

TABLE 2A.2A: Decompaction of SMF data

Depth	Facies	Current depth interval	Initial porosity	Current porosity at depth after mechanical compaction	Decompacted depth interval	Decompaction number (S*/S)	All sized SMF		Silt sized SMF	
							Raw data	Decompacted data (SMFall/D)	Raw data	Decompacted data (SMFsilt/D)
(m)		S (m)	(Φi)	(Φd)	S* (m)	D	SMFall (wt%)	SMF*all (wt%)	SMFsilt (wt%)	SMF*silt (wt%)
2106.05	b-gst	0.12	44.50	28.93	0.16	1.28	0.242	0.189	0.208	0.162
2105.92	b-gst	0.06	44.50	28.93	0.08	1.28	0.187	0.146	0.158	0.124
2105.86	b-gst	0.05	44.50	28.93	0.06	1.28	0.203	0.159	0.170	0.132
2105.82	b-gst	0.05	44.50	28.93	0.06	1.28	0.286	0.223	0.228	0.178
2105.77	b-gst	0.05	44.50	28.93	0.06	1.28	0.259	0.202	0.213	0.167
2105.73	b-gst	0.05	44.50	28.93	0.06	1.28	0.240	0.187	0.197	0.154
2105.68	b-gst	0.06	44.50	28.93	0.08	1.28	0.326	0.255	0.162	0.126
2105.62	b-gst	0.21	44.50	28.93	0.27	1.28	0.295	0.231	0.138	0.108
2105.41	b-pkst	0.09	54.70	28.93	0.14	1.57	0.296	0.189	0.133	0.085
2105.31	b-pkst	0.03	54.70	28.93	0.05	1.57	0.756	0.482	0.454	0.289
2105.28	b-pkst	0.06	54.70	28.93	0.10	1.57	0.399	0.254	0.263	0.168
2105.22	fa-gst	0.05	44.50	28.93	0.06	1.28	0.245	0.192	0.198	0.155
2105.18	fa-gst	0.05	44.50	28.93	0.06	1.28	0.474	0.370	0.204	0.159
2105.13	fa-gst	0.06	44.50	28.93	0.08	1.28	0.710	0.554	0.170	0.133
2105.07	fa-gst	0.06	44.50	28.93	0.08	1.28	2.485	1.941	0.245	0.192
2105.01	fa-gst	0.03	44.50	28.93	0.04	1.28	0.685	0.535	0.428	0.334
2104.98	fa-gst	0.05	44.50	28.93	0.06	1.28	0.685	0.535	0.363	0.284
2104.93	fa-gst	0.05	44.50	28.93	0.06	1.28	0.895	0.699	0.534	0.417
2104.88	fa-gst	0.05	44.50	28.93	0.06	1.28	0.857	0.669	0.413	0.323
2104.83	fa-gst	0.07	44.50	28.94	0.09	1.28	0.297	0.232	0.225	0.176
2104.77	fa-gst	0.03	44.50	28.94	0.04	1.28	0.936	0.731	0.420	0.328
2104.74	fa-gst	0.05	44.50	28.94	0.06	1.28	0.787	0.615	0.439	0.343
2104.69	mdrk	0.02	70.00	28.94	0.06	2.37	88.900	37.529	nd	nd
2104.67	mdrk	0.02	70.00	28.94	0.06	2.37	87.868	37.094	nd	nd
2104.64	mdrk	0.02	70.00	28.94	0.06	2.37	92.416	39.014	nd	nd
2104.62	mdrk	0.02	70.00	28.94	0.06	2.37	nd	38.061	nd	nd
2104.60	mdrk	0.02	70.00	28.94	0.06	2.37	87.900	37.108	nd	nd
2104.57	mdrk	0.02	70.00	28.94	0.06	2.37	91.261	38.526	nd	nd
2104.55	mdrk	0.02	70.00	28.94	0.06	2.37	81.890	34.571	nd	nd
2104.53	mdrk	0.02	70.00	28.94	0.06	2.37	92.836	39.191	nd	nd
2104.50	mdrk	0.02	70.00	28.94	0.06	2.37	89.026	37.583	nd	nd
2104.48	mdrk	0.02	70.00	28.94	0.06	2.37	90.039	38.011	nd	nd
2104.46	mdrk	0.02	70.00	28.94	0.06	2.37	89.686	37.862	nd	nd
2104.43	mdrk	0.02	70.00	28.94	0.06	2.37	87.713	37.029	nd	nd
2104.41	mdrk	0.02	70.00	28.94	0.06	2.37	89.757	37.892	nd	nd
2104.39	mdrk	0.02	70.00	28.94	0.06	2.37	nd	38.581	nd	nd

2104.36	mdrk	0.02	70.00	28.94	0.06	2.37	93.024	39.271	nd	nd
2104.34	mdrk	0.05	70.00	28.94	0.11	2.37	91.743	38.731	nd	nd
2104.29	fa-gst	0.05	44.50	28.94	0.06	1.28	3.640	2.843	3.605	2.815
2104.25	fa-gst	0.05	44.50	28.94	0.06	1.28	6.689	5.224	6.662	5.203
2104.20	fu-pkst	0.05	54.70	28.94	0.07	1.57	2.131	1.359	2.104	1.341
2104.16	fu-pkst	0.06	54.70	28.94	0.10	1.57	1.159	0.739	1.143	0.729
2104.10	fu-pkst	0.03	54.70	28.94	0.05	1.57	0.808	0.515	0.723	0.461
2104.06	fu-pkst	0.08	54.70	28.94	0.12	1.57	0.913	0.582	0.881	0.562
2103.99	fu-pkst	0.05	54.70	28.94	0.07	1.57	1.088	0.694	0.999	0.637
2103.94	fu-pkst	0.08	54.70	28.94	0.12	1.57	1.306	0.832	1.267	0.807
2103.87	fu-pkst	0.05	54.70	28.94	0.07	1.57	0.625	0.399	0.555	0.354
2103.82	fu-pkst	0.06	54.70	28.94	0.10	1.57	0.444	0.283	0.425	0.271
2103.76	fu-pkst	0.03	54.70	28.94	0.05	1.57	0.688	0.439	0.574	0.366
2103.73	fu-pkst	0.05	54.70	28.94	0.07	1.57	0.826	0.526	0.805	0.513
2103.68	b-pkst	0.05	54.70	28.94	0.07	1.57	0.804	0.512	0.752	0.479
2103.64	b-pkst	0.06	54.70	28.94	0.10	1.57	0.734	0.468	0.715	0.456
2103.58	b-pkst	0.03	54.70	28.94	0.05	1.57	1.071	0.683	0.937	0.597
2103.55	b-pkst	0.09	54.70	28.94	0.14	1.57	0.669	0.427	0.653	0.417
2103.46	b-pkst	0.06	54.70	28.94	0.10	1.57	0.821	0.523	0.801	0.510
2103.39	b-pkst	0.05	54.70	28.94	0.07	1.57	0.685	0.437	0.646	0.412
2103.35	b-pkst	0.05	54.70	28.94	0.07	1.57	0.948	0.604	0.922	0.588
2103.30	b-pkst	0.06	54.70	28.94	0.10	1.57	0.943	0.601	0.859	0.548
2103.24	b-pkst	0.05	54.70	28.94	0.07	1.57	1.027	0.655	1.001	0.638
2103.20	b-pkst	0.08	54.70	28.94	0.12	1.57	1.022	0.652	0.931	0.593
2103.12	b-pkst	0.06	54.70	28.94	0.10	1.57	1.142	0.728	1.122	0.716
2103.06	b-pkst	0.06	54.70	28.94	0.10	1.57	0.709	0.452	0.628	0.400
2103.00	b-pkst	0.06	54.70	28.94	0.10	1.57	1.339	0.854	1.307	0.833
2102.94	b-pkst	0.03	54.70	28.94	0.05	1.57	0.936	0.597	0.859	0.548
2102.91	b-pkst	0.06	54.70	28.94	0.10	1.57	1.148	0.732	1.113	0.710
2102.85	b-pkst	0.18	54.70	28.94	0.29	1.57	1.076	0.686	1.040	0.663
2102.66	b-pkst	0.12	54.70	28.94	0.19	1.57	1.043	0.665	1.014	0.647
2102.54	b-pkst	0.08	54.70	28.95	0.12	1.57	0.503	0.320	0.493	0.314
2102.46	b-pkst	0.11	54.70	28.95	0.17	1.57	0.581	0.370	0.567	0.361
2102.36	b-pkst	0.09	54.70	28.95	0.14	1.57	0.611	0.390	0.518	0.330
2102.27	b-pkst	0.14	54.70	28.95	0.22	1.57	0.687	0.438	0.606	0.386
2102.13	b-pkst	0.11	54.70	28.95	0.17	1.57	0.651	0.415	0.564	0.359
2102.02	b-pkst	0.11	54.70	28.95	0.17	1.57	0.496	0.316	0.440	0.281
2101.92	b-pkst	0.11	54.70	28.95	0.17	1.57	0.458	0.292	0.375	0.239
2101.81	b-pkst	0.09	54.70	28.95	0.14	1.57	0.154	0.098	0.129	0.082
2101.72	b-pkst	0.09	54.70	28.95	0.14	1.57	1.030	0.657	0.923	0.589
2101.63	b-pkst	0.12	54.70	28.95	0.19	1.57	0.380	0.242	0.323	0.206

2101.50	b-pkst	0.09	54.70	28.95	0.14	1.57	0.425	0.271	0.371	0.237
2101.41	b-pkst	0.09	54.70	28.95	0.14	1.57	1.105	0.705	0.957	0.610
2101.32	b-pkst	0.12	54.70	28.95	0.19	1.57	1.781	1.135	1.549	0.988
2101.20	b-pkst	0.09	54.70	28.95	0.14	1.57	0.332	0.212	0.260	0.166
2101.11	b-pkst	0.15	54.70	28.95	0.24	1.57	1.244	0.793	1.092	0.696
2100.96	b-pkst	0.09	54.70	28.95	0.14	1.57	0.406	0.259	0.352	0.224
2100.86	b-wkst	0.11	70.00	28.95	0.25	2.37	0.114	0.048	0.097	0.041
2100.76	b-wkst	0.15	70.00	28.95	0.36	2.37	0.463	0.195	0.405	0.171
2100.61	b-wkst	0.08	70.00	28.95	0.18	2.37	1.270	0.536	1.051	0.444
2100.53	b-wkst	0.12	70.00	28.95	0.29	2.37	0.136	0.058	0.118	0.050
2100.41	pa-bdst	0.12	44.50	28.95	0.16	1.28	0.133	0.104	0.120	0.094
2100.29	pa-bdst	0.12	44.50	28.96	0.16	1.28	0.090	0.071	0.076	0.059
2100.16	b-wkst	0.09	70.00	28.96	0.22	2.37	0.108	0.045	0.094	0.040
2100.07	b-wkst	0.15	70.00	28.96	0.36	2.37	0.118	0.050	0.099	0.042
2099.92	b-wkst	0.12	70.00	28.96	0.29	2.37	0.066	0.028	0.050	0.021
2099.80	b-wkst	0.12	70.00	28.96	0.29	2.37	1.447	0.611	1.432	0.605
2099.68	b-wkst	0.09	70.00	28.96	0.22	2.37	0.105	0.044	0.089	0.038
2099.58	b-wkst	0.09	70.00	28.96	0.22	2.37	0.091	0.038	0.080	0.034
2099.49	b-wkst	0.12	70.00	28.96	0.29	2.37	0.084	0.035	0.067	0.028
2099.37	b-wkst	0.12	70.00	28.96	0.29	2.37	0.115	0.048	0.104	0.044
2099.25	b-wkst	0.18	70.00	28.96	0.43	2.37	0.204	0.086	0.170	0.072
2099.07	b-wkst	0.09	70.00	28.96	0.22	2.37	0.268	0.113	0.228	0.096
2098.97	b-wkst	0.09	70.00	28.96	0.22	2.37	1.056	0.446	0.786	0.332
2098.88	b-wkst	0.14	70.00	28.96	0.32	2.37	0.248	0.105	0.200	0.085
2098.75	b-wkst	0.11	70.00	28.96	0.25	2.37	0.180	0.076	0.151	0.064
2098.64	b-wkst	0.09	70.00	28.96	0.22	2.37	0.154	0.065	0.117	0.049
2098.55	b-wkst	0.05	70.00	28.96	0.11	2.37	0.103	0.044	0.080	0.034
2098.50	b-wkst	0.17	70.00	28.96	0.40	2.37	0.102	0.043	0.080	0.034
2098.33	b-wkst	0.15	70.00	28.96	0.36	2.37	0.082	0.035	0.065	0.028
2098.18	b-wkst	0.09	70.00	28.96	0.22	2.37	0.057	0.024	0.046	0.019
2098.09	b-wkst	0.09	70.00	28.97	0.22	2.37	0.112	0.047	0.105	0.044
2098.00	b-wkst	0.15	70.00	28.97	0.36	2.37	0.099	0.042	0.095	0.040
2097.85	b-wkst	0.09	70.00	28.97	0.22	2.37	0.079	0.034	0.074	0.031
2097.76	b-wkst	0.09	70.00	28.97	0.22	2.37	0.064	0.027	0.050	0.021
2097.66	b-	0.12	70.00	28.97	0.29	2.37	0.077	0.033	0.067	0.028

	wkst									
2097.54	b-wkst	0.09	70.00	28.97	0.22	2.37	0.054	0.023	0.043	0.018
2097.45	b-wkst	0.09	70.00	28.97	0.22	2.37	0.045	0.019	0.037	0.016
2097.36	b-wkst	0.11	70.00	28.97	0.25	2.37	0.078	0.033	0.062	0.026
2097.25	b-wkst	0.11	70.00	28.97	0.25	2.37	0.095	0.040	0.073	0.031
2097.15	b-wkst	0.09	70.00	28.97	0.22	2.37	0.063	0.027	0.056	0.024
2097.05	b-wkst	0.12	70.00	28.97	0.29	2.37	0.091	0.038	0.083	0.035
2096.93	b-wkst	0.09	70.00	28.97	0.22	2.37	0.064	0.027	0.047	0.020
2096.84	b-wkst	0.12	70.00	28.97	0.29	2.37	0.130	0.055	0.101	0.043
2096.72	b-pkst	0.09	54.70	28.97	0.14	1.57	0.061	0.039	0.052	0.033
2096.63	b-pkst	0.11	54.70	28.97	0.17	1.57	0.058	0.037	0.048	0.031
2096.52	b-pkst	0.14	54.70	28.97	0.22	1.57	0.442	0.282	0.051	0.032
2096.38	b-pkst	0.09	54.70	28.97	0.14	1.57	0.027	0.017	0.013	0.008
2096.29	b-pkst	0.09	54.70	28.97	0.14	1.57	0.068	0.044	0.045	0.029
2096.20	b-wkst	0.12	70.00	28.97	0.29	2.37	0.054	0.023	0.034	0.014
2096.08	b-wkst	0.09	70.00	28.97	0.22	2.37	0.025	0.011	0.015	0.006
2095.99	b-wkst	0.12	70.00	28.97	0.29	2.37	0.032	0.014	0.025	0.011
2095.87	b-wkst	0.14	70.00	28.98	0.32	2.37	0.063	0.027	0.037	0.016
2095.73	b-wkst	0.11	70.00	28.98	0.25	2.37	0.028	0.012	0.017	0.007
2095.62	b-wkst	0.09	70.00	28.98	0.22	2.37	0.057	0.024	0.020	0.009
2095.53	b-wkst	0.11	70.00	28.98	0.25	2.37	0.044	0.018	0.026	0.011
2095.42	b-wkst	0.11	70.00	28.98	0.25	2.37	0.025	0.010	0.024	0.010
2095.32	b-wkst	0.09	70.00	28.98	0.22	2.37	0.042	0.018	0.029	0.012
2095.23	b-wkst	0.12	70.00	28.98	0.29	2.37	0.031	0.013	0.020	0.009
2095.10	b-wkst	0.11	70.00	28.98	0.25	2.37	0.064	0.027	0.060	0.025
2095.00	b-wkst	0.11	70.00	28.98	0.25	2.37	0.089	0.038	0.079	0.033
2094.89	b-wkst	0.09	70.00	28.98	0.22	2.37	0.039	0.017	0.028	0.012
2094.80	b-wkst	0.12	70.00	28.98	0.29	2.37	0.035	0.015	0.023	0.010
2094.68	b-wkst	0.12	70.00	28.98	0.29	2.37	0.101	0.042	0.090	0.038
2094.56	b-wkst	0.12	70.00	28.98	0.29	2.37	0.019	0.008	0.013	0.005
2094.43	b-wkst	0.09	70.00	28.98	0.22	2.37	0.085	0.036	0.075	0.031
2094.34	b-wkst	0.15	70.00	28.98	0.36	2.37	0.089	0.038	0.077	0.032
2094.19	b-wkst	0.09	70.00	28.98	0.22	2.37	0.038	0.016	0.028	0.012
2094.10	b-wkst	0.12	70.00	28.98	0.29	2.37	0.112	0.047	0.100	0.042
2093.98	b-wkst	0.09	70.00	28.98	0.22	2.37	0.078	0.033	0.070	0.029
2093.88	b-wkst	0.12	70.00	28.98	0.29	2.37	0.115	0.049	0.065	0.027

2093.76	b-wkst	0.12	70.00	28.98	0.29	2.37	0.124	0.052	0.105	0.044
2093.64	b-wkst	0.17	70.00	28.99	0.40	2.37	0.057	0.024	0.046	0.019
2093.47	b-wkst	0.08	70.00	28.99	0.18	2.37	0.055	0.023	0.034	0.014
2093.40	b-wkst	0.12	70.00	28.99	0.29	2.37	0.152	0.064	0.078	0.033
2093.27	b-wkst	0.09	70.00	28.99	0.22	2.37	0.080	0.034	0.071	0.030
2093.18	b-wkst	0.21	70.00	28.99	0.51	2.37	0.029	0.012	0.026	0.011
2092.97	b-wkst	0.09	70.00	28.99	0.22	2.37	0.072	0.031	0.044	0.018
2092.88	b-wkst	0.12	70.00	28.99	0.29	2.37	0.015	0.007	0.015	0.006
2092.76	b-wkst	0.09	70.00	28.99	0.22	2.37	0.296	0.125	0.037	0.015
2092.67	b-wkst	0.09	70.00	28.99	0.22	2.37	0.052	0.022	0.048	0.020
2092.57	b-wkst	0.09	70.00	28.99	0.22	2.37	0.094	0.040	0.089	0.037
2092.48	b-wkst	0.09	70.00	28.99	0.22	2.37	0.108	0.046	0.095	0.040
2092.39	b-wkst	0.09	70.00	28.99	0.22	2.37	0.037	0.016	0.031	0.013
2092.30	b-wkst	0.18	70.00	28.99	0.43	2.37	0.018	0.007	0.018	0.007
2092.12	b-pkst	0.09	54.70	28.99	0.14	1.57	0.029	0.019	0.029	0.018
2092.03	b-pkst	0.09	54.70	28.99	0.14	1.57	0.185	0.118	0.136	0.087
2091.93	b-gst	0.09	44.50	28.99	0.12	1.28	0.305	0.238	0.140	0.110
2091.84	b-gst	0.11	44.50	28.99	0.14	1.28	0.107	0.084	0.074	0.058
2091.74	b-gst	0.11	44.50	28.99	0.14	1.28	0.069	0.054	0.058	0.045
2091.63	b-gst	0.09	44.50	28.99	0.12	1.28	0.096	0.075	0.082	0.064
2091.54	b-gst	0.09	44.50	28.99	0.12	1.28	0.168	0.131	0.167	0.131
2091.45	pa-bdst	0.11	44.50	28.99	0.14	1.28	0.130	0.101	0.083	0.065
2091.34	pa-bdst	0.11	44.50	29.00	0.14	1.28	0.138	0.108	0.136	0.107
2091.23	pa-bdst	0.09	44.50	29.00	0.12	1.28	0.084	0.066	0.083	0.065
2091.14	pa-bdst	0.11	44.50	29.00	0.14	1.28	0.075	0.058	0.066	0.052
2091.03	pa-bdst	0.11	44.50	29.00	0.14	1.28	0.086	0.068	0.069	0.054
2090.93	pa-bdst	0.09	44.50	29.00	0.12	1.28	0.252	0.197	0.085	0.067
2090.84	pa-bdst	0.12	44.50	29.00	0.16	1.28	0.081	0.063	0.052	0.041
2090.71	pa-bdst	0.09	44.50	29.00	0.12	1.28	0.108	0.084	0.081	0.064
2090.62	pa-bdst	0.09	44.50	29.00	0.12	1.28	0.036	0.028	0.036	0.028
2090.53	pa-bdst	0.12	44.50	29.00	0.16	1.28	0.056	0.044	0.055	0.043
2090.41	pa-bdst	0.09	44.50	29.00	0.12	1.28	0.059	0.046	0.056	0.044
2090.32	pa-bdst	0.09	44.50	29.00	0.12	1.28	0.376	0.294	0.092	0.072
2090.23	pa-bdst	0.09	44.50	29.00	0.12	1.28	0.407	0.318	0.076	0.060
2090.14	b-pkst	0.15	54.70	29.00	0.24	1.57	0.101	0.065	0.043	0.027
2089.98	b-pkst	0.11	54.70	29.00	0.17	1.57	0.063	0.040	0.058	0.037
2089.88	b-pkst	0.11	54.70	29.00	0.17	1.57	0.166	0.106	0.079	0.050

2089.77	b-pkst	0.11	54.70	29.00	0.17	1.57	0.178	0.113	0.053	0.034
2089.66	b-pkst	0.11	54.70	29.00	0.17	1.57	0.087	0.055	0.042	0.027
2089.56	b-pkst	0.11	54.70	29.00	0.17	1.57	0.197	0.126	0.062	0.039
2089.45	b-pkst	0.14	54.70	29.00	0.21	1.57	0.031	0.020	0.028	0.018
2089.31	b-pkst	0.09	54.70	29.00	0.14	1.57	0.025	0.016	0.022	0.014
2089.22	b-pkst	0.09	54.70	29.00	0.14	1.57	0.062	0.039	0.057	0.037
2089.13	b-pkst	0.09	54.70	29.01	0.14	1.57	0.050	0.032	0.031	0.020
2089.04	b-pkst	0.09	54.70	29.01	0.14	1.57	0.145	0.093	0.049	0.032
2088.95	pa-bdst	0.09	44.50	29.01	0.12	1.28	0.283	0.221	0.066	0.052
2088.86	pa-bdst	0.12	44.50	29.01	0.16	1.28	0.080	0.062	0.064	0.050
2088.73	pa-bdst	0.09	44.50	29.01	0.12	1.28	0.035	0.027	0.017	0.013
2088.64	pa-bdst	0.09	44.50	29.01	0.12	1.28	1.454	1.137	0.077	0.060
2088.55	pa-bdst	0.15	44.50	29.01	0.19	1.28	0.054	0.043	0.034	0.027
2088.40	pa-bdst	0.09	44.50	29.01	0.12	1.28	0.080	0.062	0.061	0.048
2088.31	pa-bdst	0.09	44.50	29.01	0.12	1.28	0.142	0.111	0.129	0.101
2088.22	pa-bdst	0.12	44.50	29.01	0.16	1.28	0.104	0.082	0.024	0.019
2088.09	pa-bdst	0.09	44.50	29.01	0.12	1.28	0.019	0.015	0.014	0.011
2088.00	pa-bdst	0.09	44.50	29.01	0.12	1.28	0.049	0.038	0.048	0.038
2087.91	pa-bdst	0.09	44.50	29.01	0.12	1.28	0.024	0.019	0.022	0.017
2087.82	pa-bdst	0.09	44.50	29.01	0.12	1.28	0.044	0.034	0.037	0.029
2087.73	pa-bdst	0.09	44.50	29.01	0.12	1.28	0.098	0.076	0.079	0.062
2087.64	pa-bdst	0.12	44.50	29.01	0.16	1.28	0.339	0.265	0.272	0.213
2087.51	b-gst	0.09	44.50	29.01	0.12	1.28	0.011	0.008	0.004	0.003
2087.42	b-gst	0.09	44.50	29.01	0.12	1.28	0.337	0.263	0.030	0.023
2087.33	b-gst	0.12	44.50	29.01	0.16	1.28	0.063	0.049	0.013	0.010
2087.21	b-gst	0.09	44.50	29.01	0.12	1.28	0.043	0.034	0.011	0.008
2087.12	b-gst	0.09	44.50	29.01	0.12	1.28	0.030	0.023	0.021	0.016
2087.03	b-gst	0.12	44.50	29.01	0.16	1.28	0.058	0.046	0.016	0.012
2086.90	b-gst	0.09	44.50	29.02	0.12	1.28	0.039	0.030	0.012	0.010
2086.81	b-gst	0.12	44.50	29.02	0.16	1.28	0.085	0.066	0.079	0.062
2086.69	b-gst	0.12	44.50	29.02	0.16	1.28	0.032	0.025	0.009	0.007
2086.57	b-gst	0.09	44.50	29.02	0.12	1.28	0.048	0.038	0.013	0.010
2086.48	b-gst	0.09	44.50	29.02	0.12	1.28	0.039	0.030	0.038	0.030
2086.39	b-gst	0.12	44.50	29.02	0.16	1.28	0.230	0.180	0.043	0.034
2086.26	b-gst	0.09	44.50	29.02	0.12	1.28	0.072	0.056	0.050	0.039
2086.17	b-gst	0.09	44.50	29.02	0.12	1.28	0.036	0.029	0.012	0.009
2086.08	b-gst	0.09	44.50	29.02	0.12	1.28	0.018	0.014	0.018	0.014
2085.99	b-gst	0.09	44.50	29.02	0.12	1.28	0.026	0.020	0.018	0.014
2085.90	b-gst	0.09	44.50	29.02	0.12	1.28	0.014	0.011	0.012	0.009
2085.81	b-gst	0.15	44.50	29.02	0.19	1.28	0.109	0.085	0.079	0.062

2085.65	b-gst	0.09	44.50	29.02	0.12	1.28	0.129	0.101	0.053	0.042
2085.56	b-gst	0.09	44.50	29.02	0.12	1.28	0.026	0.020	0.022	0.018
2085.47	b-gst	0.12	44.50	29.02	0.16	1.28	0.026	0.021	0.025	0.019
2085.35	b-gst	0.09	44.50	29.02	0.12	1.28	0.665	0.520	0.127	0.099
2085.26	b-gst	0.09	44.50	29.02	0.12	1.28	0.137	0.107	0.030	0.024
2085.17	b-gst	0.09	44.50	29.02	0.12	1.28	0.062	0.049	0.021	0.017
2085.08	b-gst	0.12	44.50	29.02	0.16	1.28	0.049	0.039	0.039	0.030
2084.95	b-gst	0.06	44.50	29.02	0.08	1.28	0.057	0.045	0.017	0.013
2084.89	b-gst	0.12	44.50	29.02	0.16	1.28	0.058	0.046	0.033	0.026
2084.77	b-gst	0.09	44.50	29.02	0.12	1.28	0.050	0.039	0.040	0.031
2084.68	b-gst	0.12	44.50	29.03	0.16	1.28	0.053	0.042	0.045	0.035
2084.56	b-gst	0.12	44.50	29.03	0.16	1.28	0.186	0.146	0.047	0.037
2084.44	b-gst	0.09	44.50	29.03	0.12	1.28	0.037	0.029	0.020	0.016
2084.34	b-gst	0.09	44.50	29.03	0.12	1.28	0.039	0.030	0.020	0.015
2084.25	b-gst	0.09	44.50	29.03	0.12	1.28	0.147	0.115	0.118	0.093
2084.16	b-gst	0.09	44.50	29.03	0.12	1.28	0.041	0.032	0.025	0.019
2084.07	b-gst	0.09	44.50	29.03	0.12	1.28	0.035	0.027	0.024	0.019
2083.98	b-gst	0.12	44.50	29.03	0.16	1.28	0.239	0.187	0.175	0.137
2083.86	b-gst	0.09	44.50	29.03	0.12	1.28	0.097	0.076	0.086	0.067
2083.77	b-gst	0.09	44.50	29.03	0.12	1.28	0.099	0.077	0.063	0.049
2083.67	b-gst	0.15	44.50	29.03	0.19	1.28	0.098	0.077	0.063	0.049
2083.52	b-gst	0.09	44.50	29.03	0.12	1.28	0.049	0.039	0.015	0.012
2083.43	b-gst	0.09	44.50	29.03	0.12	1.28	0.069	0.054	0.049	0.038
2083.34	b-gst	0.12	44.50	29.03	0.16	1.28	0.090	0.070	0.015	0.012
2083.22	b-gst	0.09	44.50	29.03	0.12	1.28	0.053	0.041	0.028	0.022
2083.13	b-gst	0.12	44.50	29.03	0.16	1.28	0.082	0.064	0.076	0.059
2083.00	b-gst	0.09	44.50	29.03	0.12	1.28	0.055	0.043	0.053	0.042
2082.91	b-gst	0.09	44.50	29.03	0.12	1.28	0.045	0.035	0.041	0.032
2082.82	b-gst	0.12	44.50	29.03	0.16	1.28	0.018	0.014	0.006	0.005
2082.70	b-gst	0.09	44.50	29.03	0.12	1.28	0.052	0.041	0.050	0.039
2082.61	b-gst	0.09	44.50	29.03	0.12	1.28	0.028	0.022	0.024	0.019
2082.52	b-gst	0.12	44.50	29.03	0.16	1.28	0.033	0.026	0.027	0.021
2082.39	b-gst	0.09	44.50	29.04	0.12	1.28	0.030	0.023	0.024	0.019
2082.30	b-gst	0.09	44.50	29.04	0.12	1.28	0.027	0.021	0.024	0.019
2082.21	b-gst	0.18	44.50	29.04	0.23	1.28	0.009	0.007	0.007	0.005
2082.03	b-gst	0.09	44.50	29.04	0.12	1.28	0.063	0.049	0.041	0.032
2081.94	b-gst	0.09	44.50	29.04	0.12	1.28	0.114	0.089	0.066	0.052
2081.84	b-gst	0.09	44.50	29.04	0.12	1.28	0.128	0.100	0.113	0.089
2081.75	b-gst	0.05	44.50	29.04	0.06	1.28	0.082	0.064	0.081	0.063
2081.71	b-gst	0.05	44.50	29.04	0.06	1.28	0.075	0.058	0.070	0.055
2081.66	b-gst	0.05	44.50	29.04	0.06	1.28	0.078	0.061	0.067	0.052
2081.62	b-gst	0.05	44.50	29.04	0.06	1.28	0.036	0.028	0.026	0.020
2081.57	b-gst	0.05	44.50	29.04	0.06	1.28	0.093	0.073	0.082	0.064

2081.52	b-gst	0.09	44.50	29.04	0.12	1.28	0.185	0.144	0.159	0.124
2081.43	b-gst	0.05	44.50	29.04	0.06	1.28	0.090	0.070	0.073	0.057
2081.39	b-gst	0.06	44.50	29.04	0.08	1.28	0.075	0.059	0.055	0.043
2081.33	b-gst	0.05	44.50	29.04	0.06	1.28	0.075	0.059	0.063	0.049
2081.28	b-gst	0.05	44.50	29.04	0.06	1.28	0.240	0.188	0.236	0.185
2081.24	b-gst	0.05	44.50	29.04	0.06	1.28	0.312	0.244	0.266	0.208
2081.19	b-gst	0.08	44.50	29.04	0.10	1.28	0.109	0.085	0.091	0.071
2081.11	b-gst	0.06	44.50	29.04	0.08	1.28	0.157	0.123	0.123	0.096
2081.05	b-gst	0.03	44.50	29.04	0.04	1.28	0.149	0.117	0.106	0.083
2081.02	b-gst	0.06	44.50	29.04	0.08	1.28	0.114	0.089	0.092	0.072
2080.96	b-gst	0.03	44.50	29.04	0.04	1.28	0.114	0.089	0.094	0.074
2080.93	fa-gst	0.06	44.50	29.04	0.08	1.28	0.128	0.100	0.104	0.082
2080.87	fa-gst	0.06	44.50	29.04	0.08	1.28	0.123	0.096	0.085	0.067
2080.81	fa-gst	0.05	44.50	29.04	0.06	1.28	0.241	0.189	0.221	0.173
2080.76	fa-gst	0.05	44.50	29.04	0.06	1.28	0.260	0.203	0.249	0.195
2080.72	fa-gst	0.05	44.50	29.04	0.06	1.28	0.451	0.353	0.437	0.342
2080.67	fa-gst	0.05	44.50	29.04	0.06	1.28	0.563	0.441	0.545	0.426
2080.63	fa-gst	0.06	44.50	29.04	0.08	1.28	0.161	0.126	0.156	0.122
2080.56	fa-gst	0.06	44.50	29.04	0.08	1.28	0.055	0.043	0.052	0.040
2080.50	fa-gst	0.05	44.50	29.04	0.06	1.28	0.152	0.119	0.147	0.115
2080.46	fa-gst	0.05	44.50	29.04	0.06	1.28	0.126	0.099	0.126	0.098
2080.41	fa-gst	0.06	44.50	29.04	0.08	1.28	0.658	0.515	0.649	0.508
2080.35	fa-gst	0.03	44.50	29.04	0.04	1.28	0.461	0.360	0.459	0.359
2080.32	fa-gst	0.11	44.50	29.04	0.14	1.28	0.521	0.408	0.517	0.404
2080.21	fa-gst	0.05	44.50	29.05	0.06	1.28	0.565	0.442	0.558	0.436
2080.17	fa-gst	0.05	44.50	29.05	0.06	1.28	0.449	0.351	0.441	0.345
2080.12	fa-gst	0.05	44.50	29.05	0.06	1.28	0.472	0.369	0.464	0.363
2080.08	fa-gst	0.05	44.50	29.05	0.06	1.28	0.647	0.506	0.639	0.499
2080.03	fa-gst	0.05	44.50	29.05	0.06	1.28	1.165	0.911	1.120	0.876
2079.99	fa-gst	0.06	44.50	29.05	0.08	1.28	0.427	0.334	0.421	0.330
2079.92	pa-bdst	0.06	44.50	29.05	0.08	1.28	0.427	0.334	0.407	0.318
2079.86	pa-bdst	0.05	44.50	29.05	0.06	1.28	0.357	0.280	0.344	0.269
2079.82	pa-bdst	0.05	44.50	29.05	0.06	1.28	0.278	0.218	0.254	0.199
2079.77	pa-bdst	0.06	44.50	29.05	0.08	1.28	1.036	0.810	0.997	0.780
2079.71	pa-bdst	0.05	44.50	29.05	0.06	1.28	0.213	0.167	0.165	0.129
2079.67	pa-bdst	0.08	44.50	29.05	0.10	1.28	0.219	0.171	0.206	0.161
2079.59	pa-bdst	0.05	44.50	29.05	0.06	1.28	0.197	0.154	0.169	0.133
2079.54	pa-bdst	0.05	44.50	29.05	0.06	1.28	0.199	0.155	0.189	0.148
2079.50	pa-bdst	0.05	44.50	29.05	0.06	1.28	0.185	0.144	0.178	0.139
2079.45	pa-bdst	0.05	44.50	29.05	0.06	1.28	0.229	0.179	0.206	0.161
2079.41	pa-bdst	0.09	44.50	29.05	0.12	1.28	0.303	0.237	0.288	0.225

2079.32	pa-bdst	0.06	44.50	29.05	0.08	1.28	0.306	0.240	0.288	0.226
2079.25	pa-bdst	0.05	44.50	29.05	0.06	1.28	0.276	0.216	0.251	0.196
2079.21	pa-bdst	0.05	44.50	29.05	0.06	1.28	0.281	0.220	0.258	0.202
2079.16	pa-bdst	0.06	44.50	29.05	0.08	1.28	0.405	0.317	0.392	0.306
2079.10	pa-bdst	0.06	44.50	29.05	0.08	1.28	0.331	0.259	0.322	0.252
2079.04	pa-bdst	0.03	44.50	29.05	0.04	1.28	0.370	0.290	0.363	0.284
2079.01	pa-bdst	0.03	44.50	29.05	0.04	1.28	0.425	0.333	0.401	0.313

TABLE 2A.2B: Initial porosity applied in Decompaction algorithm

Facies	Initial Porosity
Bioclastic grainstone	44.5*
Foram/algal grainstone	44.5*
Bioclastic packstone	54.7*
Fusulinid packstone	54.7*
Bioclastic wackstone	70*
Phylloid algal boundstone	30[†]
Gray-greenish mudstone	70[§]

* Goldhammer (1997)

[†] Initial porosity for Phylloid algal boundstone samples are aproximated to be equivalent to grainstone

[§] Initial porosity for mudstone samples are aproximated to be equivalent to wackstone

TABLE 2A.3.— Trace Element

Depth (m)	Ba (ppm)	Be (ppm)	Cd (ppm)	Ce (ppm)	Co (ppm)	Cu (ppm)	La (ppm)	Mn (ppm)	Mo (ppm)	Nb (ppm)	Ni (ppm)	P (ppm)	Pb (ppm)	Rb (ppm)	Sc (ppm)	Se (ppm)	Sr (ppm)	U (ppm)	V (ppm)	Y (ppm)	Zn (ppm)
2106.05	<10	<0.05	0.28	3.84	0.7	2.8	2.6	103	0.35	0.1	<0.2	70	0.8	0.3	0.2	2	344	0.6	1	6.5	6
2105.28	<10	0.07	0.15	4.97	0.6	3.6	3	119	0.27	0.1	<0.2	20	2	0.3	0.2	2	447	0.6	<1	6.5	3
2104.88	10	0.06	0.2	4.43	0.6	2.6	3	131	0.15	0.1	1.3	20	1.6	<0.1	0.2	2	393	0.5	<1	6.3	3
2104.77	10	<0.05	0.23	6.89	0.9	2.2	3.3	100	0.11	0.1	<0.2	40	2.3	0.3	0.2	2	449	0.7	1	7.5	3
2104.69	280	3.11	<0.02	31	14.3	32.5	14.8	44	0.35	17.7	49.1	170	22.9	164	18.8	2	68.6	2.4	102	8.9	13
2104.60	250	2.7	0.06	46.8	18.1	34.1	20.2	82	0.32	17.2	59.9	130	25	161.5	18.2	2	60	2.3	97	10.3	14
2104.50	230	2.85	0.14	84.2	14.8	40.2	33.2	73	0.47	16.3	56.5	110	31.3	157.5	17.6	2	67	2.7	125	12.3	16
2104.41	250	2.75	0.05	41.1	18.4	33.3	18	92	0.29	17.5	64.6	100	27.9	160.5	17.9	2	60.5	2.3	95	9.8	17
2104.36	230	2.58	0.08	66.9	15.9	36.6	25.1	120	0.28	16.8	60.8	100	29.8	149	17.5	2	62	2.3	93	10.2	19
2104.29	<10	<0.05	0.21	8.86	0.8	2.2	4.8	187	0.14	0.2	<0.2	280	3.6	2.2	0.4	2	325	2.4	4	10.5	4
2103.99	<10	<0.05	0.29	4.97	0.7	2.2	3.3	163	0.1	0.1	<0.2	150	3	0.7	0.2	2	356	2.5	2	7.2	3
2103.20	<10	<0.05	0.13	2.74	0.7	1.9	2.3	173	0.12	0.1	<0.2	130	2.4	0.6	0.2	2	289	2.2	1	4.9	<2
2102.13	<10	<0.05	0.1	1.33	0.7	2	1.5	372	0.1	0.1	<0.2	30	1.6	0.4	0.2	2	216	2.3	1	2.8	<2
2100.61	<10	<0.05	0.03	1.07	0.5	2.6	1.4	514	0.11	0.1	<0.2	80	1.9	0.2	0.1	2	137.5	3	<1	2.7	<2
2098.55	<10	<0.05	<0.02	0.85	0.6	1.6	1.2	634	0.05	0.1	<0.2	70	0.7	0.2	0.1	2	69.9	1.1	1	2.8	2
2095.53	<10	<0.05	<0.02	0.65	0.4	2	1.2	672	0.08	0.1	<0.2	60	1.7	<0.1	0.1	2	46.7	1.4	<1	2.5	3
2092.57	<10	<0.05	0.16	1.75	0.7	2	2.5	181	0.06	0.1	<0.2	70	<0.5	0.4	0.3	3	303	0.8	1	4.9	2
2091.54	10	<0.05	0.14	1.86	0.5	1.8	3.1	147	0.07	0.1	<0.2	40	1.3	0.1	0.2	3	301	0.8	<1	5.9	<2
2089.88	<10	<0.05	0.25	1.8	0.5	2.7	3	119	0.06	0.1	<0.2	30	2	<0.1	0.2	2	333	0.5	<1	5.3	7
2089.04	<10	<0.05	0.28	1.78	0.6	2.1	2.5	156	0.23	0.1	0.2	70	<0.5	0.3	0.2	3	357	0.7	8	5.4	<2
2087.42	10	<0.05	0.28	1.73	0.5	3	3.5	130	0.09	0.1	<0.2	70	1	0.4	0.2	2	356	0.5	<1	6.6	4
2086.39	10	<0.05	0.27	1.7	0.8	1.8	3.4	154	0.05	0.1	<0.2	60	<0.5	0.3	0.4	2	418	0.5	1	7.4	4
2084.77	10	<0.05	0.24	1.88	0.6	1.8	3.2	127	0.07	0.1	<0.2	50	0.8	0.2	0.4	2	352	0.7	<1	6	2
2083.98	<10	<0.05	0.34	1.51	1.8	2.3	2.5	136	0.05	0.3	<0.2	40	1.2	0.2	0.4	3	346	0.3	1	5.2	9
2082.91	<10	<0.05	0.39	2.08	0.5	1.3	3.2	131	<0.05	0.1	<0.2	50	0.5	0.2	0.3	2	303	0.5	<1	6.5	2
2082.30	<10	<0.05	0.28	1.25	0.6	2	2.4	144	<0.05	0.1	<0.2	30	2.6	<0.1	0.2	2	360	0.5	<1	5.5	2
2081.28	10	<0.05	0.17	1.35	1.7	2	1.7	224	0.06	0.3	<0.2	50	1.1	0.3	0.4	3	507	1.7	2	4.4	3
2080.67	<10	<0.05	0.04	1.41	0.5	1	1.9	146	<0.05	0.1	<0.2	30	<0.5	<0.1	0.1	2	319	1.6	<1	3.5	<2
2080.46	10	<0.05	0.09	1.64	0.4	2.4	1.7	181	0.55	0.1	0.4	120	0.6	0.8	0.3	2	533	2.1	9	3.5	<2
2080.35	10	<0.05	0.14	1.94	0.7	1.3	2.5	162	<0.05	0.2	0.3	40	0.7	0.8	0.4	2	527	2	<1	4.7	<2
2080.21	10	<0.05	0.14	2.14	1.9	2.5	2.1	133	0.05	0.4	<0.2	40	1.7	1.3	0.5	3	543	2.3	2	4.1	2
2079.82	<10	<0.05	0.12	1.31	0.8	1.7	1.8	142	<0.05	0.1	<0.2	40	3.4	<0.1	0.2	2	505	1.9	<1	3.6	<2
2079.59	10	<0.05	0.14	1.32	0.6	1.8	1.5	190	0.08	0.2	<0.2	40	4.6	0.6	0.1	1	456	1.6	1	3.1	2
2079.41	10	<0.05	0.15	1.31	0.7	1.7	1.9	218	0.12	0.1	<0.2	30	3.3	0.2	0.2	2	355	2.1	<1	3.6	<2
2079.16	10	<0.05	0.13	1.36	0.6	2.1	1.6	150	0.05	0.2	<0.2	40	2.8	0.6	0.1	1	387	2.6	<1	3.1	<2

Chapter 3

Glacial-stage eolian delivery of highly reactive iron to late Paleozoic oceans

ABSTRACT

Supply of bioavailable iron to the glacial ocean via eolian dust is well documented for the late Cenozoic. Although recent studies emphasize abundant eolian dust deposits (loess) in the late Paleozoic of western equatorial Pangaea, delivery of highly reactive iron ($Fe_{HR)}$ via eolian dust to the late Paleozoic ocean is unexplored. Here, we report on the Fe_{HR} content of a loess- derived mudrock that accumulated at lowstand (glacial) time within a carbonate buildup of the so- called "Horseshoe Atoll" of the Midland basin (west Texas). High Fe_{HR}/Fe_T ratios compared to modern sediments, average crustal ratios of Fe_T/Al, sedimentological attributes and paleogeography suggest that the enrichment is primarily related to weathering at the source. The Fe_{HR} – enriched sediment was then deflated and transported as eolian dust into the study area, which likely influenced the marine primary productivity in the late Paleozoic Midland sea.

INTRODUCTION

Modern experiments conducted in high-nutrient low chlorophyll (HNLC) patches of ocean show that, in seawater of normal pH, iron is very insoluble and thus a limiting nutrient for marine primary productivity, which in turn affects the climate system by CO_2

uptake ("the iron hypothesis"; Martin and Fitzwater, 1989; Martin et al., 1990, 1991, 1994; Kumar et al., 1995; Coale et al., 1996; Boyd et al., 2000; Turner et al., 2004). Atmospheric dust provides an important source of bioavailable (biogeochemically reactive) iron to the open ocean (e.g. Fung, et al., 2000; Jickells et al., 2005; Fan et al., 2006). This, coupled with the recognition of increased atmospheric dust flux during glacial stages of the late Cenozoic, have caused many to link glacial climates with higher iron supply to the ocean and thus enhanced marine primary productivity (e.g. Kumar et al., 1995; Rutberg et al., 2005; Moore et al., 2006; Winckler et al., 2008). Highlighting similarities between the late Cenozoic and late Paleozoic glaciations in terms of their repeated glacial- interglacial variations, high atmospheric dust loads, monsoonal circulation and importance of algal- based bioherms, Soreghan and Soreghan (2002) hypothesized a possible link between atmospheric dust and primary productivity during the late Paleozoic, but no further effort has been made to test this hypothesis for the late Paleozoic, as detecting productivity in the ancient record is not straightforward.

Analytical techniques by Canfield (1989), Raiswell et al (1994), Raiswell and Canfield (1998), Poulton and Canfield (2005) identified three "reactive" iron pools within the total iron (Fe_T) pool. These are highly reactive iron (Fe_{HR}), poorly reactive iron and unreactive iron. Fe_{HR} consists of amorphous and crystalline iron oxides and (oxyhydr)oxides that are readily reactive to H_2S on an early diagenetic time scale. Fe_{HR} in ancient sediments is dominated by crystalline forms soluble in citrate- bicarbonate-dithionite solution and iron transformed to pyrite (Fe_{py}). Studies of modern glacial sediments show the presence of bioavailable, poorly crystalline iron (oxyhydr)oxides nanoparticles, the abundance of which is roughly consistent with Fe_{HR} content (Raiswell

et al., 2006). Accordingly, Fe_{HR} roughly tracks bioavailability and thus can be used as a potential proxy for primary productivity.

Here we characterize a late Paleozoic (middle Virgilian) aged, dust- derived mudrock from a glacio- eustatic sequence of the so- called "Horseshoe Atoll" of the Midland basin (west Texas), and evaluate the Fe_{HR} pool. Our results indicate remarkably high ratios of Fe_{HR}/Fe_T relative to modern sediments, which likely influenced primary productivity in the late Paleozoic Midland sea.

GEOLOGICAL BACKGROUND

The Midland basin was an epicontinental basin that formed during collision between Gondwana and Laurasia during early Pennsylvanian time. The basin remained equatorial (≤10° N) throughout the late Paleozoic (e.g. Walker et al., 1995; Scotese, 2001). The "Horseshoe Atoll" formed an arcuate, isolated carbonate buildup in the middle of the Midland basin (Fig. 3.1A) that consists of a series of middle Pennsylvanian to early Permian- aged phylloid- algal buildups devoid of any siliciclastic material excepting that delivered via eolian input (Sur et al., in review b). The upper Pennsylvanian section contains several glacioeustatic sequences (~ 18 to 24 m thick), separated by subaerial exposure surfaces (sequence boundaries) that record glacial (lowstand) conditions (Sur et al., in review b). The middle Virgilian study interval consists predominantly (99%) of carbonate (limestone and dolostone), with <1% siliciclastic mudrock concentrated at sequence boundaries (Fig. 3.1B).

We focused on the sequence- bounding mudrock from two successive sequences. The entire section is subsurface, hence our studies are based on material from a

continuous air- drilled core. Detailed sedimentology of the entire sequence is presented in Sur et al (in review b).

SEDIMENTOLOGICAL AND GEOCHEMICAL ATTRIBUTES OF THE MUDROCK

The mudrock (non-fissile clastic mudstone) composes ~ 0.37 m of the studied (24.3 m) sequence and occurs above the subaerial exposure surface, which is marked by pedogenic calcrete and root traces (e.g. Saller et al., 2004). This mudrock is in sharp contact with the carbonate facies (foram/algal grainstone) below and above and exhibits a dark gray to greenish color (N4 to 5G 4/1) and local randomly oriented slickensides (Fig. 3.2A). Local pedogenic fabrics occur, including subangular blocky microstructures with planar- and channel- type voids (Bullock et al., 1985), pedotubules (root traces and burrows), argillans and ferrans. Some samples exhibit a sepic plasmic fabric (Brewer, 1976) (Fig. 3.2B) and small, rare carbonate nodules, with local circumgranular cracks (Fig. 3.2C). Euhedral pyrite crystals and aggregates of pyrite occur commonly. Scattered bladed and coarse crystals of marcasite and radiating crystals of marcasite surrounding pyrite spheres occur locally (Fig. 3.2D). Carbonate is rare in horizons that contain marcasite.

Isolation of the silicate mineral fraction (SMF) of the mudrock by sequential removal of carbonate, organic matter, pyrite and Fe- oxides (Sur et al., in review a, b), reveals that quartz and clay (illite) are the dominant components, followed by muscovite, potassium feldspar, plagioclase feldspar (albite), zircon and biotite, in decreasing abundance. Most of the quartz is subrounded to subangular in shape, with some surficial

pitting on larger (very fine sand) grains, and are inferred to be of detrital origin. Grain size analyses of the total SMF reveals mean, median, and modal sizes of ~ 6 μm, ~ 5.5 μm and ~ 5 μm respectively.

Several (5) mudrock samples were analyzed for bulk rock geochemistry (ICP-MS), total organic carbon (TOC), total sulfur (S_T), dithionite- soluble iron concentration (Fe_D), pyrite sulfur concentration (S_{py}) and pyrite sulfur isotope composition ($\delta^{34}S_{py}$). Fe_{HR} is measured by summing the Fe_D and Fe_{py} (e.g. Poulton and Canfield, 2005). This method yields ratios of Fe_{HR} to total iron (Fe_T) ranging from 0.657 to 0.78 (Table 3.1). These values are much higher than reported values from modern riverine particules (average 0.43 ± 0.03; Poulton and Raiswell, 2002), oxically and suboxically deposited continental margin and deep sea sediments (0.26 ± 0.09; Anderson and Raiswell, 2004), glacial sediments (0.11 ± 0.11; Poulton and Raiswell, 2002) and Saharan dust particulates (0.33 ± 0.01; Poulton and Raiswell, 2002). Rather, they approximate modern euxinic (anoxic and sulfidic) marine sediments, e.g. from the Black Sea, Cariaco Basin, Orca Basin and Effingham Inlet (Lyons and Severmann, 2006). The Fe_T/Al of the studied section ranges from 0.318 to 0.414 (average 0.364), which approaches the average Fe_T/Al (0.42) of the upper continental crust (UCC) (Taylor and McLennan, 1985) and is much lower than values (mean 0.89 ± 0.16) from modern euxinic marine sediments (Lyons and Severmann, 2006). The mudrock contains very low TOC (0.125 to 0.25 %) and relatively high total sulfur (2.01 to 3.01 %). $\delta^{34}S_{py}$ shows heavy values ranging from 1.20 to 10.80 $^{o}/_{oo}$.

DISCUSSION

Origin and Diagenesis of the Mudrock

Paleogeographic and sedimentologic considerations led Sur et al (in review b) to infer that the mudrock originated as a loess deposit. Summary evidence for this inference includes: 1) paleogeographic isolation of the study area from fluvio- deltaic input; 2) lack of evidence for sufficient limestone dissolution to form ~ 0.37 m of insoluble residue; 3) presence of subrounded to subangular detrital quartz grains and a mean particle size of fine silt (~ 6 μm), which is readily transportable by wind. Moreover, recent recognition of abundant eolian dust deposits (loess) in western equatorial Pangaea during late Paleozoic time (e.g. Soreghan et al., 2008a) and recognition of dust as a potential source for Phanerozoic bedded chert (Cecil, 2004), lend further support for this hypothesis.

The presence of pedogenic features suggest that loess (eolian dust) accumulation occured primarily during subaerial exposure and was concurrently and/or subsequently subjected to pedogenesis. Clays in this paleosol are not the product of *in situ* weathering or clay illuviation. Instead they are detrital (eolian) in origin as evidenced by changes in Ti/Zr (immobile element) ratios throughout the profile (Sur et al., in review b). Vertic features e.g. slickensides and sepic- plasmic microfabric, suggest seasonality. Overall the paleosol is interpreted as an immature paleosol with vertic features based on the very weak development of pedogenic structure and lack of distinctive horizonation.

Presence of differential compaction around some pyrite grains suggests an early diagenetic origin for the pyrite. Sulfate for pyrite formation was likely supplied by seawater seepage as in many ancient transgressed paleosols (e.g. Wright, 1986; Wright et al., 1997; Driese and Ober, 2005). This is further supported by the heavy $\delta^{34}S_{py}$. As the mudrock contains very low TOC, a reasonable electron donor for the sulfate reduction

could be methane which could reflect production of isotopically heavy H_2S (Jørgensen et al., 2004). The methane could have diffused from the decomposition of soil organic matter, and the reactive iron supplied from atmospheric dust for the early diagenetic pyrite formation. However presence of some coarsely crystalline pyrite suggests an origin during late burial, which likely overprinted the early diagenetic isotopic signal of seawater. Nonetheless, alterations associated with evaporitic brine solutions during late burial- stage diagenesis (Saller, 1999) is minor in the studied core, as indicated by the bulk carbonate rock Sr isotope average value (of 0.708281) which is very close to the contemporaneous seawater value (T. Rasbury, unpublished data 2007).

Taken together, these observations indicate the mudrock records an origin as a loess deposit that was slightly pedogenically altered. Its juxtaposition between the exposure surface (sequence boundary) and superjacent marine limestone (foram/algal grainstone) suggests its deposition during glacial lowstand (exposure), marked by attendant high atmospheric dust loads and aridity, and subsequent marine transgression and diagenesis (Sur et al., in review b).

Enrichment of Highly Reactive Iron/Total Iron (Fe_{HR}/Fe_T)

The high values of Fe_{HR}/Fe_T in the studied mudrock could originate from various mechanisms as follows:

a) Enrichment due to deep euxinic conditions (e.g. Black Sea, Cariaco Basin, Orca Basin, Effingham Inlet)?

In this environment, the enrichment of Fe_{HR}/Fe_T occurs due to scavenging of reactive iron from the water column during syngenetic pyrite formation. This mechanism

also enriches the Fe_T/Al ratio by decreasing the detrital Al content in the deep basin (Lyons and Severmann, 2006). However, in our example the Fe_T/Al ratio is much lower than in modern euxinic basins and close to the composition for UCC, which does not support an influence of local enrichment of Fe_T/Al. Furthermore, the very low TOC also contradicts the modern euxinic model, wherein high TOC is expected owing to anoxic conditions.

b) Enrichment due to in situ weathering of the loess?

Although evidence for some pedogenic activity occurs in the studied mudrock the weak development of the pedogenic structures and lack of horizonation indicates only minimal *in situ* weathering. Furthermore, high Fe_{HR}/Fe_T also characterizes the silicate material hosted in the carbonate from the other sequence boundary lacking associated mudrock and pedogenesis. Hence, *in situ* weathering can not provide a major source of Fe_{HR}/Fe_T in the studied rock and Sur et al (in review b) interpreted the sediments for the loess deposition as having been sourced from pre- weathered material.

c) Enrichment due to weathering at the source?

Glacial- and iceberg- hosted sediments contain poorly crystalline nanoparticulate iron (oxyhydr)oxides, derived from weathering of the reactive- iron bearing phases at the source or during transport, and are potentially bioavailable (Raiswell et al., 2006, 2008a, b). Therefore, processes of weathering at the source can increase highly reactive iron in the sediments. During glacial phases, physical weathering predominates; Raiswell et al. (2006), for example, have shown that the ratio of physical to chemical erosion in glaciated terrain is ~10 times higher than in non- glaciated terrain. Such weathering

produces copious amounts of fresh rock and mineral surfaces which are prone to chemical weathering to produce nanoparticulate iron (oxyhydr)oxides.

Glaciation during the late Paleozoic is well established and the glaciation has long been thought confined to the southern polar (Gondwana) region (Crowell, 1999). More recently, however, glacial and periglacial conditions have been hypothesized in relatively low- elevation regions of the Ancestral Rocky Mountains (ARM) in western equatorial Pangea (Soreghan et al 2008a, b; Sweet and Soreghan, 2008). This hypothesis, if valid, raises the possibility that the late Paleozoic glaciation was more extreme than that of the late Cenozoic and thus could have resulted in more voluminous production of nanoparticulate iron (oxyhydr)oxides. The Fe_{HR}/Fe_T ratio in modern glacial sediments (Raiswell et al., 2006) varies from 0.09 to 0.70 with an average of 0.29. Although the average is much lower than our average value, their highest value approaches our average value. Therefore, we hypothesize that the enrichment of Fe_{HR}/Fe_T in the studied mudrock may reflect their derivation from glaciated regions of the ARM and/or other highlands upwind of the study area.

Transport distance can also contribute to Fe_{HR}/Fe_T enrichment, because fine particles or clay increase in abundance with atmospheric transport distance and result in increased amounts of soluble iron (e.g. Journet and Desboeufs, 2007). Hence, we suggest that our data can be best explained by the action of primary source- related weathering together with eolian transport of the weathered material into the study area.

IMPLICATIONS

The importance of iron is its solubility and thus its bioavailability. Raiswell et al. (2006, 2008a, b) noted that iron bioavailability from modern glacial sediments decreases with increasing crystallinity and age, which is more pronounced with riverine transport. However, eolian transport of nanoparticulate iron (oxyhydr)oxide directly from the primary source to the study area during glacial phases should involve considerably shorter duration, enabling preservation of the amorphous nature and thus the bioavailability. Solubility of iron and thus bioavailability are further increased during transport by photoreduction, cloud processing, organic complexation (e.g. Jickells et al., 2005) and increased clay content (e.g. Journet and Desboeufs, 2007).

From these data, together with growing recognition of remarkably high atmospheric dust loads and hypothesized episodes of tropical cold climate during the late Paleozoic (Soreghan et al., 2008a) we propose that large amounts of Fe_{HR} were supplied to glacial late Paleozoic oceans of western equatorial Pangaea. If so, then this Fe- rich dust could have greatly stimulated primary productivity during glacials, and thus influenced carbon cycling (Fig. 3.3). This hypothesis merits further exploration and testing.

ACKNOWLEDGEMENTS

This work is an outgrowth of S. Sur's PhD dissertation funded in part by grants from the American Chemical Society of the Petroleum Research Fund (PRF # 39198-AC8), the National Science Foundation (EAR- 0746042), the American Association of Petroleum Geologists, the Geological Society of America, the Society for Sedimentary Geology (SEPM) Rocky Mountain Section (Donald L. Smith grant), Chevron (USA) and

the ConocoPhillips School of Geology and Geophysics at the University of Oklahoma, Norman. We thank A. Saller, G. Hinterlong, A. Auffant, S. Randall for help in core access and sampling. We are grateful to A. Saller, R. Raiswell and J. Schieber for helpful discussions. Many thank to C. Scott, S. Bates and J. Owens of the University of California, Riverside for their assistance in laboratory work.

LIST OF FIGURES

REFERENCES CITED

Anderson, T.F., and Raiswell, R., 2004, Sources and mechanisms for the enrichment of highly reactive iron in euxinic Black Sea sediments: American Journal of Science, v. 304, p. 203-233.

Boyd, P.W., and 34 coauthors, 2000, A mesoscale phytoplankton bloom in the polar Southern Ocean stimulated by iron fertilization: Nature, v. 407, p. 695-702.

Brewer, R., 1976, Proposal for a micromorphological classification of soil materials; I, A classification of the related distributions of fine and coarse particles-Discussion: Geoderma, v. 15, p. 437-442.

Bullock, P., Fedoroff, N., Jongerius, A., Stoops, G., and Tursina, T., 1985, Handbook for soil thin section description: Waine Research Publications, 151 p.

Canfield, D.E., 1989, Reactive iron in marine sediments: Geochimica et Cosmochimica Acta, v. 53, p. 619-632.

Cecil, C.B., 2004, Eolian dust and the origin of sedimentary chert: U.S. Geological Survey Open-File Report 2004-1098, 15 p.

Coale, K.H., and 18 coauthors, 1996, A massive phytoplankton bloom induced by an ecosystem-scale iron fertilization experiments in the equatorial Pacific Ocean: Nature, v. 383, p. 495-501.

Crowell, J.C., 1999, Pre-Mesozoic ice ages: Their bearing on understanding the climate system: Geological Society of America Memoir 192, 122 p.

Driese, S.G., and Ober, E.G., 2005, Paleopedologic and paleohydrologic records of precipitation seasonality from early Pennsylvanian "underclay" Paleosols, USA: Journal of Sedimentary Research, v. 75, p. 997-1010.

Fan, S.M., Moxim, W.J., and Levy, H. II., 2006, Aeolian input of bioavailable iron to the ocean: Geophysical Research Letters, v. 33, L07602.

Fung, I.Y., Meyn, S.K., Tegen, I., Doney, S.C., John, J.G., and Bishop, J.K.B., 2000, Iron supply and demand in the upper ocean: Global Biogeochemical Cycles, v. 14, p. 281-295.

Jickells, T.D., An, Z.S., Andersen, K.K., Baker, A.R., Bergametti, G., Brooks, N., Cao, J.J., Boyd, P.W., Duce, R.A., Hunter, K.A., Kawahata, H., Kubilay, N., laRoche, J., Liss, P.S., Mahowald, N., Prospero, J.M., Ridgwell, A.J., Tegen, I., and Torres, R., 2005, Global iron connections between desert dust, ocean biogeochemistry, and climate: Science, v. 308, p. 67-71.

Jorgensen, B.B., Bottcher, M.E., Luschen, H., Neretin, L.N., and Volkov, II., 2004, Anaerobic methane oxidation and a deep H_2S sink generate isotopically heavy sulfides in Black Sea sediments: Geochimica et Cosmochimica Acta, v. 68, p. 2095-2118.

Journet, E., and Desboeufs, K., 2007, Mineralogy as a critical factor of dust iron solubility and bioavailability: Geophysical Research Abstracts, European Geosciences Union 2007, v. 9, 00934.

Kumar, N., Anderson, R.F., Mortlock, R.A., Froelich, P.N., Kubik,P., Dittrich-Hannen, B., and Suter, M., 1995, Increased biological productivity and export production in the glacial Southern Ocean: Nature, v. 378, p. 675-680.

Lyons, T.W., and Severmann, S., 2006, A critical look at iron paleoredox proxies; new insights from modern euxinic marine basins: Geochimica et Cosmochimica Acta, v. 70, p. 5698-5722.

Martin, J.H., and Fitzwater, S.E., 1989, Iron deficiency limits phytoplankton growth in the north-east Pacific subarctic: Nature, v. 331, p. 341-343.

Martin, J.H., Fitzwater, S.E., and Gordon, R.M., 1990, Iron deficiency limits phytoplankton growth in Antarctic waters: Global Biogeochemical Cycles, v. 4, p. 5-12.

Martin, J.H., Gordon, R.M., and Fitzwater, S.E., 1991, The case for iron: Limnology and Oceanography, v. 36, p. 1793-1802.

Martin, J.H., and 43 coauthors, 1994, Testing the iron hypothesis in ecosystems of the equatorial Pacific Ocean: Nature, v. 371, p. 123-129.

Moore, C.M., Mills, M.M., Milne, A., Langlois, R., Achterberg, E.P., Lochte, K., Geider, R.J., and LaRoche, J., 2006, Iron limits primary productivity during spring bloom development in the central North Atlantic: Global Change Biology, v. 12, p. 626-634.

Poulton, S.W., and Raiswell, R., 2002, The low-temperature geochemical cycle of iron; from continental fluxes to marine sediment deposition: American Journal of Science, v. 302, p. 774-805.

Poulton, S.W., and Canfield, D.E., 2005, Development of a sequential extraction procedure for iron; implications for iron partitioning in continentally derived particulates: Chemical Geology, v. 214, p. 209-221.

Raiswell, R., Canfield, D.E., and Berner, R.A., 1994, A comparison of iron extraction methods for the determination of degree of pyritisation and the recognition of iron-limited pyrite formation: Chemical Geology, v. 111, p. 101-110.

Raiswell, R., and Canfield, D.E., 1998, Sources of iron for pyrite formation in marine sediments: American Journal of Science, v. 298, p. 219-245.

Raiswell, R., Tranter, M., Benning, L.G., Siegert, M., De'ath, R., Huybrechts, P., and Payne, T., 2006, Contributions from glacially derived sediment to the global iron (oxyhydr)oxide cycle; implications for iron delivery to the oceans: Geochimica et Cosmochimica Acta, v. 70, p. 2765-2780.

Raiswell, R., Benning, L.G., Tranter, M., and Tulaczyk, S., 2008a, Bioavailable iron in the Southern Ocean: the significance of the iceberg conveyor belt: Geochemical Transaction, v. 9:7, p. 1-9.

Raiswell, R., Benning, L.G., Davidson, L., and Tranter, M., 2008b, Nanoparticulate bioavailable iron minerals in icebergs and glaciers: Mineralogical Magazine, v. 72, p. 345-348.

Rutberg, R.L., Goldstein, S.L., Hemming, S.R., and Anderson, R.F., 2005, Sr isotope evidence for sources of terrigenous sediment in the southeast Atlantic Ocean: Is there increased available Fe for enhanced glacial productivity? Paleoceanography, v. 20, p. PA1018.

Saller, A.H. 1999, Core description and sedimentology of Upper Pennsylvanian and lowest Permian limestones and dolomite, South Dome of Reinecke Field, west Texas: Unpublished internal report, Unocal Corporation.

Saller, A.H., Walden, S., Robertson, S., Steckel, M., Schwab, J., Hagiwara, H., and Mizohata, S., 1999, Reservoir characterization of a reefal carbonate for crestal CO_2 flood, Reinecke Field, west Texas, in Hentz, T.F., ed, Advanced Reservoir Characterization for the 21st Century: Gulf Coast Section SEPM Foundation 19th Annual Research Conference, p. 259-268.

Saller, A.H., Walden, S., Robertson, S., Steckel, M., Schwab, J., Hagiwara, H., and Mizohata, S., 2004, Three-dimensional seismic imaging and reservoir modeling of an upper Paleozoic "reefal" buildup, Reinecke Field, west Texas, United States, *in* Seismic imaging of carbonate reservoirs and systems: American Association of Petroleum Geologists Memoir, 81, p. 107-122.

Scotese, C.R., 2001, Atlas of Earth History, Volume 1 (Paleogeography): PALEOMAP Project, Arlington, Texas.

Soreghan, G.S., and Soreghan, M.J., 2002, Atmospheric dust and algal dominance in the late Paleozoic: A hypothesis: Journal of Sedimentary Research, v. 72, p. 457-461.

Soreghan, G.S., Soreghan, M.J., and Hamilton, M.A., 2008a, Origin and significance of loess in late Paleozoic western Pangaea: A record of tropical cold?: Palaeogeography, Palaeoclimatology, Palaeoecology, v. 268, p. 234-259.

Soreghan, G.S., Soreghan, M.J., Poulsen, C.J., Young, R.A., Eble, C.F., Sweet, D.E., and Davogustto, O.C., 2008b, Anomalous cold in the Pangaean tropics: Geology, v. 36, p. 659-662.

Sur, S., Soreghan, G.S., Soreghan, M.J., and Stagner, A.F., in review a, Extraction methodology for the silicate mineral fraction (eolian dust) from ancient carbonate: assessing the geologic record of dust: submitted in Journal of Sedimentary Research.

Sur, S., Soreghan, G.S., Soreghan, M.J., and Yang, W., in review b, A high-resolution record of atmospheric dust from the Pennsylvanian tropics: submitted in Journal of Sedimentary Research.

Sweet, D.E., and Soreghan, G.S., 2008, Polygonal cracking in coarse clastics records cold temperatures in the equatorial Fountain Formation (Pennsylvanian-Permian, Colorado): Palaeogeography, Palaeoclimatology, Palaeoecology, v. 268, p. 193-204.

Taylor, S.R., and McLennan, S.M., 1985, The continental crust: Its composition and evolution, Blackwell, Oxford.

Turner, D.R., Bertilsson, S., Fransson, A., and Pakhomov, E.A, 2004, The SWEDARP 1997/98 marine expedition; overview, *in* Turner, D.R., Anderon, L., McQuaid, C., Nost, O.A., and Pakhomov, E.A., eds., The SWEDARP 1997/98 expedition: Deep-Sea Research. Part II: Topical Studies in Oceanography, v. 51, p. 2543-2556.

Walker, D.A., Golonka, J., Reid, A., and Reid, S., 1995, The effects of paleolatitude and paleogeography on carbonate sedimentation in the late Paleozoic: American Association of Petroleum Geologists, Studies in Geology, v.40, p. 133-155.

Winckler, G., Anderson, R.F., Fleisher, M.Q., McGee, D., and Mahowald, N., 2008, Covariant glacial-interglacial dust fluxes in the equatorial Pacific and Antarctica: Science, v. 320, p. 93-96.

Wright, V.P., 1986, Pyrite formation and the drowning of a paleosol: Geological Journal, v. 21, p. 139-149.

Wright, V.P., Vanstone, S.D., and Marshall, J.D., 1997, Contrasting flooding histories of Mississippian carbonate platforms revealed by marine alteration effects in palaeosols: Sedimentology, v. 44, p. 825-842.

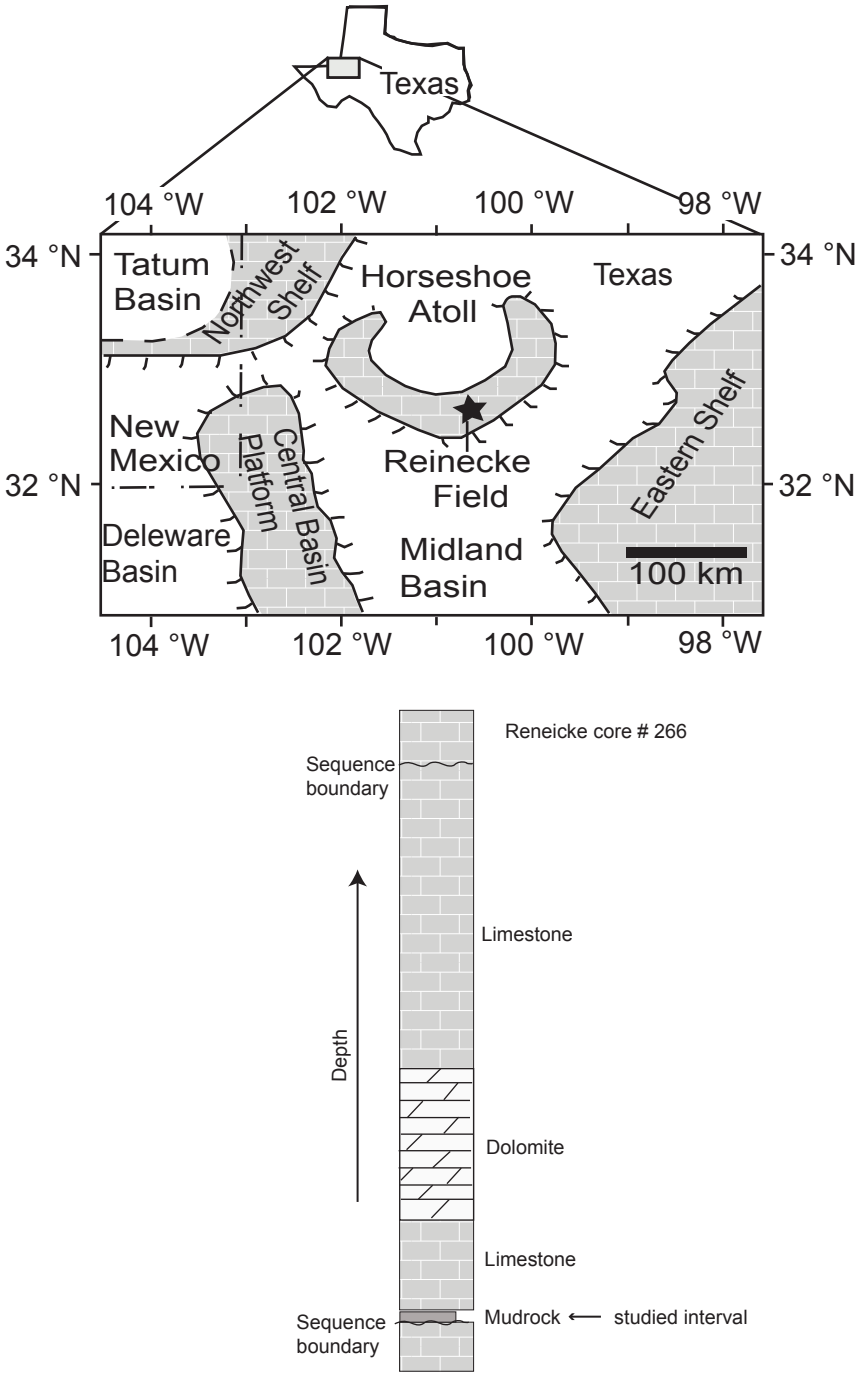
Texas
104 °W
102 °W
100 °W
98 °W
34 °N
32 °N
Tatum Basin
Northwest Shelf
Horseshoe Atoll
Texas
New Mexico
Central Basin Platform
Reinecke Field
Eastern Shelf
Deleware Basin
Midland Basin
100 km
Reneicke core # 266
Sequence boundary
Limestone
Depth
Dolomite
Limestone
Mudrock ⟵ studied interval
Sequence boundary

Figure 3.1

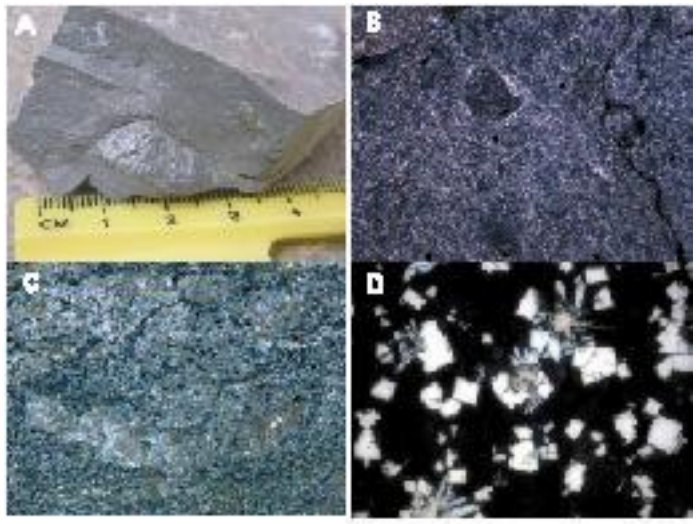

Figure 3.2

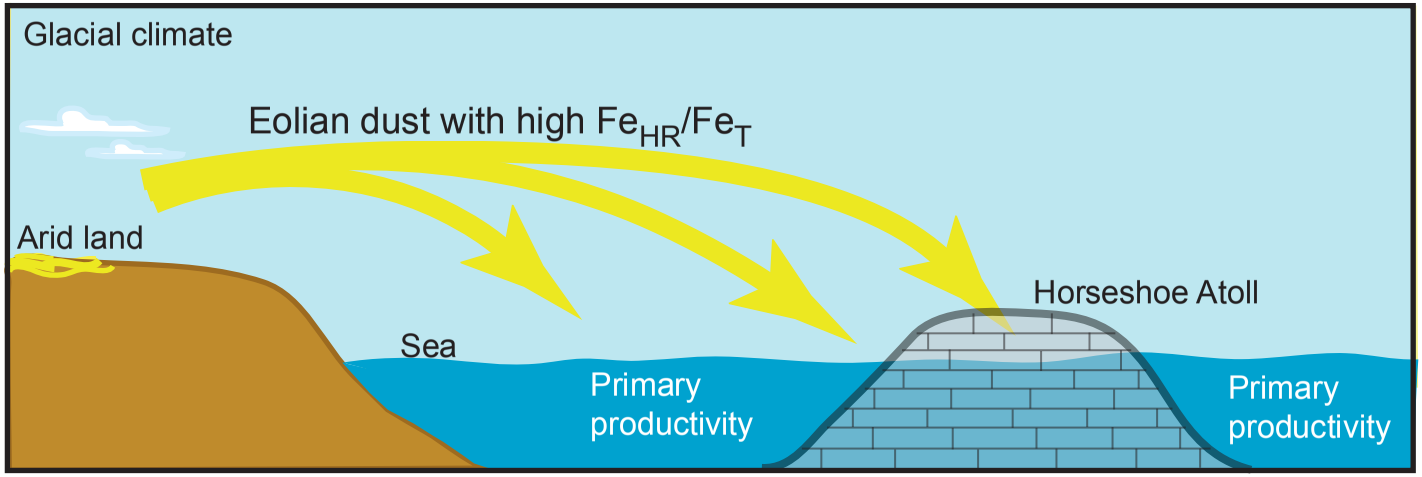
Glacial climate
Eolian dust with high Fe_{HR}/Fe_T
Arid land
Horseshoe Atoll
Sea
Primary productivity
Primary productivity

Figure 3.3

TABLE 3.1: SUMMARY OF GEOCHEMICAL DATA

Sample Number	TOC (%)	S_{py} (%)	Fe_{py} (%)	Fe_D (%)	Fe_{HR} (%)	Fe_{HR}/Fe_T	Fe_T/Al	$\delta^{34}S_{py}$ ($^o/_{oo}$)
S- 2	0.205	1.914	1.67	0.12	1.78499	0.699996	0.3316	9.6
S- 4	0.15	1.933	1.68	0.13	1.81039	0.707184	0.31841	10.8
S- 8	0.25	2.824	2.46	0.13	2.58467	0.780868	0.41479	1.2
S- 12	0.18	2.019	1.76	0.14	1.89409	0.65767	0.36	6.7
S-16	0.125	2.495	2.17	0.01	2.18559	0.682997	0.39801	5.3

* Mudrock samples are in their relative depth position. Depth increses from S-2 to S- 16.